First Search for Heavy Neutral Leptons with IceCube DeepCore

Dissertation
zur Erlangung des akademischen Grades
doctor rerum naturalium
(Dr. rer. nat.)

im Fach: Physik
Spezialisierung: Experimentalphysik

eingereicht an der
Mathematisch-Naturwissenschaftlichen Fakultät
der Humboldt-Universität zu Berlin

von
Leander Fischer M. Sc.
geboren am 24. Oktober 1992
in Heidelberg

Präsidentin der Humboldt-Universität zu Berlin
Prof. Dr. Julia von Blumenthal

Dekanin der Mathematisch-Naturwissenschaftlichen Fakultät
Prof. Dr. Caren Tischendorf

Colophon
This document was typeset with the help of KOMA-Script and LaTeX using the open-source kaobook template class.

The source code of this thesis is available at:
https://github.com/LeanderFischer/phd_thesis

Todo list

Contents

Standard Model Neutrinos and Beyond

1

1.1 The Standard Model

The *standard model (SM)* of particle physics is a Yang-Mills theory [1] providing very accurate predictions of weak, strong, and *electromagnetic (EM)* interactions. It is a relativistic quantum field theory that relies on gauge invariance, where all matter is made up of fermions, which are divided into quarks and leptons, and bosons describe the interactions between the fermions that have to fulfil the overall symmetry of the theory. Leptons are excitations of Dirac-type fermion fields.

[1]: Yang et al. (1954), "Conservation of Isotopic Spin and Isotopic Gauge Invariance"

The initial idea of the theory is associated with the works of Weinberg [2], Glashow [3], and Salam [4], that proposed a unified description of EM and weak interactions as a theory of a spontaneously broken SU(2) x U(1) symmetry for leptons, predicting a neutral massive vector boson Z^0, a massive charged vector boson $W^{\pm}$, and a massless photon γ as the gauge bosons. The Higgs mechanism [5], describing the breaking of the symmetry, predicts the existence of an additional scalar particle, the Higgs boson, giving the $W^{\pm}$ and Z^0 bosons their mass. The Higgs boson was discovered in 2012 at the LHC [6, 7].

[2]: Weinberg (1967), "A Model of Leptons"

[3]: Glashow (1961), "Partial-symmetries of weak interactions"

[5]: Higgs (1964), "Broken symmetries, massless particles and gauge fields"

[6]: Chatrchyan et al. (2012), "Observation of a New Boson at a Mass of 125 GeV with the CMS Experiment at the LHC"

[7]: Aad et al. (2012), "Observation of a new particle in the search for the Standard Model Higgs boson with the ATLAS detector at the LHC"

Gell-Mann and Zweig proposed the quark model in 1964 [8, 9], which was completed by the discovery of non-abelian gauge theories [10] to form the SU(3) symmetry of the strong interaction called *quantum chromodynamics (QCD)*. QCD describes the interaction between quarks and gluons which completed the full picture of the SM in the mid-1970s. Together with the electroweak theory, the SM is a $SU(3)_C$ x $SU(2)_L$ x $U(1)_Y$ local gauge symmetry, with the conserved quantities *color* (C), *left-handed chirality* (L), and *weak hypercharge* (Y).

[8]: Gell-Mann (1964), "A Schematic Model of Baryons and Mesons"

[9]: Zweig (1964), "An SU(3) model for strong interaction symmetry and its breaking. Version 2"

In the following, the basic properties of the SM are described, following the derivations of [11, 12].

[11]: Giunti et al. (2007), *Fundamentals of Neutrino Physics and Astrophysics*

[12]: Schwartz (2013), *Quantum Field Theory and the Standard Model*

1.1.1 Fundamental Fields

Fermions in the SM are Weyl fields with either *left-handed (LH)* or *right-handed (RH)* chirality, meaning they are eigenvectors of the chirality operator γ_5 with $\gamma_5 \psi_{R/L} = \pm \psi_{R/L}$. Only LH particles transform under $SU(2)_L$. The Higgs field is a complex scalar field, a doublet of $SU(2)_L$, which is responsible for the spontaneous symmetry breaking of $SU(2)_L$ x $U(1)_Y$ to $U(1)_{EM}$. Local gauge transformations of the fields are given by

$$\psi \rightarrow e^{ig\theta^a(x)T^a}\psi \,, \tag{1.1}$$

where g is the coupling constant, $\theta^a(x)$ are the parameters of the transformation, and T^a are the generators of the group, with a counting them. The number of bosons is dependent on the generators of the symmetry groups, while the strength is defined by the coupling constants. There are eight massless gluons corresponding to the generators of the $SU(3)_C$ group. These

mediate the strong force which conserves color charge. The W_1, W_2, W_3, and B boson fields of the SU(2)$_L$ x U(1)$_Y$ group are mixed into the massive bosons through spontaneous symmetry breaking as

$$W^{\pm} = \frac{1}{\sqrt{2}}(W_1 \mp iW_2) \tag{1.2}$$

and

$$Z^0 = \cos\theta_W W_3 - \sin\theta_W B \ , \tag{1.3}$$

with θ_W being the *Weinberg angle*. The massless photon field is given by

$$A = \sin\theta_W W_3 + \cos\theta_W B \tag{1.4}$$

and its conserved quantity is the EM charge Q, which depends on the weak hypercharge, Y, and the third component of the weak isospin, T_3, as $Q = T_3 + Y/2$.

	Type			Q
quarks	u	c	t	+2/3
	d	s	b	-1/3
leptons	ν_e	ν_μ	ν_τ	0
	e	μ	τ	-1

Table 1.1: Fermions in the Standard Model. Shown are all three generations of quarks and leptons with their electric charge Q.

Fermions are divided into six quarks and six leptons, which are listed in Table 1.1. The quarks interact vie the weak, the strong, and the EM force, and they are always found in bound form as baryons or mesons. Leptons do not participate in the strong interaction and only the electrically charged leptons are massive and are effected by the EM force, while neutrinos only interact via the weak force and are predicted to be massless in this original form of the SM. Each charged lepton has an associated neutrino, which it interacts with in *charged-current (CC)* weak interactions, that will be explained in more detail in Section 1.1.4. For the massive fermion a LH and a RH component exist (e_L, e_R), while the neutrinos only have a LH component (ν_{eL}). Both LH fields of one generation form a doublet under SU(2)$_L$, $L_L = (\nu_{eL}, e_L)^T$, while the RH fields are singlets under SU(2)$_L$, e_R.

1.1.2 Electroweak Symmetry Breaking

To elaborate the process of spontaneous symmetry breaking through which the gauge bosons of the weak interaction acquire their masses, the Lagrangian of the Higgs field is considered as

$$\mathcal{L}_{\text{Higgs}} = (D_\mu \Phi^\dagger)(D^\mu \Phi) - \lambda\left(\Phi^\dagger\Phi - \frac{v^2}{2}\right)^2 \ , \tag{1.5}$$

with parameters λ and v, where λ is assumed to be positive. Φ is the Higgs doublet, which is defined as

$$\Phi = \begin{pmatrix} \Phi^+ \\ \Phi^0 \end{pmatrix} , \tag{1.6}$$

with the charged component Φ^+ and the neutral component Φ^0. The covariant derivative is given by

$$D_\mu = \partial_\mu - ig_2\frac{\sigma^i}{2}W_\mu^i - \frac{1}{2}ig_1 B_\mu \ , \tag{1.7}$$

with the Pauli matrices σ^i and the gauge boson fields W_μ^i and B_μ of the SU(2)$_L$ and U(1)$_Y$ groups, respectively. The coupling constants g_2 and g_1 are the respective coupling constants which are related to the Weinberg angle as $\tan\theta_W = \frac{g_1}{g_2}$. The Higgs potential has a non-zero *vacuum expectation value*

(vev) at the minimum of the potential at $\Phi^\dagger\Phi = \frac{v^2}{2}$. Since the vacuum is electrically neutral, it can only come from a neutral component of the Higgs doublet as

$$\Phi_{\text{vev}} = \frac{1}{\sqrt{2}}\begin{pmatrix}0\\ v\end{pmatrix}. \tag{1.8}$$

1.1.3 Fermion Masses

The mass term for charged fermions with spin-1/2 is given by

$$\mathscr{L}_{\text{Dirac}} = m(\bar{\Psi}_R\Psi_L - \bar{\Psi}_L\Psi_R)\,, \tag{1.9}$$

composed of the product of LH and RH Weyl spinors $\Psi_{L/R}$. This term is not invariant under SU(2)$_L$ x U(1)$_Y$ gauge transformations, but adding a Yukawa term

$$\mathscr{L}_{\text{Yukawa}} = -Y^e\bar{L}_L\Phi e_R + h.c.\,, \tag{1.10}$$

coupling the fermion fields e_R to the Higgs field Φ, recovers the invariance and gives the fermions their masses. Here, Y^e is the Yukawa coupling constant and $\bar{L}_L$ is the SU(2)$_L$ doublet. With the vev, this results in the mass term for the charged leptons and down-type quarks of $-m_e(\bar{e}_L e_R + \bar{e}_R e_L)$ with $m_e = \frac{Y^e v}{\sqrt{2}}$. With $\tilde{\Phi} = i\sigma_2\Phi^*$, a similar Yukawa term can be written as $-Y^u\bar{L}_L\tilde{\Phi}u_R + h.c.$, which leads to the masses of the up-type quark fields u_R.

1.1.4 Leptonic Weak Interactions after Symmetry Breaking

After the spontaneous symmetry breaking, the leptonic part of the electroweak Lagrangian can be written as

$$\mathscr{L}^{\ell}_{\text{EW}} = \frac{g}{\sqrt{2}}W^+\sum_{\alpha=e,\mu,\tau}\bar{\nu}_\alpha\gamma^\mu P_L\ell_\alpha + \frac{g}{4c_w}Z \times\left\{\sum_{\alpha=e,\mu,\tau}\bar{\nu}_\alpha\gamma^\mu P_L\nu_\alpha + \sum_\alpha\bar{\ell}_\alpha\gamma^\mu\left[2s_w^2P_R - (1-2s_w^2)P_L\right]\ell_\alpha\right\} + h.c.\,, \tag{1.11}$$

where $c_w \equiv \cos\theta_w$, $s_w \equiv \sin\theta_w$, P_L and P_R are the left and right projectors, respectively, while ν_α and ℓ_α, are the neutrino and charged lepton weak eigenstates. The W^+ and Z^0 bosons are the massive gauge bosons of the weak interaction. The large boson masses $m_W \sim 80\,\text{GeV}$ and $m_Z \sim 90\,\text{GeV}$ result in a short range of the force of about 1×10^{-18} m. Interactions carried out by the $W^\pm$ bosons are called *charged current (CC)* interactions, as they propagate a charge, therefore changing the interacting lepton to its charged/neutral counterpart. *Neutral current (NC)* interactions are those mediated by the Z^0 boson, where no charge is transferred. NC interactions couple neutrinos to neutrinos and charged leptons to charged leptons, but not to each other. The Feynman diagrams for CC and NC interactions are shown in Figure 1.1.

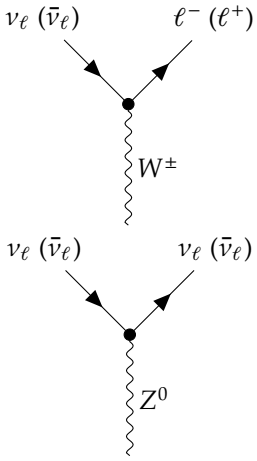

Figure 1.1: Feynman diagrams of charged-current (top) and neutral-current (bottom) neutrino weak interactions, modified from [13].

1.2 Beyond the Standard Model

The fundamentals of the SM described above **are not** enough to explain all observed phenomena. The SM is unable to account for gravity, as it

is incompatible with general relativity. Similarly, it fails to explain some cosmological observations like *dark matter (DM)*, and the matter-antimatter asymmetry in the universe. But most importantly, the SM does not predict neutrinos to have mass, which on the contrary is experimentally proven by to observation of neutrino oscillations, so some extension to the SM is needed to complete the full picture.

write short paragraph about dark matter here! (RED)

The standard cosmological model ΛCDM [14] assumes that equal amounts of matter and anti-matter were produced in the early universe. However, the universe today is dominantly made up of matter. This *baryon asymmetry of the universe (BAU)* can be measured by the difference between the number densities of baryons and anti-baryons normalized to the number density of photons as

$$\eta_B = \frac{n_B - n_{\bar{B}}}{n_\gamma} \,, \tag{1.12}$$

where n_B, $n_{\bar{B}}$, and n_γ are the number densities of baryons, anti-baryons, and photons, respectively. Baryons are the dominant component with η_B being observed to be at the order of 10^{-9} [15]. Leptogenesis and EW baryogenesis are scenarios that could explain this phenomenon, where the former could be realized by the existence of heavy RH neutrinos [16].

The observation of neutrino flavor conversions and neutrino oscillations in a multitude of experiments [17–19] is the strongest evidence for physics *beyond the standard model (BSM)* measured in laboratories to date. The observation that neutrinos change their flavor while they propagate through space can only be explained, if at least two neutrinos have a non-zero mass. From those measurements we know the mass differences are very small as compared to the lepton masses, but neither their existence, nor their smallness is predicted by the SM. There are upper limits on the sum of all neutrino masses from cosmological observations at 1.2 eV [20, 21] and at 0.8 eV from the KATRIN experiment [22]. Adding RH neutrino states to the theory could explain the origin of the observed non-zero neutrino masses and could be tested for by searching for corresponding signatures in experiments.

[14]: Deruelle et al. (2018), *Relativity in Modern Physics*

[15]: Workman et al. (2022), "Review of Particle Physics"

[16]: Fukugita et al. (1986), "Baryogenesis without grand unification"

[17]: Davis et al. (1968), "Search for Neutrinos from the Sun"

[18]: Fukuda et al. (1998), "Evidence for Oscillation of Atmospheric Neutrinos"

[19]: Ahmad et al. (2002), "Direct Evidence for Neutrino Flavor Transformation from Neutral-Current Interactions in the Sudbury Neutrino Observatory"

[20]: Alam et al. (2021), "Completed SDSS-IV extended Baryon Oscillation Spectroscopic Survey: Cosmological implications from two decades of spectroscopic surveys at the Apache Point Observatory"

[21]: Aghanim et al. (2020), "Planck2018 results: VI. Cosmological parameters"

[22]: Aker et al. (2022), "Direct neutrino-mass measurement with sub-electronvolt sensitivity"

1.2.1 Mass Mechanisms

Since there are no RH neutrinos in the SM, the mass mechanism described in Section 1.1.3, which couples the Higgs field to LH and RH Weyl fields, predicts the LH neutrinos to be massless. From experimental observations it is known that at least two of the three neutrino generations need to have a non-zero mass. Assuming the existence of RH neutrinos fields ν_R, one way of producing the neutrino masses is by adding a Yukawa coupling term similar to the one for up-type quarks mentioned in Section 1.1.3, to write the full Yukawa Lagrangian as

$$\mathcal{L}_{\text{Yukawa}} = -Y^e_{ij} \bar{L}^i_L \Phi e^j_R - Y^\nu_{ij} \bar{L}^i_L \tilde{\Phi} \nu^j_R + h.c. \,, \tag{1.13}$$

with i, j running over the three generations of leptons e, μ, and τ, and Y^e and Y^ν being the Yukawa coupling matrices. Diagonalizing the Yukawa coupling matrices through unitary transformations U^e and U^ν leads to the **Dirac mass term** in the mass basis as

$$\mathcal{L}^{\text{mass}}_{\text{Dirac}} = \frac{v}{\sqrt{2}} \left(\bar{e}_L M_e e_R - \bar{\nu}_L M_\nu \nu_R \right) \,, \tag{1.14}$$

where M_e and M_ν are the diagonal mass matrices of leptons and neutrinos, respectively. A purely Dirac mass term would not explain the smallness of the neutrino masses in a straightforward way. Only fine-tuning the Yukawa coupling constants to small values would lead to small neutrino masses.

An additional way of generating neutrino masses is by adding a Majorana mass term of the form

$$\mathcal{L}_{\text{Majorana}} = -\frac{1}{2} M_{ij} (\nu_R^i)^c \nu_R^j + h.c. \,, \tag{1.15}$$

with M_{ij} being the Majorana mass matrix and the indices i, j running over all n_R RH neutrino generations. The superscript c denotes the charge conjugate field. Combining the charge conjugated RH neutrino fields with the LH neutrino fields as

$$\boldsymbol{N} = \begin{pmatrix} \boldsymbol{\nu}_L \\ \boldsymbol{\nu}_R^c \end{pmatrix} , \tag{1.16}$$

with $\boldsymbol{\nu}_R$ containing the n_R RH fields. The full neutrino mass Lagrangian is then given by the combined **Dirac and Majorana mass term** as

$$\mathcal{L}^{\text{mass},\nu}_{\text{Dirac+Majorana}} = \frac{1}{2} \boldsymbol{N}^T \hat{C} M^{\text{D+M}} \boldsymbol{N} + h.c. \,, \tag{1.17}$$

and the mass matrix is given by

$$M^{\text{D+M}} = \begin{pmatrix} 0 & (M^D)^T \\ M^D & M^R \end{pmatrix} . \tag{1.18}$$

On top of explaining the origin of neutrino masses itself, a combined Dirac and Majorana mass term could also solve the question of their smallness. If the mass of the RH neutrinos is very large, the masses of the active neutrino flavors is suppressed, which is known as *see-saw mechanism*.

blabla, write this part properly!

add Majorana condition and mention what this means for interactions (LNV of 2) (RED)

Discuss lepton number conservation LNC (pure dirac) and lepton number violation (dirac+majorana) LNV, also mention how this isn't solved, yet! (RED)

copilot: depending on the type of mass term, the neutrinos are either Dirac or Majorana particles. The difference between the two is that Dirac neutrinos are distinct from their antiparticles, while Majorana neutrinos are their own antiparticles. The question of the nature of neutrinos is still open and could be answered by the observation of neutrinoless double beta decay, which is only possible if neutrinos are Majorana particles. The observation of neutrinoless double beta decay would also imply that the lepton number is not conserved, which would be a strong hint for physics beyond the standard model. The search for neutrinoless double beta decay is a very active field of research, as it could answer some of the most fundamental questions in particle physics.

lepton number conservation (LNC) lepton number violation (LNV)

1.2.2 Minimal Extensions and the νMSM

So far we have described neutrinos in their flavor eigenstates, which are relevant for weak interactions, where the three weak flavor states ν_e, ν_μ, and ν_τ are related to the charged leptons they interact with in CC interactions. In order to *just* explain the three oscillating flavor eigenstates, three mass states are needed, which are related to the flavor eigenstates by the unitary,

3x3 *Pontecorvo-Maki-Nakagawa-Sakata (PMNS)* mixing matrix U, where the flavor states are a superposition of the mass states as

$$|\nu_\alpha\rangle = \sum_k U^*_{\alpha k} |\nu_k\rangle \ , \tag{1.19}$$

with the weak flavor states $|\nu_\alpha\rangle$, $\alpha = e, \mu, \tau$, and the mass states $|\nu_k\rangle$ with $k = 1, 2, 3$. In its generic form the PMNS matrix is given by

$$U = \begin{pmatrix} U_{e1} & U_{e2} & U_{e3} \\ U_{\mu 1} & U_{\mu 2} & U_{\mu 3} \\ U_{\tau 1} & U_{\tau 2} & U_{\tau 3} \end{pmatrix} , \tag{1.20}$$

which will be the basis for the discussion of neutrino oscillations in Section 1.3.2.

This however is not enough to explain the neutrino masses observed in oscillation experiments. The most minimal model required to give rise to two non-zero active neutrino masses, is an additional two RH neutrinos, assuming the mass of the lightest SM neutrino is zero. If the additional neutrino states have masses $\gg$eV they are referred to as *heavy neutral leptons (HNLs)*, which are almost sterile, with a small mass mixing with the active neutrinos.

But the SM also fails to explain additional observations of physics beyond the standard model (BAU, DM), which could be solved by the *neutrino minimal standard model (νMSM)* [23, 24]. In the νMSM, three RH neutrinos are added, where two of them are heavy, to explain the observed neutrino masses and oscillations, and a third one is light and serves as a DM candidate. The mixing between mass and flavor eigenstates is then described by an extended 6x6 mixing matrix as

[23]: Asaka et al. (2005), "The nuMSM, dark matter and neutrino masses"
[24]: Asaka et al. (2005), "The νMSM, dark matter and baryon asymmetry of the universe"

elaborate on Leptogenesis in νMSM and sterile neutrino DM, or link some papers? (RED)

$$\begin{pmatrix} \nu_e \\ \nu_\mu \\ \nu_\tau \\ N_1 \\ N_2 \\ N_3 \end{pmatrix} = \begin{pmatrix} U_{e1} & U_{e2} & U_{e3} & U_{e4} & U_{e5} & U_{e6} \\ U_{\mu 1} & U_{\mu 2} & U_{\mu 3} & U_{\mu 4} & U_{\mu 5} & U_{\mu 6} \\ U_{\tau 1} & U_{\tau 2} & U_{\tau 3} & U_{\tau 4} & U_{\tau 5} & U_{\tau 6} \\ U_{N_1 1} & U_{N_1 2} & U_{N_1 3} & U_{N_1 4} & U_{N_1 5} & U_{N_1 6} \\ U_{N_2 1} & U_{N_2 2} & U_{N_2 3} & U_{N_2 4} & U_{N_2 5} & U_{N_2 6} \\ U_{N_3 1} & U_{N_3 2} & U_{N_3 3} & U_{N_3 4} & U_{N_3 5} & U_{N_3 6} \end{pmatrix} \begin{pmatrix} \nu_1 \\ \nu_2 \\ \nu_3 \\ \nu_4 \\ \nu_5 \\ \nu_6 \end{pmatrix} , \tag{1.21}$$

where N_i and ν_{i+3} ($i \in 1, 2, 3$) are the sterile flavor states and the additional RH mass states, respectively. In the νMSM, the two heavy RH neutrinos generate the active neutrino masses through the type I seesaw mechanism [25–29]. This refers to a model, where the HNLs are assumed to be SM scalars and get their mass trough coupling to the Higgs as in Section **??**. Naturally, more complex theories also exist, but are beyond the scope of this thesis and will not be discussed further.

[25]: Minkowski (1977), "$\mu \to e\ \gamma$ at a rate of one out of 10^9 muon decays?"
[26]: Yanagida (1980), "Horizontal Symmetry and Masses of Neutrinos"
[27]: Glashow (1980), "The Future of Elementary Particle Physics"
[28]: Gell-Mann et al. (1979), "Complex Spinors and Unified Theories"
[29]: Mohapatra et al. (1980), "Neutrino Mass and Spontaneous Parity Nonconservation"

With this extension, the leptonic part of the EW Lagrangian from Equation 1.11 now reads

$$\mathscr{L}^{\ell}_{ext.EW} = \frac{g}{\sqrt{2}} W^+ \sum_\alpha \sum_i U^*_{\alpha i} \bar{\nu}_i \gamma^\mu P_L \ell_\alpha + \frac{g}{4 c_w} Z \times \left\{ \sum_{i,j} C_{ij} \bar{\nu}_i \gamma^\mu P_L \nu_j + \sum_\alpha \bar{\ell}_\alpha \gamma^\mu \left[2 s_w^2 P_R - (1 - 2 s_w^2) P_L \right] \ell_\alpha \right\} + h.c. \ , \tag{1.22}$$

with

$$C_{ij} \equiv \sum_{\alpha} U^*_{\alpha i} U_{\alpha j} \ , \tag{1.23}$$

and the indices α and i now summing over all $(3 + n)$ flavor and mass states, respectively. If only mixing between one SM flavor, α, and one RH neutrino mass state, i, is non-zero $C_{ii} = |U_{\alpha i}|^2 \neq 0$, coupling terms of the form

$$\mathscr{L}^{\ell}_{\mathrm{EW}} \supset \frac{g}{\sqrt{2}} W^+ |U_{\alpha i}|^2 \bar{\nu}_i \gamma^\mu P_L \ell_\alpha \ , \tag{1.24}$$

and

$$\mathscr{L}^{\ell}_{\mathrm{EW}} \supset \frac{g}{4 c_w} Z |U_{\alpha i}|^2 \bar{\nu}_i \gamma^\mu P_L \nu_i + h.c. \ , \tag{1.25}$$

are present. Those are the CC and NC interactions between the HNL and the SM neutrinos, which are the basis for the searches for HNLs in experiments, as will be discussed in the following.

1.2.3 Observational Avenues for Right-Handed Neutrinos

If the RH neutrinos have masses at the eV scale, they can be observed through distortion effects in measurements of neutrino oscillation experiments. Several analyses looking for these so-called light sterile neutrinos exist in *IceCube*, where [30] is using atmospheric neutrinos in the higher energy range of 500 GeV to 10 000 GeV and [13] is using the lower energy region of 6 GeV to 156 GeV. The latter work includes a detailed description of the expected oscillation effects and the various anomalies observed in oscillation experiments that could be explained by the existence of a light sterile neutrino, which is not covered in this work.

[30]: Aartsen et al. (2020), "eV-Scale Sterile Neutrino Search Using Eight Years of Atmospheric Muon Neutrino Data from the IceCube Neutrino Observatory"

[13]: Trettin (2023), "Search for eV-scale sterile neutrinos with IceCube DeepCore"

Here, the focus will be on heavy RH neutrinos, interchangeably also called heavy sterile neutrinos, or HNLs. A defining property is that they are too massive to be produced in oscillations and to be observed as distortions thereof. Several ways to observe HNLs are possible through direct production and decay experiments, which will be discussed in the following. Most of the existing searches assume the minimal model, where only one coupling between the new mass states and the SM neutrinos is non-zero and the coupling is just through mass mixing in a type I seesaw scenario, but more complex scenarios are of course also possible and might produce various additional signatures, or stronger signals.

In general, the constraints discussed in the following are based on models, where only the coupling between the HNL and one SM flavor is non-zero. While this is the straight forward approach to test the mixing parameters individually, this might make the constraints stronger than they would be in a more complex scenario, where the HNLs couple to more than one SM flavor as was show in [31] for collider bounds.

[31]: Tastet et al. (2021), "Reinterpreting the ATLAS bounds on heavy neutral leptons in a realistic neutrino oscillation model"

Extracted Beamline Searches

Protons interacting with a target or a beam dump can produce pions, kaons, and heavy-quark hadrons, whose subsequent decays would also produce HNLs. Depending on the HNL lifetime in the specific model, the mass of the HNLs produced in beam dump experiments would be between 1 MeV and 4 GeV and they could decay at distances across several

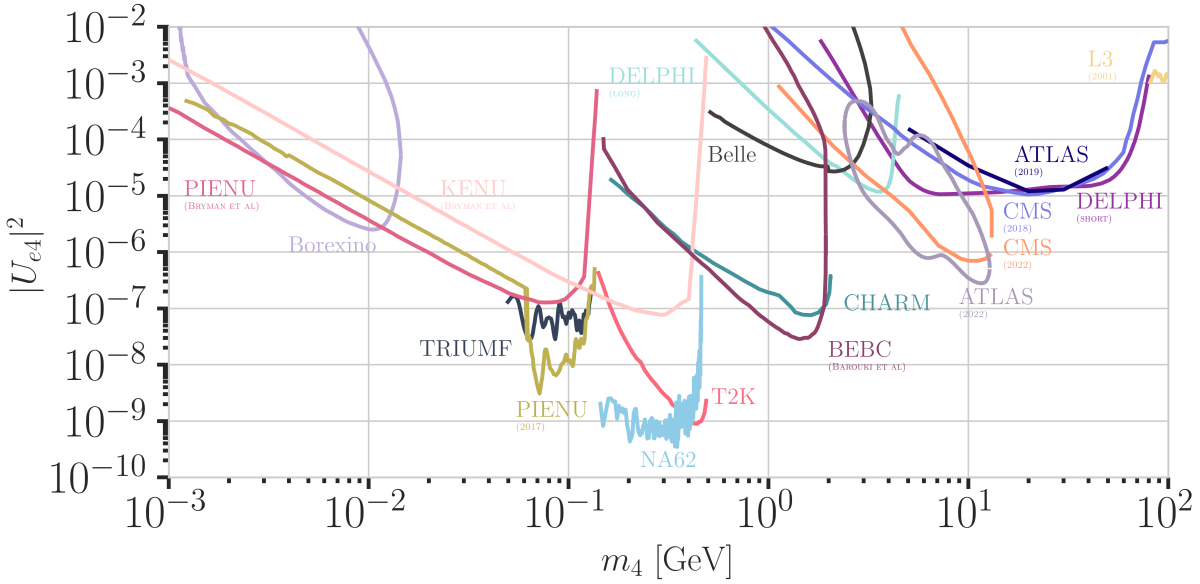

Figure 1.2: Current leading $|U_{e4}^2| - m_4$ upper limits from PIENU [32, 33], BOREXINO [34], KENU [32], TRIUMF [35], NA62 [36], T2K [37], DELPHI [38], BEBC [39], Belle [40], L3 [41], CHARM [42], ATLAS [43, 44], CMS [45, 46], and NuTeV [47]. Modified from [48].

orders of magnitude, Experiments along the extracted beamline, which are using a spectrometer with particle identification, can search for unique decay signatures at displaced vertices. Example signatures[1] are $\nu_4 \to l_\alpha \pi^+$, $\nu_4 \to \nu_\alpha l_\beta^+ l_\beta^-$, or $\nu_4 \to \nu_\alpha \pi^0$ (or other neutral mesons) that cannot be explained by SM neutrinos. Here, ν_α and l_α are the SM neutrino and charged lepton of flavor $\alpha \in \{e, \mu, \tau\}$, defined by which flavor the HNL couples to. l_β^-/l_β^+ is a charged lepton/antilepton pair of any flavor $\beta \in \{e, \mu, \tau\}$. Depending on the decay channel, a specific mixing can be probed. The other way of searching for HNLs with these interactions is to look for peaks in the missing mass spectrum, measured around the production vertex at the target, which usually is not possible for beam dumps, as the beam dump region is not calorimetrically instrumented. The HNL searches were pioneered by experiments at extracted beamlines, with *PS191* [49] and *CHARM* [42] establishing upper limits on $|U_{e4}|^2$, $|U_{\mu 4}|^2$, and combinations of them, at masses from 10 MeV to 500 MeV at orders of 10^{-3} to 10^{-6}. Since then, there has been and still is a large activity of searches for HNLs at extracted beamlines and at the lower mass end, the strongest bounds on $|U_{e4}|^2$ are set by *PIENU* [32] at $\sim (10^{-4})$ around 2 MeV, and at the higher mass end, the strongest bounds are set by *NA62* [36], reaching down to $\sim 10^{-9}$ at 0.3 GeV. For $|U_{\mu 4}|^2$, the strongest bounds up to 10 GeV are set by *PSI* [50] at $\sim 10^{-5}$, and reach down to $\sim (10^{-9})$ at 0.3 GeV, by *BNL-E949* [51]. The current strongest bounds are shown in Figure 1.2 and Figure 1.3, where bounds from other type of experiments are also presented. Those will be discussed in the following.

Especially noteworthy are the results of analyses probing the mixing with the third lepton generation, $|U_{\tau 4}|^2$, from *NOMAD* [52] and reinterpretations of the CHARM results and the BEBC results in the context of the mixing $|U_{\tau 4}|^2$, where the latter places the most stringent limits from 10^{-3} to 10^{-6} in the 0.1 GeV to 2 GeV range [39, 53, 54]. In Figure 1.4 the current strongest bounds on $|U_{\tau 4}|^2$ are shown.

1: The explicit channels and their decay width calculations used in this thesis are explained in detail in Section 2.2.1.

[49]: Bernardi et al. (1986), "Search for Neutrino Decay"

[42]: Bergsma et al. (1983), "A Search for Decays of Heavy Neutrinos"

[32]: Bryman et al. (2019), "Constraints on Sterile Neutrinos in the MeV to GeV Mass Range"

[36]: Parkinson et al. (2022), "Search for heavy neutral lepton production at the NA62 experiment"

[50]: Daum et al. (1987), "Search for Admixtures of Massive Neutrinos in the Decay $\pi^+ \to \mu^+$ Neutrino"

[51]: Artamonov et al. (2015), "Search for heavy neutrinos in $K^+ \to \mu^+ \nu_H$ decays"

[52]: Astier et al. (2001), "Search for heavy neutrinos mixing with tau neutrinos"

[39]: Barouki et al. (2022), "Blast from the past II: Constraints on heavy neutral leptons from the BEBC WA66 beam dump experiment"

[53]: Orloff et al. (2002), "Limits on the mixing of tau neutrino to heavy neutrinos"

[54]: Boiarska et al. (2021), "Constraints from the CHARM experiment on heavy neutral leptons with tau mixing"

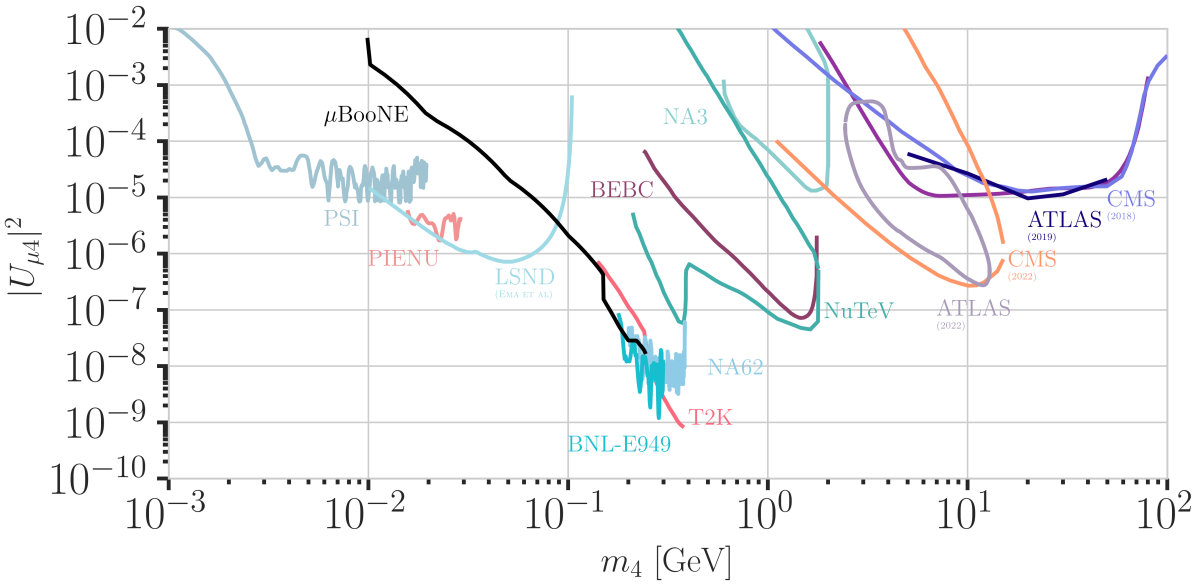

Figure 1.3: Current leading $|U^2_{\mu 4}| - m_4$ upper limits from PSI [50], μBooNE [55], PIENU [32], LSND [56], BNL-E949 [51], NA62 [36], T2K [37], BEBC [57], ATLAS [43, 44], CMS [45, 46], NuTeV [47], and NA3 [58]. Modified from [48].

Collider Searches

So far, collider searches have been conducted at the *large electron positron collider (LEP)* and at the *large hadron collider (LHC)* in proton-proton mode. Strongest results are from the *ATLAS* and *CMS* experiments, which are nearly hermetic, general purpose detectors around the interaction point, and from the *DELPHI* and the *LHCb* experiments, which are forward detectors that can be used to search for new particles in decays of heavy particles produced. In the minimal model, HNLs in the GeV mass range can be produced through mass mixing in decays of heavy mesons, tau leptons, Z/W bosons, H bosons, or top quarks originating from the collisions. Depending on the dirac or majorana nature of the HNL, they can decay to lepton number conserving or lepton number violating channels.

Using prompt and displaced decays of the HNL, both ATLAS and CMS have set constraints on $|U_{e4}|^2$ and $|U_{\mu 4}|^2$ at the level of 10^{-4} to 10^{-6} in the mass range between 1 GeV to 100 GeV [43–46]. The LHCb experiment has HNL search results at HNL masses below and above the W boson mass, where the low mass searches are using the decay channel $B^- \to \pi^+\mu^-\mu^-$, setting limits at the 10^{-3} level for $|U_{\mu 4}|^2$ in the mass range of 0.5 GeV to 3.5 GeV [59]. At high masses, the $W^+ \to \mu^-\mu^{\pm}$jet channel is used to set limits at the order of 10^{-3} to 10^{-2} for $|U_{\mu 4}|^2$ in the mass range of 5 GeV to 50 GeV in the LNC channel and at the order of 10^{-4} to 10^{-3} in the LNV channel [60]. Using hadronic Z^0 decays, searches for short- and long-lived HNLs have been conducted with the *DELPHI* detector setting upper limits of the order of 10^{-5} for mixing to any SM flavor in the mass range from 3.5 GeV to 50 GeV [38].

Nuclear Decays Measurements

A novel approach of searching for irregularities in energy-momentum conservation measurements in nuclear reactions might be a viable way of

[43]: Aad et al. (2019), "Search for heavy neutral leptons in decays of W bosons produced in 13 TeV pp collisions using prompt and displaced signatures with the ATLAS detector"

[44]: Aad et al. (2023), "Search for Heavy Neutral Leptons in Decays of W Bosons Using a Dilepton Displaced Vertex in $\sqrt{s}$ = 13TeV pp Collisions with the ATLAS Detector"

[45]: Sirunyan et al. (2018), "Search for heavy neutral leptons in events with three charged leptons in proton-proton collisions at $\sqrt{s}$ = 13 TeV"

[46]: Tumasyan et al. (2022), "Search for long-lived heavy neutral leptons with displaced vertices in proton-proton collisions at $\sqrt{s}$ =13 TeV"

[59]: Shuve et al. (2016), "Revision of the LHCb Limit on Majorana Neutrinos"

[60]: Aaij et al. (2021), "Search for heavy neutral leptons in $W^+ \to \mu^+\mu^{\pm}$jet decays"

[38]: Abreu et al. (1997), "Search for neutral heavy leptons produced in Z decays"

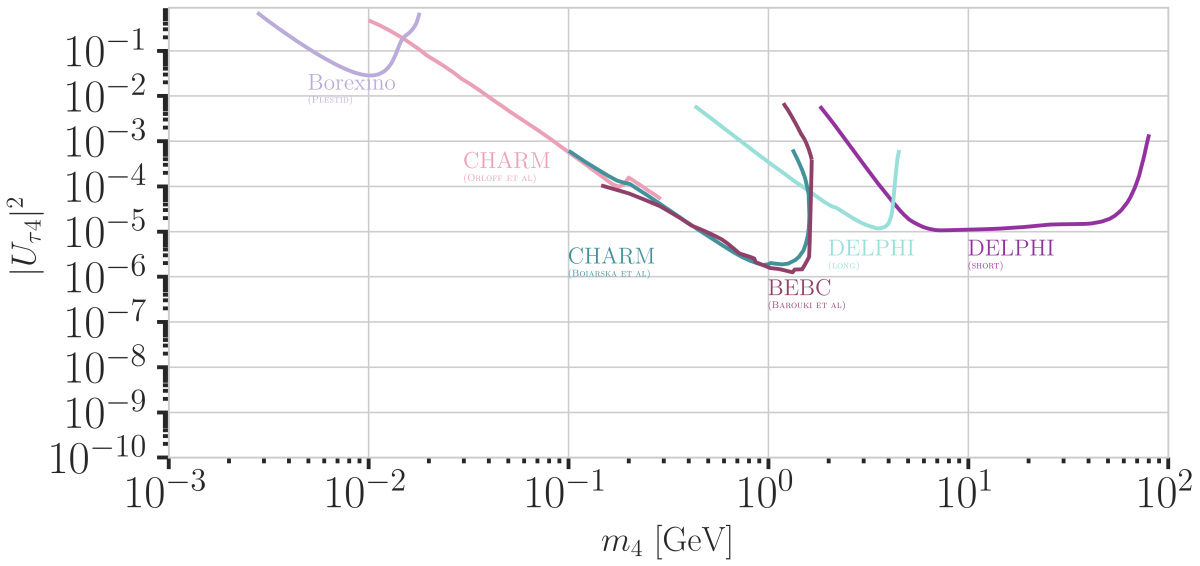

Figure 1.4: Current leading $|U_{\tau 4}^2| - m_4$ upper limits from BOREXINO [61], CHARM [53, 54], DELPHI [38], and BEBC [39]. Modified from [48].

searching for HNLs, as they could be interpreted as constraints on $|U_{e4}|^2$ and m_4.

Kinks in **beta decay** spectra would show up at $Q - m_4c^2$, where the HNL mass, m_4, can be measured between the lower energy detection threshold and the energy released in the decay, which is called Q value. Analyses using the tritium decay, with $Q = 18.6\,\text{keV}$, are planned in *KATRIN* [62] and *TRISTAN* [63] in the 1 keV to 18 keV range. Their projected statistical limits are around 10^{-7} for $|U_{e4}|^2$, but will require further detector upgrades [63]. A first result from KATRIN measurements during commissioning sets limits at the order of 10^{-2} to 10^{-3} in the mass range of 0.1 keV to 1.6 keV [64]. *DUNE* is planning to measure the ionization charge of atmospheric argon decays, with $Q = 565\,\text{keV}$, to probe $|U_{e4}|^2$ at in the 20 keV to 450 keV mass range. The projected sensitivity is at the 10^{-5} level, and might improve to 10^{-7} with additional detector improvements [65].

To test for the existence of HNLs using **electron capture** measurements, total energy-momentum reconstruction of all non-neutrino final states is needed. Electron capture is a pure two-body decay process, where the recoiling atom and the electron neutrino are the only final state particles, but additional energy is carried away by the de-excitation x-ray or auger electron. The energy-momentum conservation can be probed by measuring the atom and the associated de-excitation products. The mixing $|U_{e4}|^2$ can be probed by looking for a separated non-zero missing mass peak. The *BeEST* experiment has set limits at the 10^{-4} level in the 100 keV to 850 keV mass range, using berillium-7, which has a Q value of 862 keV. After planned upgrades to the experiment, the sensitivity is expected to improve to the 10^{-7} level [66].

Reactor searches up to 12 MeV in mass are possible at short baseline experiments using commercial or research reactors, which are a strong source of electron antineutrinos and could therefore also produce HNLs if $|U_{e4}|^2$ is non-zero. Visible decay channels at these energies are $\nu_4 \to \nu_e e^+ e^-$, $\nu_4 \to \nu\gamma$, and $\nu_4 \to \nu\gamma\gamma$, where the first dominates. The first analysis in

[62]: Osipowicz et al. (2001), "KATRIN: A Next generation tritium beta decay experiment with sub-eV sensitivity for the electron neutrino mass. Letter of intent"

[63]: Mertens et al. (2019), "A novel detector system for KATRIN to search for keV-scale sterile neutrinos"

[64]: Aker et al. (2023), "Search for keV-scale sterile neutrinos with the first KATRIN data"

[65]: Abi et al. (2020), "Deep Underground Neutrino Experiment (DUNE), Far Detector Technical Design Report, Volume II: DUNE Physics"

[66]: Friedrich et al. (2021), "Limits on the Existence of sub-MeV Sterile Neutrinos from the Decay of ^{7}Be in Superconducting Quantum Sensors"

this field, reports limits at the 10^{-4} level in the 2 MeV to 7 MeV mass range [67].

[67]: Hagner et al. (1995), "Experimental search for the neutrino decay v3+vj+e++e- and limits on neutrino mixing"

Atmospheric and Solar Neutrinos

Natural sources of neutrinos are provided up to 20 MeV by the sun and up to 100s of GeV by neutrino production in the atmosphere. Both fluxes contain all flavors of neutrinos, due to mixing and oscillations, and can therefore be used to directly probe the mixings with ν_e, ν_μ, and ν_τ. Depending on the HNL mass and the strength of the mixing, which both govern the decay length, different signatures can be used to experimentally access large regions of the HNL parameter space. The strength of the mixing determines the total rate of HNL events, which is additionally affected by whether solely the minimal mass mixing is assumed, or also more complicated mixing scenarios, like the dipole portal, are considered.

So far, only very few analyses exist, which are performed by the experimental collaborations themselves. Several external theoretical groups have predicted the expected sensitivities to HNLs, produced from solar or atmospheric neutrinos, based on various coupling scenarios and decay lengths. A selection of the potential analyses will be discussed in the following.

For very long-lived particles, **production inside the sun** can be used as a source to search for HNLs in detectors on earth. This will only allow production through non-zero $|U_{e4}|^2$, because the initial solar neutrino flux is only ν_e. By searching for HNL decays to a SM neutrino and an electron positron pair $\nu_4 \to \nu_e e^+ e^-$ and comparing to the expected inter planetery positron flux, *Borexino* has placed the strongest limits on the mixing $|U_{e4}|^2$ at the order of 10^{-5} in the few MeV mass range [34].

[34]: Bellini et al. (2013), "New limits on heavy sterile neutrino mixing in B8 decay obtained with the Borexino detector"

For HNL decay length scales of the order of the Earth's diameter, HNL **up-scattering outside the detector** is possible, where a neutrino from the solar or the atmospheric neutrino flux scatters in the Earth and transfers some kinetic energy to the HNL, which can then later decay inside the detector. For HNL masses below 18 MeV produced from solar neutrinos, limits were derived using the Borexino data for purely tau coupling through mass mixing [61] and for all flavor coupling through the dipole portal [68]. At similar decay length scales, the HNL could also be produced directly in the atmosphere, but neither this channel, nor the production anywhere in the Earth from atmospheric neutrinos has been investigated yet.

[61]: Plestid (2021), "Luminous solar neutrinos I: Dipole portals"

[68]: Plestid (2021), "Luminous solar neutrinos II: Mass-mixing portals"

If the HNL decay lengths are sufficiently short, **production and decay in the detector** can happen and the observation of two vertices could be used to constrain the mixing parameters. In principle, this could be possible with any neutrino flavor produced in the sun or the atmosphere, but so far only theoretical studies have been performed for mass-mixing and dipole-portal couplings for the atmospheric neutrino detectors IceCube [69, 70] and *Super-K*, *Hyper-K*, and Dune [71, 72]. Due to the high complexity of these experiments, several simplified assumptions were made in the studies, which might not hold in reality, and the results should be taken with caution. For reliable sensitivity estimates and limits the collaborations should perform their own analyses.

[69]: Coloma et al. (2017), "Double-Cascade Events from New Physics in Icecube"

[70]: Coloma (2019), "Icecube/DeepCore tests for novel explanations of the MiniBooNE anomaly"

[71]: Atkinson et al. (2022), "Heavy Neutrino Searches through Double-Bang Events at Super-Kamiokande, DUNE, and Hyper-Kamiokande"

[72]: Coloma et al. (2021), "GeV-scale neutrinos: interactions with mesons and DUNE sensitivity"

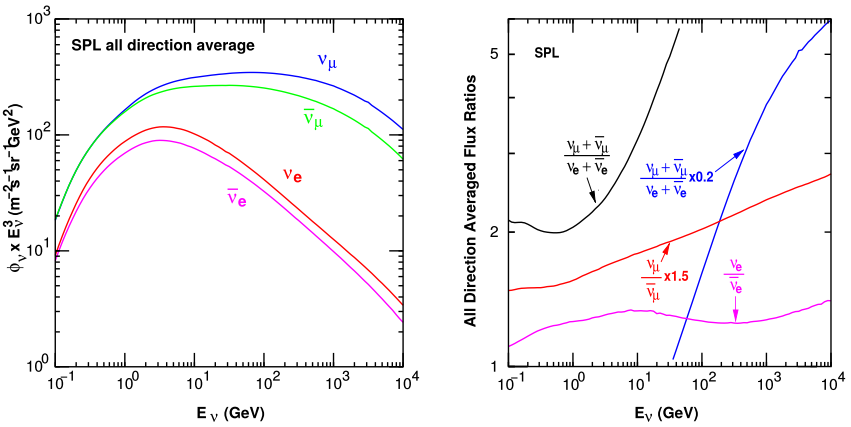

Figure 1.5: The atmospheric fluxes of different neutrino flavors as a function of energy (left) and the ratios between muon neutrinos and electron neutrinos as well as the ratios between neutrinos and antineutrinos for both those flavors (right). Results from the calculations performed for the geographic South Pole, taken from [74].

1.3 Atmospheric Neutrinos as Source of Heavy Neutral Leptons

This work focuses on the search for HNLs using atmospheric neutrinos as source for the production and decay inside the IceCube detector. The following sections will give a brief overview of the production of neutrinos in the atmosphere and the oscillations they undergo, before discussing the expected signatures of HNLs in the detector, where they are produced from the incoming neutrinos and subsequently decay.

1.3.1 Production of Neutrinos in the Atmosphere

[73]: Tanabashi et al. (2018), "Review of Particle Physics"

The analysis performed in this work is based on the sample of neutrinos observed in IceCube DeepCore at energies below 100 GeV. At these energies, the flux exclusively originates in the Earth's atmosphere. Highly relativistic cosmic rays (protons and heavier nuclei [73]) interact in the upper atmosphere, producing showers of secondary particles. Neutrinos are produced in decays of charged pions and kaons (π and K mesons) present in those showers, where the dominant contribution comes from the decay chain

$$\begin{aligned} \pi^\pm &\rightarrow \mu^\pm + \nu_\mu(\bar{\nu}_\mu) \,, \\ \mu^\pm &\rightarrow e^\pm + \bar{\nu}_\mu(\nu_\mu) + \nu_e(\bar{\nu}_e) \,, \end{aligned} \tag{1.26}$$

where muon neutrinos ν_μ and muons $\mu^\pm$ are produced in the first decay and both electron and muon neutrinos $\nu_{e/\mu}$ are produced in the second decay. Atmospheric muons, which are also produced in these decays, are the main background component for IceCube DeepCore analyses.

The different atmospheric flux components are shown in Figure 1.5 (left), for a much broader energy range than relevant for this work. Both neutrinos and antineutrino fluxes are shown for electron and muon neutrinos and all fluxes are the directionally averaged expectation calculated at the South Pole. Muon neutrinos are dominating the flux and from Equation 1.26 the naive assumption would be that the ratio between muon and electron neutrinos is $(\nu_\mu + \bar{\nu}_\mu)/(\nu_e + \bar{\nu}_e) = 2$. This is roughly true at energies below 1 GeV, where all muons decay in flight, but at larger energies muons can reach the detector before decaying, which increases the ratio to approximately 10:1 at around 100 GeV. Additionally, kaon decays start to contribute which also increases the number of muons and muon neutrinos. The increasing ratio can be

seen in Figure 1.5 (right), which also shows the ratio between neutrinos and antineutrinos for both flavors.

Charged mesons heavier than the tau can also be produced in cosmic ray interactions. Their decays to tau neutrinos or direct production of taus in cosmic ray interactions lead to the production of tau neutrinos. At the energies relevant for this work however, the resulting tau neutrino flux is negligible as compared to the muon neutrino flux [75] and is not considered in the analysis. This is because both charged mesons and tau particles are much heavier than pions and kaons and therefore their production is suppressed at high energies.

[75]: Fedynitch et al. (2015), "Calculation of conventional and prompt lepton fluxes at very high energy"

1.3.2 Neutrino Oscillations

Describing neutrinos in their mass state as introduced in Section **??** is crucial to understanding their propagation through space and time and to explaining neutrino oscillations. Oscillations mean that a neutrino changes from its initial flavor, that it was produced with, to another flavor and back after traveling a certain distance.

The neutrino propagation in vacuum can be expressed by applying a plane wave approach, where the mass eigenstates evolve as

$$|\nu_k(t)\rangle = e^{-iE_k t/\hbar} |\nu_k\rangle \ . \tag{1.27}$$

The energy of the mass eigenstate $|\nu_k\rangle$ is $E_k = \sqrt{\vec{p}^2c^2 + m_k^2c^4}$, with momentum $\vec{p}$ and mass m_k, $\hbar$ is the reduced Planck constant, and c is the speed of light in vacuum. A neutrino is produced as a flavor eigenstate $|\nu_\alpha\rangle$ in a CC weak interaction, but its propagation happens as the individual mass states it is composed of. The probability of finding the neutrino with initial flavor $|\nu_\alpha\rangle$ in the flavor state $\left|\nu_\beta\right\rangle$ after the time t is calculated as

$$P_{\nu_\alpha \to \nu_\beta}(t) = \left| \left\langle \nu_\beta | \nu_\alpha(t) \middle| \nu_\beta | \nu_\alpha(t) \right\rangle \right|^2 , \tag{1.28}$$

[76]: Dirac (1927), "The Quantum Theory of the Emission and Absorption of Radiation"

by applying Fermi's Golden Rule [76], which defines the transition rate from one eigenstate to another by the strength of the coupling between them. This coupling strength is the square of the matrix element and using the fact that the mixing matrix is unitary ($U^{-1} = U^\dagger$) to describe the mass eigenstates as flavor eigenstates, we find the time evolution of the flavor state $|\nu_\alpha(t)\rangle$, which can be inserted into Equation 1.28 to find the probability as

$$P_{\nu_\alpha \to \nu_\beta}(t) = \sum_{j,k} U^*_{\beta j} U_{\alpha j} U_{\beta k} U^*_{\alpha k} e^{-i(E_k - E_j)t/\hbar} \ . \tag{1.29}$$

The indices j and k run over the mass eigenstates.

We can approximate the energy as

$$E_k \approx E + \frac{c^4 m_k^2}{2E} \quad \longrightarrow \quad E_k - E_j \approx \frac{c^4 \Delta m_{kj}^2}{2E} \ , \tag{1.30}$$

for very small masses compared to the kinetic energy $E \gg m_k c^2$. Here, $\Delta m_{kj}^2 = m_k^2 - m_j^2$ is the mass-squared splitting between states k and j, and E is the energy of the wavepacket to be detected (flavor eigenstate). Replacing

the time in Equation 1.29 by the distance traveled by relativistic neutrinos $t \approx L/c$ we get

$$P_{\nu_\alpha \to \nu_\beta}(t) = \delta_{\alpha\beta} - 4 \sum_{j>k} \mathbf{Re}(U^*_{\beta j} U_{\alpha j} U_{\beta k} U^*_{\alpha k}) \sin^2\left(\frac{c^3 \Delta m^2_{kj}}{4E\hbar} L\right) + 2 \sum_{j>k} \mathbf{Im}(U^*_{\beta j} U_{\alpha j} U_{\beta k} U^*_{\alpha k}) \sin^2\left(\frac{c^3 \Delta m^2_{kj}}{4E\hbar} L\right), \tag{1.31}$$

which is called the survival probability if $\alpha = \beta$, and the transition probability if $\alpha \neq \beta$. Once again, this probability is only non-zero if there are neutrino mass eigenstates with masses greater than zero. Additionally, there must be a mass-squared difference Δm^2 and non-zero mixing between the states. Since we assumed propagation in vacuum in Equation 1.27, the transition and survival probabilities correspond to vacuum mixing.

[73]: Tanabashi et al. (2018), "Review of Particle Physics"

The mixing matrix can be parameterized as [73]

$$U = \begin{pmatrix} 1 & 0 & 0 \\ 0 & c_{23} & s_{23} \\ 0 & -s_{23} & c_{23} \end{pmatrix} \begin{pmatrix} c_{13} & 0 & s_{13} e^{-i\delta_{CP}} \\ 0 & 1 & 0 \\ -s_{13} e^{i\delta_{CP}} & 0 & c_{13} \end{pmatrix} \begin{pmatrix} c_{12} & s_{12} & 0 \\ -s_{12} & c_{12} & 0 \\ 0 & 0 & 1 \end{pmatrix}, \tag{1.32}$$

where $c_{ij} = \cos\theta_{ij}$ and $s_{ij} = \sin\theta_{ij}$ are cosine and sine of the mixing angle θ_{ij}, that defines the strength of the mixing between the mass eigenstates i and j, and δ_{CP} is the neutrino CP-violating phase. Experiments are sensitive to different mixing parameters, depending on the observed energy range, neutrino flavor, and the distance between the source and the detector L, commonly referred to as *baseline*. To be able to resolve oscillations the argument

$$\frac{\Delta m^2 L}{4E} \tag{1.33}$$

should be at the order of 1. This divides experiments into ones that are sensitive to very slow oscillations from $\Delta m^2_{21} \approx \mathcal{O}(10^{-5}\text{eV}^2)$ and ones that are sensitive to faster oscillations from $\Delta m^2_{31} \approx \mathcal{O}(10^{-3}\text{eV}^2)$. Relevant for this work are the parameters that can be measured at the earths surface using atmospheric neutrinos, which are Δm^2_{31}, θ_{23}, and θ_{13}, because the flux is primarily composed of muon neutrinos and antineutrinos. Applying the parameterization from Equation 1.32 to Equation 1.31 and using the fact that θ_{13} is small and θ_{12} is close to $\pi/4$, the survival probability of muon neutrinos can be approximated as

$$\begin{aligned} P_{\nu_\mu \to \nu_\mu} &\simeq 1 - 4|U_{\mu 3}|^2(1 - |U_{\mu 3}|^2) \sin^2\left(\frac{\Delta m^2_{31} L}{4E}\right) \\ &\simeq 1 - \sin^2\left(2\theta_{23}\right) \sin^2\left(\frac{\Delta m^2_{31} L}{4E}\right), \end{aligned} \tag{1.34}$$

while the tau neutrino appearance probability is

$$\begin{aligned} P_{\nu_\mu \to \nu_\tau} &\simeq 4|U_{\mu 3}|^2 |U_{\tau 3}|^2 \sin^2\left(\frac{\Delta m^2_{31} L}{4E}\right) \\ &\simeq \sin^2\left(2\theta_{23}\right) \sin^2\left(\frac{\Delta m^2_{31} L}{4E}\right). \end{aligned} \tag{1.35}$$

Parameter	Global Fit
θ_{12} [°]	$33.41^{+0.75}_{-0.72}$
θ_{13} [°]	$8.54^{+0.11}_{-0.12}$
θ_{23} [°]	$49.1^{+1.0}_{-1.3}$
Δm^2_{21} [10^{-5}eV^2]	$7.41^{+0.21}_{-0.20}$
Δm^2_{31} [10^{-3}eV^2]	$2.511^{+0.028}_{-0.027}$
δ_{CP} [°]	197^{+42}_{-25}

Table 1.2: Results from the latest global fit of neutrino mixing parameters from [77].

[77]: Esteban et al. (2020), "The fate of hints: updated global analysis of three-flavor neutrino oscillations"

The latest global fit [77] of all the parameters is shown in Table 1.2.

1.3.3 Neutrino Interactions with Nuclei

The neutrino detection principle of IceCube DeepCore is explained in Chapter **??** and relies on the weak interaction processes between neutrinos and the nuclei of the Antarctic glacial ice. At neutrino energies above 5 GeV, the cross-sections are dominated by ***deep inelastic scattering (DIS)***, where the neutrino is energetic enough to resolve the underlying structure of the nucleons and interact with one of the composing quarks individually. As a result the nucleon breaks and a shower of hadronic secondary particles is produced. Depending on the type of interaction, the neutrino either remains in the final state for NC interactions or is converted into its charged lepton counterpart for CC interactions. The CC DIS interactions have the form

$$\begin{aligned} \nu_\alpha + N &\rightarrow l_\alpha^- + X \,, \\ \bar{\nu}_\alpha + N &\rightarrow l_\alpha^+ + X \,, \\ &\qquad , \end{aligned} \tag{1.36}$$

where $\nu_\alpha / \bar{\nu}_\alpha$ and l_α^- / l_α^+ are the neutrino/antineutrino and its corresponding lepton/antilepton for $\alpha = e, \mu, \tau$.N is the nucleon and X stands for any set of final state hadrons. The NC DIS interactions are

$$\begin{aligned} \nu_\alpha + N &\rightarrow \nu_\alpha + X \text{ and} \\ \bar{\nu}_\alpha + N &\rightarrow \bar{\nu}_\alpha + X \,. \end{aligned} \tag{1.37}$$

DIS interactions have a roughly linear energy dependent cross-section above ~20 GeV and are well measured and easy to theoretically calculate. They are the primary interaction channel for neutrinos detected with IceCube. Figure 1.6 shows the Feynman diagrams for both processes.

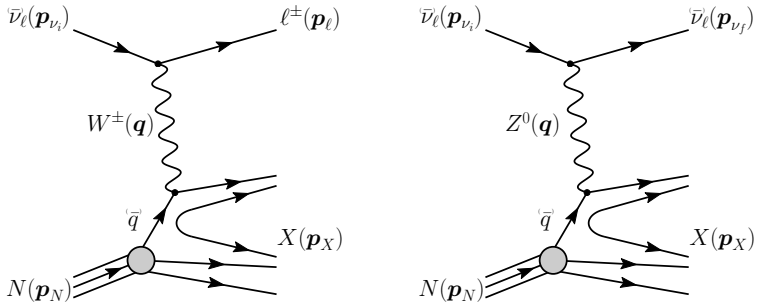

Figure 1.6: Feynman diagrams for deep inelastic scattering of a neutrino with a nucleon via charged-current (left) and neutral current (right) interactions. $\boldsymbol{p}_{\nu_i}$, $\boldsymbol{p}_N$ and $\boldsymbol{p}_{\nu_f}$, $\boldsymbol{p}_l$, $\boldsymbol{p}_N$ are the input and output four-momenta, while $\boldsymbol{q}$ is the momentum transfer. Taken from [78].

At energies below 5 GeV, ***quasi-elastic scattering (QE)*** and ***resonant scattering (RES)*** become important. At these energies the neutrinos interact with the approximately point-like nucleons, without breaking them up in the process. RES describes the process of a neutrino scattering off a nucleon producing an excited state of the nucleon in addition to a charged lepton. It is the dominant process from 1.5 GeV to 5 GeV for neutrinos and from 1.5 GeV to 8 GeV for antineutrinos. Below 1.5 GeV QE is the dominant process, where protons are converted to neutrons in antineutrino interactions and vice-versa for neutrino interactions. Additionally, a charged lepton corresponding to the neutrino/antineutrino flavor is produced. The cross-sections of QE and RES scattering processes are not linear in energy and the transition region from QE/RES to DIS is poorly understood. The total cross-sections and their composition is shown in Figure 1.7. It can be seen that the interaction cross-sections are very small at the order of 10^{-38} cm^2. This is the reason why very

large volume detectors are required to measure atmospheric neutrinos with sufficient statistics to perform precision measurements of their properties.

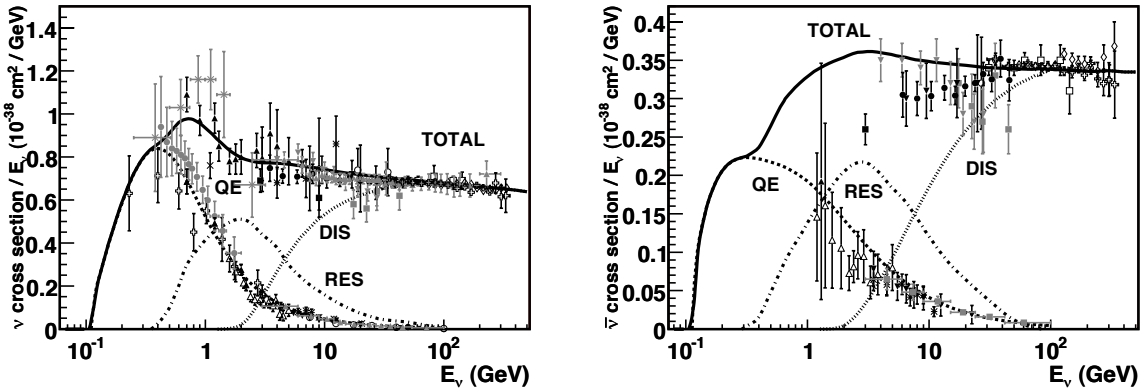

Figure 1.7: Total neutrino (left) and antineutrino (right) per nucleon cross-section divided by neutrino energy plotted against energy. The three main scattering processes quasi-elastic scattering (QE), resonant scattering (RES), and deep-inelastic scattering (DIS) are shown. Taken from [79].

1.3.4 Heavy Neutral Lepton Production and Decay

For the search conducted in this work, both production and decay of the HNL are assumed to happen inside the detector, therefore probing decay lengths ranges at the scale of the detector size, which is below 1000 m. Since the mixing with the first two generations of leptons is already strongly constrained as was discussed in Section 1.3, only the mixing with the tau neutrino will be considered in the following. Due to the effect of oscillations, described in Section 1.3.2, the initial atmospheric muon neutrino flux provides a sizable tau neutrino flux at the detector.

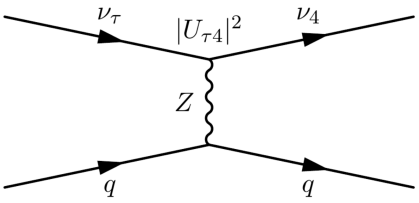

Figure 1.8: Feynman diagram of the HNL production. The heavy mass state is produced in the up-scattering of a tau neutrino.

For a non-zero $|U_{\tau 4}|^2$, the HNL can be produced through **up-scattering in the ice**. An incoming tau neutrinos scatters on an ice nucleus and transfers some of its kinetic energy to the heavy neutrino. The Feynman diagram of this process is shown in Figure 1.8. The custom NC cross-sections calculated for this purpose are explained in more detail in Section 2.2.1, but are similar to the SM tau neutrino NC cross-sections, with a reduction scaling with the mixing $|U_{\tau 4}|^2$ and energy dependent reductions, due to kinematic constraints because of the heavy neutrino mass. The scattering process produces a hadronic cascade, which will produce light in the detector.

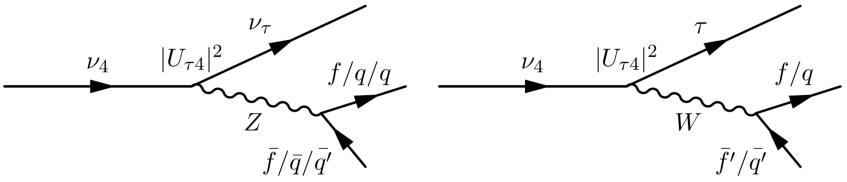

Figure 1.9: Feynman diagram of the HNL decay. The heavy mass state can decay through neutral current interaction (left) into a tau neutrino and a charged lepton or quark pair, or through charged current interaction (right) into a tau lepton and a charged lepton or quark.

After a certain distance, the HNL will **decay in the ice**, where the possible decay channels considered in this work and the underlying, explicit calculations are discussed in Section 2.2.1. The decay can be a CC or NC and both purely leptonic and leptonic+mesonic modes are possible. The Feynman diagrams of the decays can be seen in Section **??**. Only the mass range relevant for this work is presented and mixing with $\nu_{e/\mu}$ is assumed to be negligible. Depending on the decay channel, an electromagnetic or a hadronic cascade is produced, while some energy is carried away by the invisible neutrino. The decay length of the HNL is defined by its proper lifetime[2], which is given by

$$\tau_{\text{proper}} = \frac{\hbar}{\Gamma_{\text{total}}(m_4) \cdot |U_{\tau 4}|^2} \,, \tag{1.38}$$

2: A particle decay time follows an exponential distribution, with mean lifetime given by the proper lifetime. The proper lifetime is the lifetime in the rest frame of the particle.

where $\hbar$ is the reduced Planck constant, $\Gamma_{\text{total}}(m_4)$ is the total decay width of the HNL for the given mass, and $|U_{\tau 4}|^2$ is the mixing with the tau neutrino. The total decay width is the sum of the partial decay widths for all possible decay channels. The mean lab frame decay length is then given by

$$L_{\text{decay}} = \gamma v \tau_{\text{proper}} \,, \tag{1.39}$$

where γ is the Lorentz factor of the HNL, defined by the kinetic energy. This will be further discussed on Section 2.2.1. Figure 1.10 shows the mean decay lengths for an example mass of $m_4 = 0.6\,\text{GeV}$ and several mixing values.

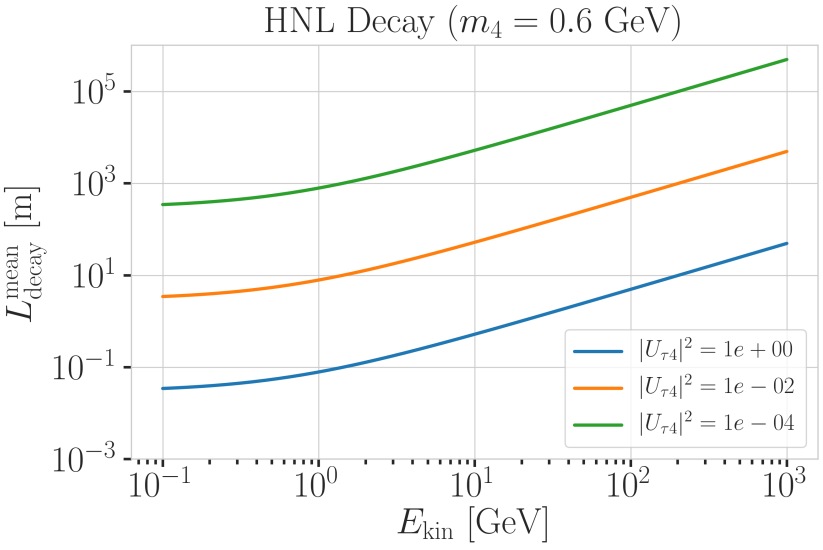

Figure 1.10: Theoretical mean decay length of the HNL for a mass of 0.6 GeV and different mixing values.

Monte Carlo Event Generation and Detector Simulation

2

Like many analyses in IceCube, this work is based on MC simulations. The initial step for all particle (non-noise) simulation is the generation of events from selected initial distributions and fluxes. Events are the primary particle and all particles produced in the interaction with the ice. The particles are then propagated through the ice, producing Cherenkov photons, which are propagated further until they reach a DOM or are absorbed in the ice. If they hit a DOM the detector response is simulated. Splitting the simulation steps has the advantage of reusing the outputs of for example the generation step to propagate the particles with different ice model, in order to estimate the systematic impacts of uncertainties of the ice properties. A similar approach can be taken for varying detector response, before starting the event selection. Through this a more efficient (reduced) use of computing resources can be achieved.

The central part of this thesis is the HNL signal simulation itself. Since this is the first search for HNLs with IceCube DeepCore, there was no prior knowledge of the number of events expected per year nor of the performance in terms of reconstruction and classification accuracy. This chapter describes the first HNL event generation developed for IceCube DeepCore. Two avenues of generation were pursued in parallel. A collection of model-independent samples is explained in Section 2.1. They were used for performance benchmarking and for cross-checks to validate the physically accurate, model-dependent event generation, which is described in Section 2.2. The event generation for SM background events is briefly described in Section 2.3, followed by the detector response simulation in Section 2.4. The detector response is identically applied to both signal and background events.

2.1 Model-Independent Heavy Neutral Lepton Event Generation

To investigate the potential of IceCube to detect HNLs by identifying the unique double cascade morphology explained in Section 1.3.4, a model-independent double cascade generator was developed, where the kinematics of each cascade can be controlled directly. Using this generator, several simulation samples were produced to investigate the performance of IceCube DeepCore to detect low-energy double cascades, dependent on their properties. All samples are produced using a collection of custom generator functions [80] that place two EM cascade vertices with variable energy and direction at configurable locations in the detector.

2.1.1 Simplistic Samples

To investigate the best-case and the worst-case double cascade event scenarios, two samples are produced in the DeepCore volume: straight up-going events ($\cos(\theta) = -1$) that are centered on a string and horizontal events ($\cos(\theta) = 0$).

The first sample is used to investigate one of the most promising scenarios to detect a double cascade, where both cascade centers are located on a DeepCore string and the directions are directly up-going. One of the DeepCore strings was randomly chosen as the x-y coordinate for this sample. As already mentioned in Section **??**, DeepCore strings have higher quantum efficiency DOMs and a denser vertical spacing, making them better to detect low-energy events that produce little light. To produce the events, the x, y position of the cascades is fixed to the center of the string while the z positions are each sampled uniformly along the axis of the string. Note that this will therefore not produce a uniform length distribution between the cascades. The positions are defined in the IceCube coordinate system that was introduced in Section **??**. The energies are sampled uniformly between 0.0 GeV and 60.0 GeV, to generously cover the region where $\nu_\mu \longrightarrow \nu_\tau$ appearance is maximized. The time of the lower cascade is set to $t_0 = 0.0\,\text{ns}$ and for the upper one to $t_1 = L/c$, assuming the HNL travels at the speed of light, c. Figure 2.1 shows the resulting energy distributions and the decay length distribution, where it can be seen how the uniform cascade energies sum into a non-uniform total energy, and the decay length distribution is also non-uniform due to the uniform z sampling of both cascades, which sets the distance between them.

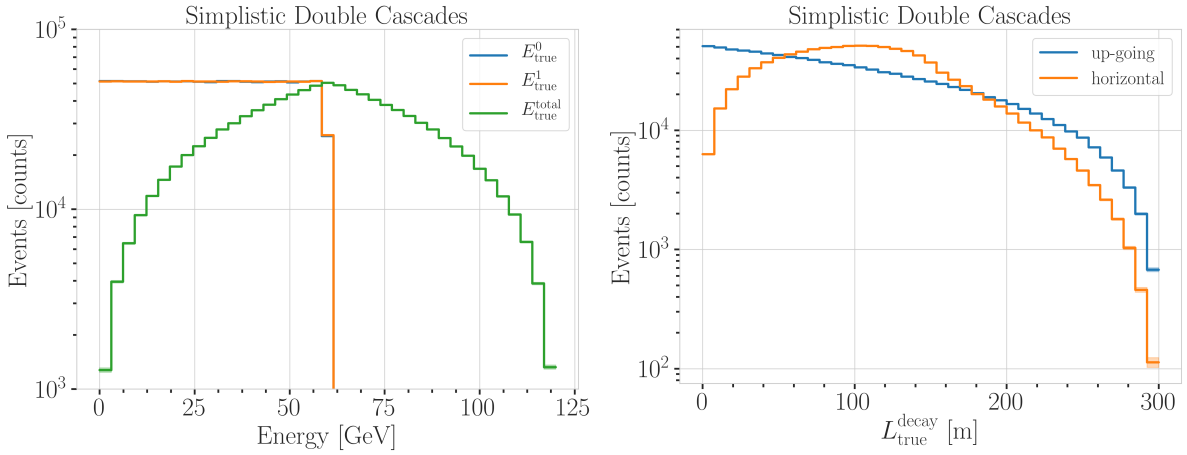

Figure 2.1: Generation level distributions of the simplistic simulation samples. Cascade and total energies (left) and decay lengths (right) of both samples are shown.

The second sample is used to investigate the reconstruction performance for horizontal events, where the spacing between DOMs is much larger. The cascades are placed uniformly on a circle with radius of $r = 150\,\text{m}$ centered in DeepCore at the depth of $z = -330\,\text{m}$. The direction is always horizontal and azimuth is defined by the connecting vector of both cascade positions. The energies are again sampled uniformly between 0.0 GeV and 60.0 GeV. The specific sampling distributions/values for the cascades are listed in Table 2.1, for both samples and for completeness, all distributions are shown in Figure **??**.

2.1.2 Realistic Sample

To thoroughly investigate the potential of IceCube DeepCore to detect double cascade events, a more realistic simulation sample is produced that aims to be as close as possible to the expected signal simulation explained in

Sample	Variable	Distribution	Range/Value
Up-going			
	energy	uniform	0.0 GeV to 60.0 GeV
	zenith	fixed	180.0°
	azimuth	fixed	0.0°
	x, y position	fixed	(41.6, 35.49) m
	z position	uniform	−480.0 m to −180.0 m
Horizontal			
	energy	uniform	0.0 GeV to 60.0 GeV
	zenith	fixed	90.0°
	azimuth	uniform	0.0° to 360.0°
	x, y position	uniform (circle)	c=(46.29, -34.88) m, r=150.0 m
	z position	fixed	−330.0 m

Table 2.1: Generation level sampling distributions and ranges/values of up-going and horizontal model-independent simulation.

Section 2.2, while still allowing additional freedom to control the double cascade kinematics. This sample is particularly useful for validating the model-dependent HNL simulation described in Section 2.2.

For this purpose the total energy is sampled from an E^{-2} power law, mimicking the energy spectrum of the primary neutrinos as stated in Section 2.3.1. The total energy is divided into two parts, by assigning a fraction between 0 % and 100 % to one cascade and the remaining part to the other cascade. This is a generic approximation of the realistic process described in Section 2.2, and chosen such that the whole sample covers various cases of energy distributions between the two cascades. The decay length is sampled from an exponential distribution, as expected for a decaying heavy mass state. The resulting energy distributions and the decay length distribution are shown in Figure 2.2, where it can be seen that the individual cascade energies can be very small, due to splitting the total energy, and the decay lengths spans across several orders of magnitude.

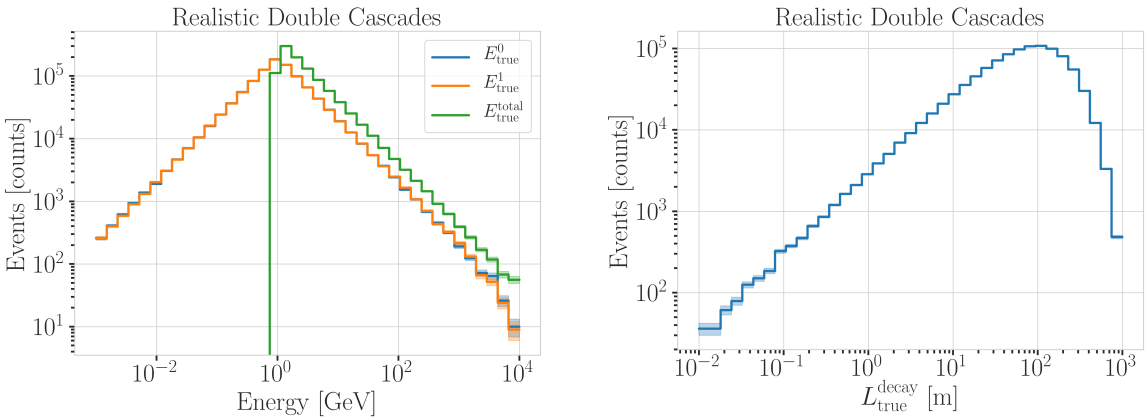

Figure 2.2: Generation level distributions of the realistic sample. Shown are the individual cascade energies and total energy (left) and decay lengths (right). It can be seen how the cascade energies can get very small, and the decay length follows a more realistic distribution spanning across several orders of magnitude.

To efficiently generate events in a way that produces distributions similar to what would be observed with DeepCore, one of the cascade positions is sampled inside the DeepCore volume by choosing its coordinates uniformly on a cylinder that is centered in DeepCore. This is similar to a trigger condition of one cascade always being inside the DeepCore fiducial volume. Choosing the direction of the event by sampling zenith and azimuth uniformly between 70° and 180° and 0° and 360°, respectively, the position of the other cascade

can be inferred for a given decay length, assuming a travel speed of c, and choosing whether the cascade position that was sampled is the first cascade or the second with a 50 % chance. The zenith angle is chosen between straight up-going (zenith of 180°) and slightly down-going from above the horizon (70°) to mimic an event selection that reduces atmospheric muons by rejecting events coming from above the horizon, but still incorporates some down-going events. All distributions are shown in Figure **??**, and the sampling distributions/values are listed in Table 2.2.

Table 2.2: Generation level sampling distributions and ranges/values of the realistic model-independent simulation.

Variable	Distribution	Range/Value
energy (total)	power law E^{-2}	1 GeV to 1000 GeV
decay length	exponential $e^{-0.01L}$	0 m to 1000 m
zenith	uniform	70° to 180°
azimuth	uniform	0° to 360°
x, y (one cascade)	uniform (circle)	c=(46.29, -34.88) m, r=150 m
z (one cascade)	uniform	−480.0 m to −180.0 m

2.2 Model-Dependent Heavy Neutral Lepton Event Generation

To estimate the HNL event expectation in IceCube DeepCore, depending on the specific model parameters, a generator was developed that is based on the HNL theory introduced in Section 1.3. For this work, only the interaction with the τ-sector was taken into account ($|U^2_{\alpha 4}| = 0, \alpha = e, \mu$), which reduces the physics parameters of interest and relevant for the generation to the fourth heavy lepton mass, m_4, and the mixing, $|U^2_{\tau 4}|$.

Due to the very low interaction rate of neutrinos, which are the source of HNL production, the event generation is performed in a way that forces every event to interact in a chosen sampling volume. The weight of each event is then calculated as the inverse of the simulated neutrino fluence

$$w_{\text{gen}} = \frac{1}{F_{\text{sim}}} \frac{1}{N_{\text{sim}}} , \tag{2.1}$$

where F_{sim} is the number of neutrino events per energy, time, area, and solid angle, and N_{sim} is the number of simulated events. If this weight is multiplied by the livetime and the theoretically expected neutrino flux for a given physical model, it results in the number of expected events in the detector for this particular MC event.

The generator uses a customized *LeptonInjector (LI)* version to create the events and *LeptonWeighter (LW)* to weight them [81]. The modified LI and the essential components needed for the HNL simulation are described in the next sections, followed by the description of the weighting scheme and the sampling distributions chosen for the generation.

[81]: Abbasi et al. (2021), "LeptonInjector and LeptonWeighter: A neutrino event generator and weighter for neutrino observatories"

2.2.1 Custom LeptonInjector

In its standard version, the LI generator produces neutrino interactions by injecting a lepton and a hadronic cascade at the interaction vertex of the neutrino, where the lepton is the charged (neutral) particle produced in a CC (NC) interaction and the cascade is the hadronic cascade from the

nucleus that is breaking apart. The hadronic cascade is stored as a specific object of type *Hadrons*, which triggers the correct simulation of the shower development in the following simulation steps. Below 30 GeV the individual hadrons are simulated using GEANT4 [82] while for higher energies an analytical approximation from [83] is used. The main differences to an EM cascade is that part of the energy will not be observed, because it goes into neutral particles, and that the spatial development of the shower is different as discussed in Section **??**. Both objects are injected with the same (x, y, z, t) coordinates and the kinematics are sampled from the differential and total cross-sections that are one of the inputs to LI.

[82]: Agostinelli et al. (2003), "Geant4—a simulation toolkit"

[83]: Rädel et al. (2012), "Calculation of the Cherenkov light yield from low energetic secondary particles accompanying high-energy muons in ice and water with Geant4 simulations"

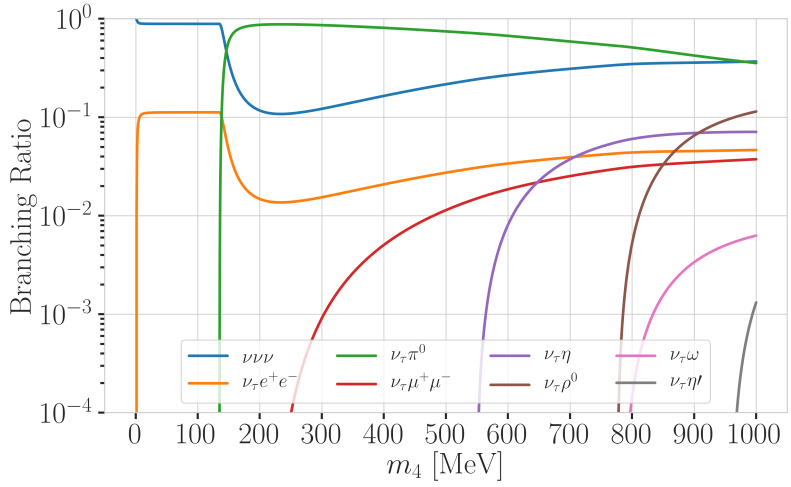

Figure 2.3: Branching ratios of the HNL within the mass range considered in this work, only considering $|U_{\tau 4}^2| \neq 0$, calculated based on the results from [72].

In the modified version, the SM lepton at the interaction vertex is replaced by the new HNL particle, where the interaction cross-sections are replaced by custom, mass dependent HNL cross-sections. The HNL is forced to decay after a chosen distance[1] to produce secondary SM particles, where the decay mode is chosen with a probability given by the mass dependent branching ratios from the kinematically accessible decay modes shown in Figure 2.3. The cross-section and decay width calculations were implemented for this purpose and will be explained in more detail in the following. Another addition to LI is that the decay products of the HNL are also stored. These HNL daughter particles form the second cascade, not as a single hadronic cascade object, but as the explicit particles forming the shower. They are injected with the correctly displaced position and delayed time from the interaction vertex, given the HNL decay length. The kinematics of the two-body decays are computed analytically, while the 3-body decay kinematics are calculated with MADGRAPH [84], which will also be explained further below. Independent of the number of particles in the final state of the HNL decay, the kinematics are calculated/simulated at rest and then boosted along the HNL momentum.

1: The explicit sampling distributions and ranges can be found in Section 2.2.2.

[84]: Alwall et al. (2014), "The automated computation of tree-level and next-to-leading order differential cross sections, and their matching to parton shower simulations"

Muons produced in those decays are propagated using PROPOSAL [85], also simulating their Cherenkov light output. The shower development of gamma rays, electrons, and positrons below 100 MeV is also simulated using Geant4 and for higher energies the analytical approximation is used again [83].

[85]: Koehne et al. (2013), "PROPOSAL: A tool for propagation of charged leptons"

The injection is done using the LI *volume mode*, for the uniform injection of the primary particle on a cylindrical volume, adding 50 % of the events with ν_τ and the other half with $\bar{\nu}_\tau$ as primary particle types. The generator takes

the custom double-differential/total cross-section splines described below and the parameters defining the sampling distributions as inputs.

Cross-Sections

The cross-sections are calculated using the NuXSSplMkr [86] software, which is a tool to calculate neutrino cross-sections from *parton distribution functions (PDFs)* and then fit to an N-dimensional tensor-product B-spline surface [87] to produce the splines that can be read and used with LI/LW. The tool was modified to produce the custom HNL cross-sections, where the main modification to calculate the cross-sections for the ν_τ-NC interaction into the new heavy mass state, is the addition of a kinematic condition to ensure that there is sufficient energy to produce the heavy mass state. It is the same condition fulfilled for the CC case, where the outgoing charged lepton mass is non-zero. Following [88] (equation 7), the condition

$$(1 + x\delta_N)h^2 - (x + \delta_4)h + x\delta_4 \leq 0 \tag{2.2}$$

is implemented for the NC case in the NuXSSplMkr code. Here

$$\delta_4 = \frac{m_4^2}{s - M^2}\,, \tag{2.3}$$

$$\delta_N = \frac{M^2}{s - M^2}\,, \text{and} \tag{2.4}$$

$$h \overset{def}{=} xy + \delta_4\,, \tag{2.5}$$

with x and y being the Bjorken variables, m_4 and M the mass of the heavy state and the target nucleon, respectively, and s the center of mass energy squared. The custom version was made part of the open source NuXSSplMkr software and can thus be found in [86]. The result of this kinematic condition is that events cannot be produced for energy, x, y combinations that do not have sufficient energy to produce the outgoing, massive lepton. This results in a reduction of the cross-section towards lower energies, which scales with the assumed mass of the HNL. This effect can be seen in Figure 2.4.

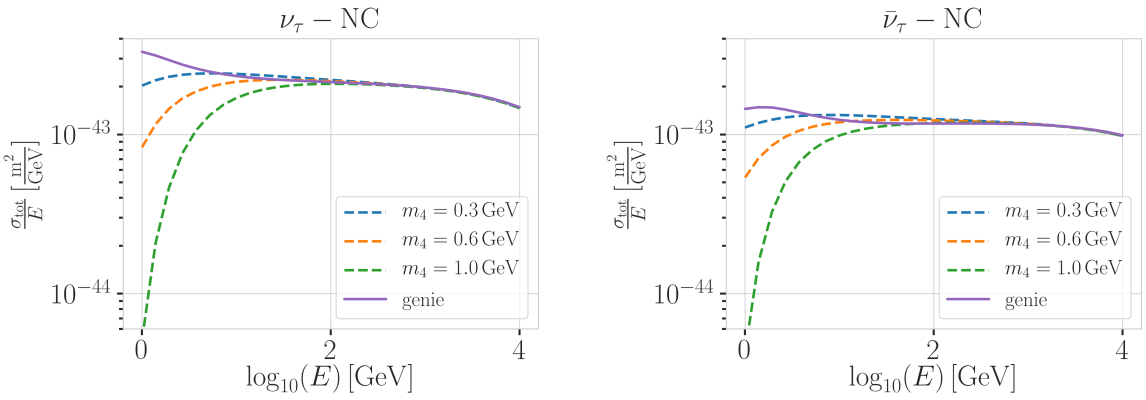

Figure 2.4: Custom HNL total cross-sections for the three target masses compared to the total ($\nu_\tau/\bar{\nu}_\tau$ NC) cross-sections used for SM neutrino simulation production with GENIE.

The GRV98LO PDFs were added to the cross-section spline maker and used to create the HNL cross-sections for consistency with the neutrino

[87]: Whitehorn et al. (2013), "Penalized splines for smooth representation of high-dimensional Monte Carlo datasets"

[88]: Levy (2009), "Cross-section and polarization of neutrino-produced tau's made simple"

simulation explained in Section 2.3.1. The double-differential ($d^2\sigma/dxdy$) and total (σ) cross-sections were produced for the chosen target HNL masses and then splined in energy, x, and y for $d^2\sigma/dxdy$ and σ in the energy. Figure 2.4 shows the total cross-sections that were produced compared to the cross-section used for the production of the SM $\nu_\tau/\bar{\nu}_\tau$ NC background simulation. They agree above $\sim$ 200 GeV, where the modification should not have any effect on the cross-sections. This is the desired result of using the identical input PDFs, and confirms that the unmodified cross-sections produced with NuXSSplMkr agree with the GENIE cross-sections.

Decay Channels

The accessible decay channels are dependent on the mass of the HNL and the allowed mixing. For this analysis, where only $|U_{\tau 4}|^2 \neq 0$, the decay channels considered are listed in Table 2.3 and the corresponding branching ratios are shown in Figure 2.3. The individual branching ratio for a specific mass is calculated as $\mathrm{BR}_i(m_4) = \Gamma_i(m_4)/\Gamma_{\mathrm{total}}(m_4)$, where $\Gamma_{\mathrm{total}}(m_4) = \sum \Gamma_i(m_4)$. They can be seen in Figure 2.5, where the individual decay widths Γ_i are shown, which are computed using an implementation of the state-of-the-art calculations from [72]. The formulae for these calculations are explicitly listed in the following.

[72]: Coloma et al. (2021), "GeV-scale neutrinos: interactions with mesons and DUNE sensitivity"

Channel	Opens
$\nu_4 \to \nu_\tau \nu_\alpha \bar{\nu_\alpha}$	0 MeV
$\nu_4 \to \nu_\tau e^+ e^-$	1 MeV
$\nu_4 \to \nu_\tau \pi^0$	135 MeV
$\nu_4 \to \nu_\tau \mu^+ \mu^-$	211 MeV
$\nu_4 \to \nu_\tau \eta$	548 MeV
$\nu_4 \to \nu_\tau \rho^0$	770 MeV
$\nu_4 \to \nu_\tau \omega$	783 MeV
$\nu_4 \to \nu_\tau \eta'$	958 MeV

Table 2.3: Possible decay channels of the HNL, considering only $|U_{\tau 4}|^2 \neq 0$, and the mass at which each channel opens.

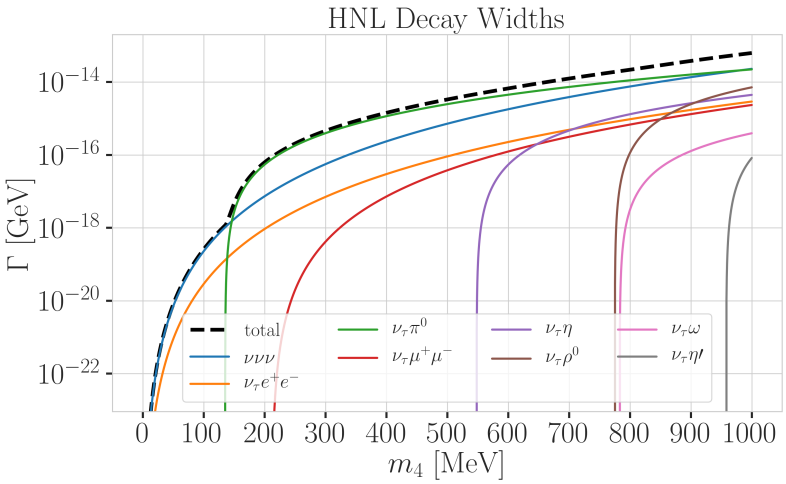

Figure 2.5: Decay widths of the HNL within the mass range considered, calculated based on the results from [72]. Given the existing constraints on $|U_{e4}|^2$ and $|U_{\mu 4}|^2$, we consider that the corresponding decay modes are negligible.

2-Body Decay Widths The decay to a neutral pseudoscalar meson is

$$\Gamma_{\nu_4 \to \nu_\tau P} = |U_{\tau 4}|^2 \frac{G_F^2 m_4^3}{32\pi} f_P^2 (1 - x_p^2)^2 \,, \tag{2.6}$$

with $x_P = m_P/m_4$ and the *effective decay constants* f_P given by

$$f_{\pi^0} = +0.1300\,\mathrm{GeV}\,, \tag{2.7}$$
$$f_\eta = +0.0816\,\mathrm{GeV}\,, \text{and} \tag{2.8}$$
$$f_{\eta'} = -0.0946\,\mathrm{GeV}\,, \tag{2.9}$$

while the decay to a neutral vector meson is given by

$$\Gamma_{\nu_4 \to \nu_\tau V} = |U_{\tau 4}|^2 \frac{G_F^2 m_4^3}{32\pi} \left(\frac{f_V}{m_V} \right)^2 g_V^2 (1 + 2x_V^2)(1 - x_V^2)^2 \,, \tag{2.10}$$

with $x_V = m_V / m_4$,

$$f_{\rho^0} = 0.171\,\text{GeV}^2 \,, \tag{2.11}$$

$$f_\omega = 0.155\,\text{GeV}^2 \,, \tag{2.12}$$

and

$$g_{\rho^0} = 1 - 2\sin^2\theta_w \,, \tag{2.13}$$

$$g_\omega = \frac{-2\sin^2\theta_w}{3} \,, \tag{2.14}$$

and $\sin^2\theta_w = 0.2229$ [89], where θ_w is the Weinberg angle.

[89]: Tiesinga et al. (2021), "CODATA recommended values of the fundamental physical constants: 2018"

3-Body Decay Widths The (invisible) decay to three neutrinos, one of flavor τ and two of any flavor α, is

$$\Gamma_{\nu_4 \to \nu_\tau \nu_\alpha \bar{\nu_\alpha}} = |U_{\tau 4}|^2 \frac{G_F^2 m_4^5}{192\pi^3} \,, \tag{2.15}$$

while the decay to two charged leptons (using $x_\alpha = (m_\alpha / m_4)^2$) of the same flavor reads

$$\Gamma_{\nu_4 \to \nu_\tau l_\alpha^+ l_\alpha^-} = |U_{\tau 4}|^2 \frac{G_F^2 m_4^5}{192\pi^3} \left[C_1 f_1(x_\alpha) + C_2 f_2(x_\alpha) \right] \,, \tag{2.16}$$

with the constants defined as

$$C_1 = \frac{1}{4}(1 - 4\sin^2\theta_w + 8\sin^4\theta_w) \,, \tag{2.17}$$

$$C_2 = \frac{1}{2}(-\sin^2\theta_w + 2\sin^4\theta_w) \,, \tag{2.18}$$

the functions as

$$f_1(x_\alpha) = (1 - 14x_\alpha - 2x_\alpha^2 - 12x_\alpha^3)\sqrt{1 - 4x_\alpha} + 12x_\alpha^2(x_\alpha^2 - 1)L(x_\alpha) \,, \tag{2.19}$$

$$f_2(x_\alpha) = 4[x_\alpha(2 + 10x_\alpha - 12x_\alpha^2)\sqrt{1 - 4x_\alpha} + 6x_\alpha^2(1 - 2x_\alpha + 2x_\alpha^2)L(x_\alpha)] \,, \tag{2.20}$$

and

$$L(x) = \ln\left(\frac{1 - 3x_\alpha - (1 - x_\alpha)\sqrt{1 - 4x_\alpha}}{x_\alpha(1 + \sqrt{1 - 4x_\alpha})} \right) . \tag{2.21}$$

Analytical 2-Body Decay Kinematics

[15]: Workman et al. (2022), "Review of Particle Physics"

Following the review of [15], the 4-vector defining the kinematics of a particle is $p = (E, \vec{p})$, with its energy, E, and 3-momentum, $\vec{p}$. Squaring it gives the mass, $p^2 = E^2 - \vec{p}^2 = m^2$, while the velocity is $\vec{\beta} = \vec{p}/E$. If the HNL with mass m_4 decays into two particles with masses m_1 and m_2, their 3-momenta

in the rest frame of the HNL are given by

$$|\vec{p}_1| = |\vec{p}_2| = \frac{\lambda^{1/2}(m_4^2, m_1^2, m_2^2)}{2m_4} , \tag{2.22}$$

where $\lambda(x, y, z) = x^2 + y^2 + z^2 - 2xy - 2xz - 2yz$. The energy of the particles is then given by

$$E_1 = \frac{m_4^2 + m_1^2 - m_2^2}{2m_4} , \tag{2.23}$$

and equivalently for E_2. The 4-vectors of the particle are then boosted to the lab frame, where the HNL is moving with velocity $\vec{\beta}$.

Simulated 3-Body Decay Kinematics

The 3-body decay kinematics cannot be computed analytically, instead, we employ MadGraph4 (v3.4.0) [90] for this purpose. MadGraph is a tool to simulate particle collisions and decay processes, and is widely used in the high-energy physics community. The 3-body decay kinematics are calculated in the rest frame of the HNL, using decay diagrams calculated with FeynRules 2.0 [91] and the Lagrangians derived in [72] as input. The *Universal FeynRules Output (UFO)* from effective_HeavyN_Majorana_v103 were used for our calculation. For each mass and corresponding decay channels, we produce 1×10^6 decay kinematic variations in the rest frame and store those in a text file. During event generation, we uniformly select an event from that list, to simulate the decay kinematics of a 3-body decay.

[91]: Alloul et al. (2014), "FeynRules 2.0 - A complete toolbox for tree-level phenomenology"

[72]: Coloma et al. (2021), "GeV-scale neutrinos: interactions with mesons and DUNE sensitivity"

2.2.2 Sampling Distributions

Variable	Distribution	Range/Value
energy	E^{-2}	[2 GeV, 1×10^4 GeV]
zenith	uniform (in $\cos(\theta)$)	[80°, 180°]
azimuth	uniform	[0°, 360°]
vertex x, y	uniform (on circle)	r=600 m
vertex z	uniform	−600 m to 0 m
m_4	fixed	[0.3, 0.6, 1.0] GeV
L_{decay}	L^{-1}	[0.0004, 1000] m

Table 2.4: Generation level sampling distributions and ranges/values of the model-dependent simulation samples.

In principle, the generation level sampling distributions should be chosen such that at the final level of the event selection chain the phase space relevant for the analysis is covered with sufficient statistics to make a reasonable estimate of the event expectation. Initial distributions insufficiently covering the phase space lead to an underestimation of the expected rates, because some of the events that would pass the selection are not produced. This limits the expected analysis potential. Three discrete simulation samples were produced with HNL masses of 0.3 GeV, 0.6 GeV, and 1.0 GeV. The remaining sampling distributions are identical for all samples and are listed in Table 2.4. The target number of events for each sample was 2.5×10^9 at generation to result in sufficient MC statistics at final level. Figure 2.6 shows the true cascade energies, which result from the custom interaction cross-sections and the decays discussed above. Note here that these are the full true energies

going into the cascades. For the first cascade some energy goes into invisible particles produced in the hadronic shower development and for the HNL decay, there always is at least one invisible neutrino. Additional sampling distributions can be found in Figure **??**.

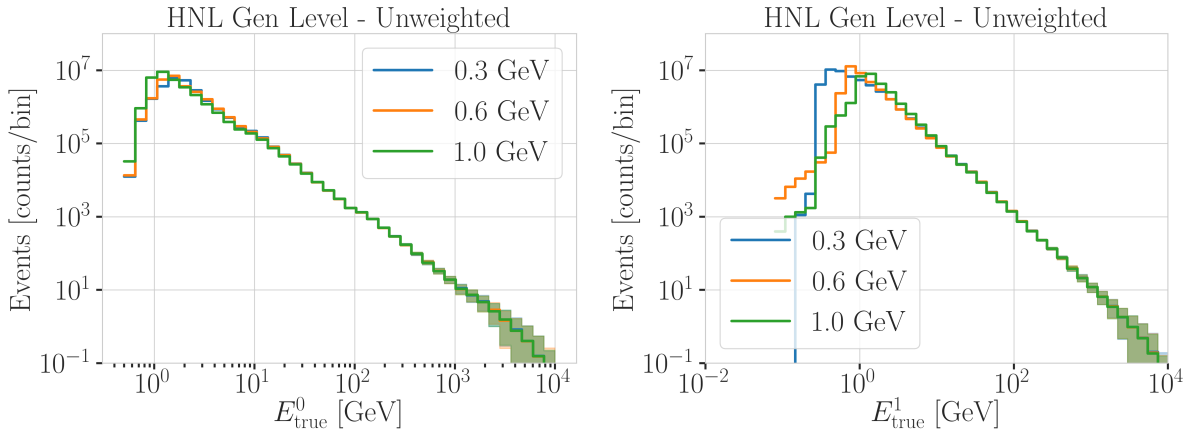

Figure 2.6: Generation level distributions of the model-dependent simulation. Shown are the true energies of both cascades including the energy that goes into invisible particles.

2.2.3 Weighting Scheme

Since the lab frame decay lengths/lifetimes of the events were sampled from an inverse distribution instead of an exponential, as it would be expected from a particle decay, we have to re-weight accordingly to achieve the correct decay length distribution. The re-weighting factor is calculated as the ratio of the *probability density functions (PDFs)* of the desired exponential distribution and the inverse distribution that was sampled from as $\frac{\text{PDF}_{\text{exp}}}{\text{PDF}_{\text{inv}}}$.

The inverse distribution in the rest frame of the HNL is given by

$$\text{PDF}_{\text{inv}} = \frac{1}{\tau \cdot (\ln(\tau_{\text{max}}) - \ln(\tau_{\text{min}}))} , \tag{2.24}$$

where τ is the rest frame lifetime and $\tau_{\text{min/max}}$ are the minimum and maximum values of the lifetime sampling range. Since the generation range is chosen in the lab frame, the rest frame lifetime range $[\tau_{\text{min}}, \tau_{\text{max}}]$ is defined by the lab frame decay length range $[s_{\text{min}}, s_{\text{max}}]$ as

$$\tau_{\text{min/max}} = \frac{s_{\text{min/max}}}{v \cdot \gamma}. \tag{2.25}$$

Here, the gamma factor is calculated for each event as

$$\gamma = \frac{\sqrt{E^2_{\text{kin}} + m^2_4}}{m_4} , \tag{2.26}$$

with the HNL mass, m_4, and its kinetic energy, E_{kin}, while v is the speed of the HNL which is calculated as

$$v = c \cdot \sqrt{1 - \frac{1}{\gamma^2}} , \tag{2.27}$$

where c is the speed of light.

The desired exponential distribution of the rest frame lifetime is given by

$$\mathrm{PDF}_{\mathrm{exp}} = \frac{1}{\tau_{\mathrm{proper}}} \cdot e^{\frac{-\tau}{\tau_{\mathrm{proper}}}} , \tag{2.28}$$

where τ_{proper} is the proper lifetime of each HNL event that is calculated using the total decay width, Γ_{total}, and the chosen mixing strength $|U_{\tau 4}|^2$ as

$$\tau_{\mathrm{proper}} = \frac{\hbar}{\Gamma_{\mathrm{total}}(m_4) \cdot |U_{\tau 4}|^2} , \tag{2.29}$$

where $\hbar$ is the reduced Planck constant.

This re-weighting factor is then calculated as

$$w_{\mathrm{lifetime}} = \frac{\mathrm{PDF}_{\mathrm{exp}}}{\mathrm{PDF}_{\mathrm{inv}}} = \frac{\Gamma_{\mathrm{total}}(m_4) \cdot |U_{\tau 4}|^2}{\hbar} \cdot \tau \cdot (\ln(\tau_{\mathrm{max}}) - \ln(\tau_{\mathrm{min}})) \cdot e^{\frac{-\tau}{\tau_{\mathrm{proper}}}} . \tag{2.30}$$

Adding another factor of $|U_{\tau 4}|^2$ to account for the mixing at the interaction vertex the total re-weighting factor becomes

$$w_{\mathrm{total}} = |U_{\tau 4}|^2 \cdot w_{\mathrm{lifetime}} . \tag{2.31}$$

If this additional weighting factor is multiplied to the generation weight introduced in Section 2.2 (in m^2), the livetime (in s), and the oscillated primary neutrino flux (in $\mathrm{m}^{-2}\mathrm{s}^{-1}$) it results in the number of expected events in the detector for this particular MC event for a specific mixing (and mass). The only required input is therefore the mixing strength $|U_{\tau 4}|^2$, since the mass is fixed for each sample. This re-weighting scheme allows to continuously vary the mixing strength and to estimate the expected event rate for, which will be crucial for the analysis performed in Chapter 3.

2.3 Standard Model Event Generation

2.3.1 Neutrinos

The simulation volume is a cylinder centered in DeepCore with radius and height chosen such that all events possibly producing a signal are contained. The different sizes, chosen depending on energy and neutrino flavor, are shown in Table 2.5. The directions of the neutrinos are sampled isotropically and the energies are sampled from an E^{-2} power law. The number of simulated events is chosen such that the livetime is more than 70 years for each flavor. Neutrinos and antineutrinos are simulated with ratios of 70% and 30%, respectively, which is roughly the ratio expected from the atmospheric neutrino flux [74].

To simulate the neutrino interaction with the ice, the GENIE event generator [92] (version 2.12.8) is used, resulting in the secondary particles and the kinematic and cross-section parameters. As input, the outdated GRV98LO [93] PDFs were used, because they were the only option that could incorporate extrapolations to lower Q^2 [94]. The propagation of the secondary particles and of the shower development is performed identical to the description in Section 2.2.1 and produces the energy losses and event morphologies introduced in Section **??**.

[74]: Honda et al. (2015), "Atmospheric neutrino flux calculation using the NRLMSISE-00 atmospheric model"

[92]: Andreopoulos et al. (2015), "The GENIE Neutrino Monte Carlo Generator: Physics and User Manual"

[93]: Glück et al. (1998), "Dynamical parton distributions revisited"

[94]: Bodek et al. (2003), "Higher twist, xi(omega) scaling, and effective LO PDFs for lepton scattering in the few GeV region"

Table 2.5: Cylinder volumes used for GENIE neutrino simulation generation. Cylinder is always centered in DeepCore at $(x, y, z) = (46.29, -34.88, -330.00)$ m.

Flavor	Energy [GeV]	Radius [m]	Length [m]	Events/File	Files
$\nu_e + \bar{\nu_e}$	1-4	250	500	450000	650
	4-12			100000	
	12-100	350	600		
	100-10000	550	1000	57500	
$\nu_\mu + \bar{\nu_\mu}$	1-5	250	500	408000	1550
	5-80	400	900	440000	
	80-1000	450	1500	57500	
	1000-10000	550		6700	
$\nu_\tau + \bar{\nu_\tau}$	1-4	250	500	1500000	350
	4-10			300000	
	10-50	350	600	375000	
	50-1000	450	800	200000	
	1000-10000	550	1500	26000	

2.3.2 Muons

Atmospheric muons are generated on a cylinder surface enclosing the full IceCube detector array. The cylinder has a height of 1600 m and a radius of 800 m. The energy is sampled from an E^{-3} power law while the other sampling distributions (position, direction) are found from parameterizations based on [95]. This work uses full Corsika [96] simulations of muons to tailor the parameterizations, starting from *cosmic ray (CR)* interactions with atmospheric nuclei using the CR flux model from [97] and producing the muons applying the hadronic interaction model SIBYLL 2.1 [98]. After the generation, they are propagated through the ice with PROPOSAL producing photons, treating them exactly like the muons produced in the HNL and neutrino event generation.

[95]: Becherini et al. (2006), "A parameterisation of single and multiple muons in the deep water or ice"

[96]: Heck et al. (1998), "CORSIKA: A Monte Carlo code to simulate extensive air showers"

[97]: Gaisser (2012), "Spectrum of cosmic-ray nucleons, kaon production, and the atmospheric muon charge ratio"

[98]: Engel et al. (2017), "The hadronic interaction model Sibyll – past, present and future"

Since the offline processing and selection steps described in Section **??** and Section **??** reduce the muon contamination to an almost negligible level, the statistical uncertainty on the number of expected muon events at the final selection level is large and therefore two separate samples of muon simulation are produced. **A first sample** is used to tune the lower level selection (up to Level 4), therefore including all events resulting from the above described generation. **A second sample** is then produced to estimate the muon contamination at higher levels (above Level 5). It only consists of muon events that pass through a smaller cylinder centered in DeepCore (height of 400 m and radius of 180 m), and additionally rejects events based on a KDE estimated muon density at Level 5 (in energy and zenith). This increased the simulation efficiency at Level 5 significantly, making it feasable to use this sample to estimate the muon contamination at higher levels.

2.4 Detector Simulation

The detector simulation is performed after the event generation, where the initial particles and the resulting photons and secondary particles from their propagation were produced. This part of the simulation chain is applied to all muon and neutrino simulation as well as the HNL signal simulation. The detector simulation can be split into two parts: the propagation of the

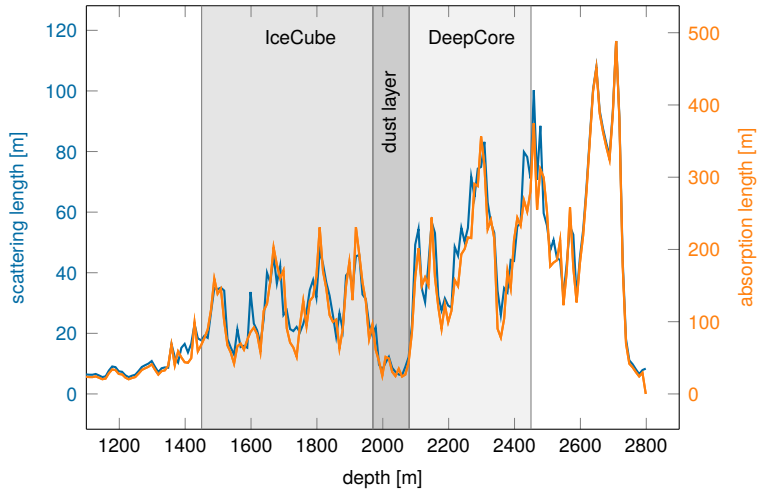

Figure 2.7: Scattering and absorption lengths as a function of depth in the SPICE model used for simulation. Modified from [13].

photons and the simulation of the detector response (including internal noise).

2.4.1 Photon Propagation

Any photon that was produced in the event generation is individually traced through the ice, simulating scattering and absorption processes. The propagation is done using CLSIM [99] which is an implementation of the *Photon Propagation Code (PPC)* [100] in OpenCL. It is optimized to be run efficiently on GPUs. The ice is modeled as a set of 10 m thick, almost horizontal layers with specific absorption and scattering lengths. The *South Pole ice (SPICE)* model [101] accounts for the layers being tilted by a small amount, due to the uneven surface of the bedrock below the glacier, and the absorption and scattering lengths having a non-uniformity with respect to the azimuth direction. Figure 2.7 shows the values of this model for the different depths, indicating the location of IceCube, DeepCore, and the dust layer.

[100]: Chirkin et al. (2019), "Photon Propagation using GPUs by the IceCube Neutrino Observatory"

[101]: Aartsen et al. (2013), "Measurement of South Pole ice transparency with the IceCube LED calibration system"

In an initial step, each photon's absorption length is sampled from an exponential distribution with the expectation value at the current layer's absorption length. The following propagation steps are performed in parallel for all photons. In each of those steps, corresponding to a single scattering event, the photon travels a length that is sampled from an exponential distribution with the expectation value at the scattering length of the current layer and the scattering angle chosen based on a combination of a simplified Mie scattering distribution [102] and a Henyey-Greenstein distribution [103] [104]. The parameters defining the shape of these distributions were calibrated using data from *in-situ* LED calibration runs. These steps are continuously repeated until each photon reaches a DOM or is absorbed[2]. After all photons have been propagated in that manner, the final step is to store the photons that reached a DOM for further processing.

[102]: Mie (1908), "Beiträge zur Optik trüber Medien, speziell kolloidaler Metallösungen"

[103]: Henyey et al. (1941), "Diffuse radiation in the Galaxy."

[104]: Abbasi et al. (2022), "In-situ estimation of ice crystal properties at the South Pole using LED calibration data from the IceCube Neutrino Observatory"

2: A photon is absorbed, when it traveled its full absorption length, sampled in the initial step of the photon propagation.

2.4.2 Detector Responses

The second part of simulating the IceCube detector is the DOM response. For a photon that reaches a DOM, the probability to produce a signal depends

on the total efficiency and the angular acceptance of the specific DOM. The total efficiency includes effects of the DOM glass, PMT quantum and photo-electron collection efficiencies, and it is wavelength dependent. Additionally, there is another angle dependent effect called *hole ice* [105]. This effect is due to varied ice properties resulting from the re-freezing process of the water column inside the borehole after deployment of the string. Accepted photons are converted into a so-called *Monte Carlo photo-electron (MCPE)*. The amount of charge measured for each MCPE is determined by sampling from the so-called *single photo-electron (SPE)* distribution, which was tuned to match the observed distribution in each DOM in an *in-situ* calibration study [106]. Figure 2.8 shows the spread of the distribution measured over all DOMs compared to lab measurements of a specific PMT type. Based on the sampled charges and times of MCPEs, the voltage waveforms for the (two) different readout channels are simulated and passed on to the trigger simulation starting with *WaveDeform* (see Section **??**).

[105]: Fiedlschuster (2019), "The Effect of Hole Ice on the Propagation and Detection of Light in IceCube"

[106]: Aartsen et al. (2020), "In-situ calibration of the single-photoelectron charge response of the IceCube photomultiplier tubes"

Parameter	Value
Therm. rate λ_{th}	180 Hz
Decay rate λ_{dec}	80 Hz
Decay hits η	8.5
Decay μ	4.3 $\log_{10}$(ns)
Decay σ	1.8 $\log_{10}$(ns)

Table 2.6: Typical parameter values used in the vuvuzela noise simulation. Averaged over all DOMs.

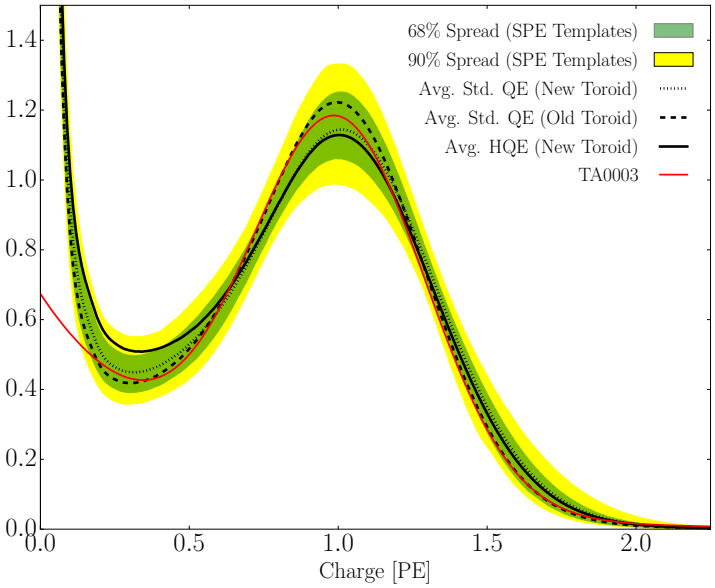

Figure 2.8: Single photo-electron charge distribution shown for a lab measurement in red (TA0003), various hardware configurations in black dashed, dotted, and solid lines, and the 68 % and 90 % spread of the measured charged templates for all DOMs. All curves are normalized to the same area. The figure is taken from [106].

Besides the Cherenkov photons, IceCube also observes photons that are produced in radioactive decays inside the DOMs, both in the glass housing sphere and the PMT glass itself. To simulate this internal noise, the *Vuvuzela* module [107, 108] is used to create additional MCPEs that are fed into the same simulation chain described above. The noise hits are simulated by drawing the times from a constant rate Poisson process and the number of photons from a Poisson distribution. Then the time differences between the individual photons per hit is found, based on a Log-Normal distribution. The simulation is defined by 5 parameters that are calibrated for each DOM individually. Table 2.6 shows the average values for these parameters.

[107]: Larson (2013), "Simulation and Identification of Non-Poissonian Noise Triggers in the IceCube Neutrino Detector"

[108]: Larson (2018), "A Search for Tau Neutrino Appearance with IceCube-DeepCore"

Search for Tau Neutrino Induced Heavy Neutral Lepton Events

3

This chapter describes the search for HNL events using 10 years of IceCube DeepCore data. The expected number of HNL events in the data sample depends on the mass of the additional heavy state, m_4, and the mixing element $|U^2_{\alpha 4}|$, with $\alpha = e, \mu, \tau$, between the SM flavors and the new mass state. As discussed in Section 1.3, this work focuses on the mixing to the tau sector, $|U^2_{\tau 4}|$, which has the weakest constraints to date. Since the mass itself influences the production and decay kinematics of the event and the accessible decay modes, individual mass samples were produced as described in Section 2.2. The mass influences the decay length and energy distributions, while the mixing both changes the overall expected rate of the HNL events and the shape in energy and length. We perform three independent searches for each mass sample, where the mixing is measured in each of the fits.

work in the parts about MC re-weighting (forward folding) etc. from below (RED)

3.1 Final Level Sample

The final level simulation sample of this analysis consists of the neutrino and muon MC introduced in Section 2.3 and one of the three HNL samples explained in Section 2.2, while the data are the events measured in 10 years of IceCube DeepCore data taking. All simulation and the data are processed through the full event selection chain described in Section **??** and Section **??** leading to the final level sample. As described in Section **??**, event triggers consisting purely of random coincidences induced by noise in the DOMs have been reduced to a negligible rate, and will not be discussed further.

To get the neutrino expectation, the MC events are weighted according to their generation weight introduced in Section 2.3.1, multiplied by the total lifetime, and the expected neutrino flux. For the correct expectation at the detector, the events have to be weighted by the oscillation probability, depending on their energy and their distance traveled from the atmosphere to the detector. The oscillation probabilities are calculated using a PYTHON implementation of the calculations from [109], which use the matter profile of the Earth following the *Preliminary Reference Earth Model (PREM)* [110] as input. Apart from the energy and the distance, the two relevant parameters defining the oscillation probabilities are the atmospheric neutrino oscillation parameters θ_{23} and Δm^2_{31}. Since the HNL events originate from the tau neutrinos that were produced as muon neutrinos in the atmosphere and then oscillated into ν_τ, this weighting is also applied in addition to the specific weighting scheme for the HNL events described in Section 2.2.3, which itself is defined by the mixing $|U^2_{\tau 4}|$ and the mass m_4.

[109]: Barger et al. (1980), "Matter effects on three-neutrino oscillations"
[110]: Dziewonski et al. (1981), "Preliminary reference Earth model"

3.1.1 Expected Rates/Events

The rates and the expected number of events for the SM background are shown in Table 3.1 with around 175000 total events expected in the 10 years. Only data marked as good is used for the analysis, where *good* refers to

measurement time with the correct physics run configuration and without other known issues. The resulting good detector livetime in this data taking period was 9.28 years. The rates are calculated by summing the weights of all events in the final level sample, while the uncertainties are calculated by taking the square root of the sum of the weights squared. The expected number of events is calculated by multiplying the rate with the livetime. The individual fractions show that this sample is neutrino dominated where the majority of events are ν_μ-CC events.

Table 3.1: Final level rates and event expectation of the SM background particle types.

Type	**Rate** [mHz]	**Events** (9.28 years)	**Fraction** [%]
ν_μ^{CC}	0.3531	103321 ± 113	58.9
ν_e^{CC}	0.1418	41490 ± 69	23.7
ν^{NC}	0.0666	19491 ± 47	11.1
ν_τ^{CC}	0.0345	10094 ± 22	5.8
μ_{atm}	0.0032	936 ± 15	0.5
total	0.5992	175332 ± 143	100.0

Table 3.2 shows the rates and expected number of events for the HNL signal simulation. The expectation depends on the mass and the mixing and shown here are two example mixings for all the three masses that are being tested in this work. A mixing of 0.0 would result in no HNL events at all. It can already be seen that for the smaller mixing of $|U_{\tau 4}|^2 = 10^{-3}$ the expected number of events is very low, while at the larger mixing of $|U_{\tau 4}|^2 = 10^{-1}$ the number is comparable to the amount of atmospheric muons in the background sample.

Table 3.2: Final level rates and event expectations of the HNL signal for all three masses and two example mixing values.

HNL mass	**Rate** [µHz]	**Events (in** 9.28 years**)**
$\lvert U_{\tau 4}\rvert^2 = 10^{-1}$		
0.3 GeV	3.3	975 ± 2
0.6 GeV	3.1	895 ± 2
1.0 GeV	2.5	731 ± 2
$\lvert U_{\tau 4}\rvert^2 = 10^{-3}$		
0.3 GeV	0.006	1.67 ± 0.01
0.6 GeV	0.022	6.44 ± 0.01
1.0 GeV	0.025	7.27 ± 0.01

3.1.2 Analysis Binning

[111]: Yu et al. (2023), "Recent neutrino oscillation result with the IceCube experiment"

An identical binning to the analysis performed in [111] is used. In total, there are three bins in PID (cascade like, mixed, and track like), 12 bins in reconstructed energy, and 8 bins in cosine of the reconstructed zenith angle as specified in Table 3.3.

Table 3.3: Three dimensional binning used in the analysis. All variables are from the FLERCNN reconstruction explained in Section **??**.

Variable	N_{bins}	**Edges**	**Spacing**
P_ν	3	[0.00, 0.25, 0.55, 1.00]	linear
E	12	[5.00, 100.00]	logarithmic
$\cos(\theta)$	8	[-1.00, 0.04]	linear

Extending the binning towards lower energies or increasing the number of bins in energy or cosine of the zenith angle did not improve the HNL sensitivities significantly, because the dominant signal region is already covered with a sufficiently fine binning to observe the shape and magnitude

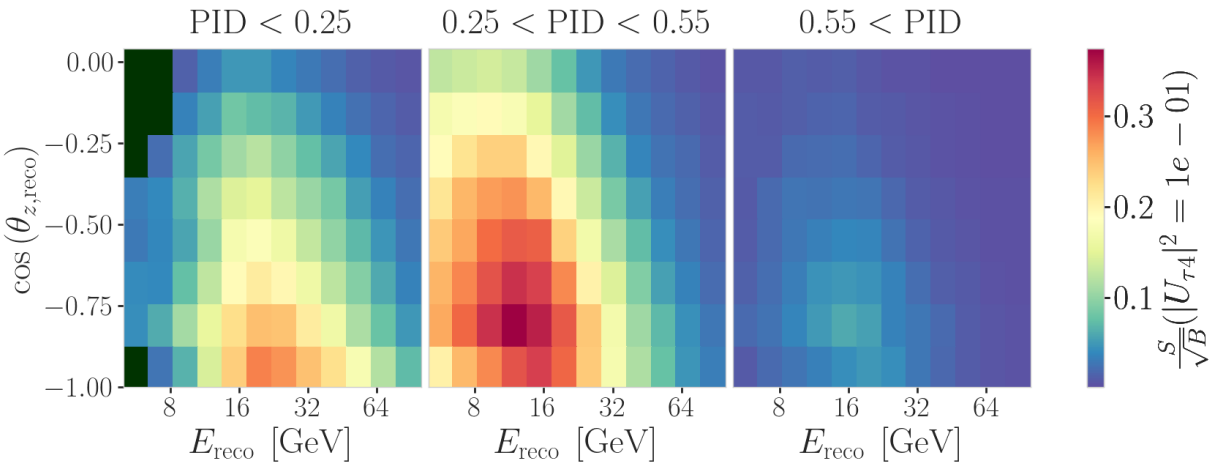

Figure 3.1: Signal over square root of background expectation in 9.28 years for the 1.0 GeV mass sample at a mixing of 0.1, while all other parameters are at their nominal values.

of the HNL events on top of the SM background. This can be seen in the middle panel of Figure 3.1, which shows the expected signal events divided by the square root of the expected background events for every bin used in the analysis. The signal expectation is using the 1.0 GeV mass sample at a reference mixing of 0.1, with the corresponding three dimensional histogram shown in Figure **??**. Both the nominal background expectation used to calculate the signal to square root of background ratio and the detector data can be seen in Figure 3.2.

Some low energy bins in the cascade like region have very low MC expectations (<1 event) and are therefore not taken into account in the analysis, to prevent unwanted behavior in the fit. Those are shown in dark green in the three dimensional histograms, and both background and data histograms show a strong decrease of events towards low energies in the cascade like bin. This background expectation is not necessarily supposed to agree with the data, because this is the distributions assuming nominal parameter values, before performing the fit to find the parameters that describe the data best. All parameters used in the analysis are discussed in Section 3.2.2, and post-fit data to MC comparisons are shown in Section 3.3.3.

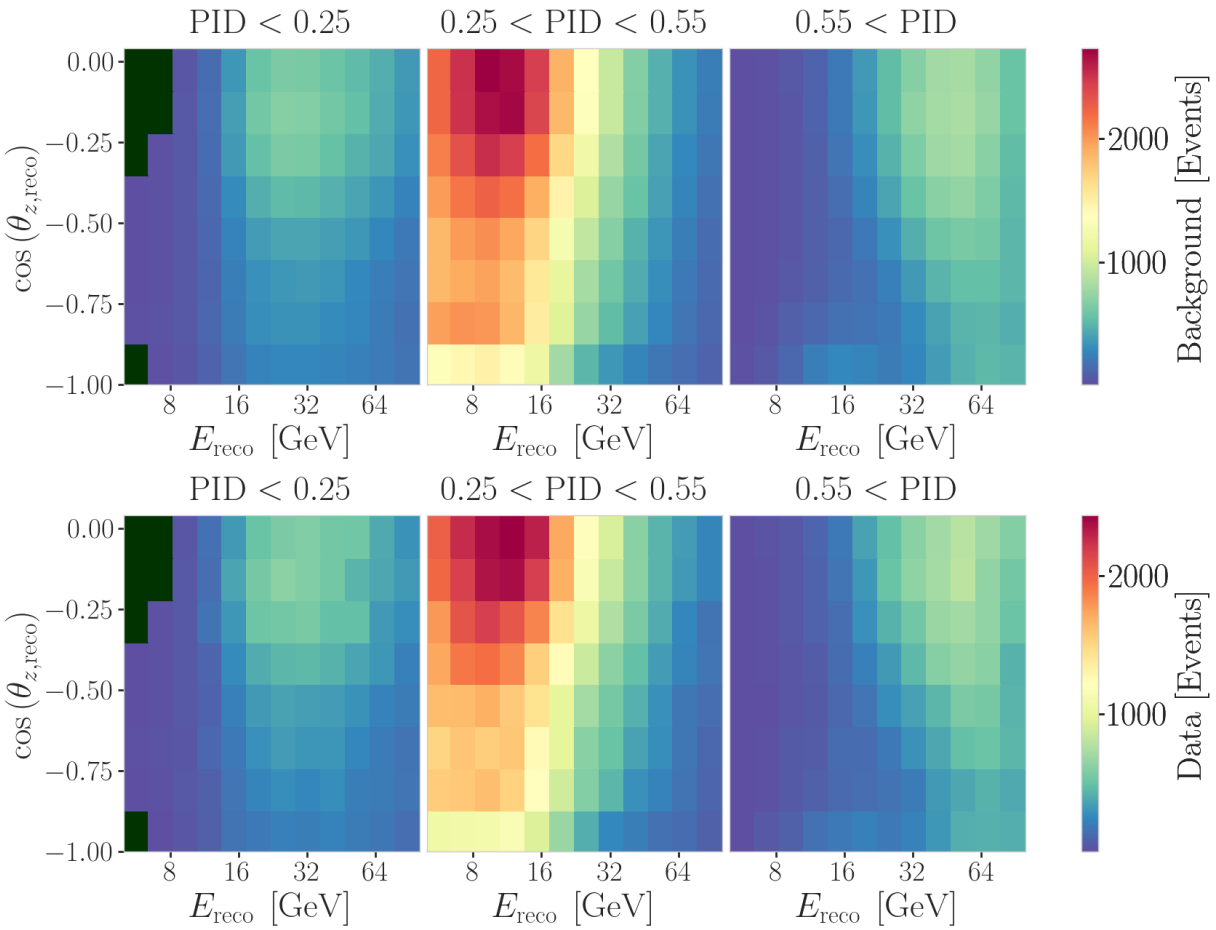

Figure 3.2: Background expectation in 9.28 years for all other parameters are at their nominal values (top) and observed data (bottom).

3.2 Statistical Analysis

3.2.1 Test Statistic

The measurements are performed by comparing the weighted MC to the data. Through variation of the nuisance and physics parameters that govern the weights, the best matching set of parameters can be found, by optimizing a fit metric. The comparison is done using a modified χ^2, defined as

$$\chi^2_{\text{mod}} = \sum_{i \in \text{bins}} \frac{(N_i^{\text{exp}} - N_i^{\text{obs}})^2}{N_i^{\text{exp}} + (\sigma_i^{\nu})^2 + (\sigma_i^{\mu})^2 + (\sigma_i^{\text{HNL}})^2} + \sum_{j \in \text{syst}} \frac{(s_j - \hat{s}_j)^2}{\sigma_{s_j}^2}, \tag{3.1}$$

as the fit metric. It is designed such that taking the difference between a free fit and a fit with fixed parameters based on a chosen hypothesis, $\Delta\chi^2_{\text{mod}}$, can directly be used as a *test statistic (TS)* for hypothesis testing, due to its asymptotic behavior. The total even expectation is $N_i^{\text{exp}} = N_i^{\nu} + N_i^{\mu} + N_i^{\text{HNL}}$, where N_i^{ν}, N_i^{μ}, and N_i^{HNL} are the expected number of events in bin i from neutrinos, atmospheric muons, and HNLs, while N_i^{obs} is the observed number of events in the bin. The expected number of events from each particle type is calculated by summing the weights of all events in the bin $N_i^{\text{type}} = \sum_i^{\text{type}} \omega_i$, with the statistical uncertainty being $(\sigma_i^{\text{type}})^2 = \sum_i^{\text{type}} \omega_i^2$. The additional term in Equation 3.1 is included to apply a penalty term for

prior knowledge of the systematic uncertainties of the parameters where they are known. s_j are the systematic parameters that are varied in the fit, while $\hat{s_j}$ are their nominal values and σ_{s_j} are the known uncertainties.

3.2.2 Physics Parameters

The variable physics parameter in this analysis is the mixing between the HNL and the SM τ sector, $|U_{\tau 4}|^2$. It is varied continuously in the range of [0.0 , 1.0] by applying the weighting scheme described in Section 2.2.3. The fit is initialized at an off-nominal value of 0.1. The other physics parameter, the mass m_4 of the HNL, is implicitly fixed to one of the three discrete masses to be tested, by using the corresponding sample of the HNL simulation described in Section 2.2.

3.2.3 Nuisance Parameters

There are multiple sources of systematic uncertainties related to the event generation and detector simulation explained in Chapter 2. All uncertainties considered in this work need to be implemented with parameters that can be varied continuously so that a simultaneous fit of the physics and systematic parameters can be performed. Where possible, a correct model of the effect is used, but in many cases the variations are captured by effective parameters. Uncertainties that solely scale the total event rate are not included individually, since the analysis only uses the relative distribution of events and a single scaling parameter N_ν is used to scale the total neutrino rate instead.

Atmospheric Flux Uncertainties

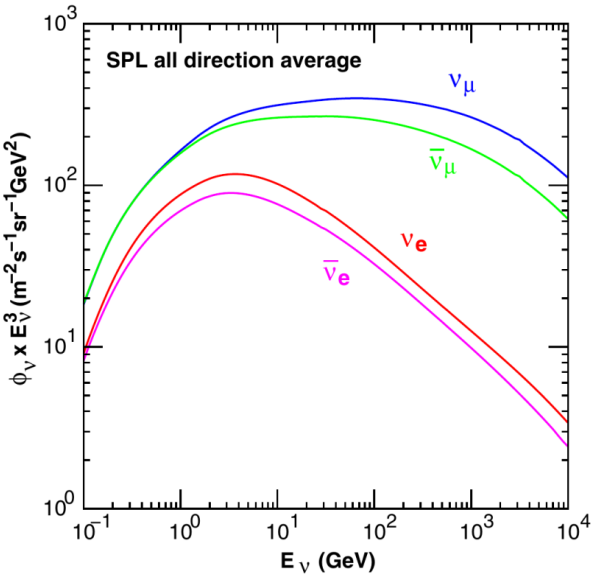

Figure 3.3: Atmospheric neutriono flux computed at the South Pole. Shown are the neutrino and antineutrino flux for ν_e and ν_μ. Taken from [74].

The flux of atmospheric neutrinos is influenced by multiple factors, the spectrum and composition of primary CRs, the atmospheric conditions, and the hadronic interaction model used to describe the air showers development. Uncertainties of the neutrino flux are therefore dictated by the uncertainties

on these components, where the variations in atmospheric conditions were found to have negligible effect [112]. The baseline neutrino flux used in this thesis is taken from [74]. Figure 3.3 shows the flux for neutrinos and antineutrinos, computed at the South Pole.

[112]: Abbasi et al. (2023), "Measurement of atmospheric neutrino mixing with improved IceCube DeepCore calibration and data processing"

[74]: Honda et al. (2015), "Atmospheric neutrino flux calculation using the NRLMSISE-00 atmospheric model"

Cosmic ray flux: The selected sample of atmospheric neutrinos lies around energies of up to 100 GeV. The initial primary particles in the CR flux can have 100 times larger energies and therefore the CR flux between 10 GeV and 10 TeV is important, which dominantly consists of hydrogen and helium nuclei [113]. The uncertainty in this CR flux component can be described as a power law correction [114, 115]

$$\Phi'_\nu = \Phi_\nu \left(\frac{E}{E^\star} \right)^{\Delta\gamma} , \tag{3.2}$$

where $E^\star$ is the pivot energy and $\Delta\gamma$ is the correction to the power law exponent. This modification propagates into the neutrino flux, which is therefore corrected in the same way. $E^\star$ was chosen to be 24 GeV as to minimize the dependence of the overall flux scale on $\Delta\gamma$ [112].

[113]: Dembinski et al. (2017), "Data-driven model of the cosmic-ray flux and mass composition from 10 GeV to 10^{11} GeV"

[114]: Barr et al. (2006), "Uncertainties in atmospheric neutrino fluxes"

[115]: Evans et al. (2017), "Uncertainties in atmospheric muon-neutrino fluxes arising from cosmic-ray primaries"

[112]: Abbasi et al. (2023), "Measurement of atmospheric neutrino mixing with improved IceCube DeepCore calibration and data processing"

Hadronic interaction model: Neutrinos are produced from the decaying hadrons (dominantly pions and kaons) in CR air shower, spanning a large parameter space that is sparsely evaluated by experimental data. To include uncertainties based on energy, direction, and neutrino flavor, the MCEq package [116] is used to compute the distribution of atmospheric leptons and to estimate the impact of varying their contributions. The calculations result in the change in flux $\mathrm{d}\Phi_\mathrm{l}/\mathrm{d}B$ for a variation $\mathrm{d}B$ of some parameter B. Scaling this variation by some value b, the modified total flux, s is then given by

$$\Phi'_\mathrm{l} = \Phi_\mathrm{l} + \left(b \cdot \frac{\mathrm{d}\Phi_\mathrm{l}}{\mathrm{d}B} \right) . \tag{3.3}$$

Matching the work in [117], the parameter space is divided in regions of the primary energy, E_i, and the energy fraction of the secondary meson, x_lab, with varying uncertainties, derived from fixed target experiment data. The Sibyll2.3c [118] hadronic interaction model and the GSF CR flux [113] were used to calculate the related flux changes[1] for the different regions in E_i and x_lab, resulting in 17 variables, encoding the possible changes. Figure 3.4 shows the selected regions of the parameter space and the names given to the uncertainties. At the energies relevant for this work, the flux is dominantly affected by the pion uncertainties. The variational term in Equation 3.3 is applied for each of these parameters and the total variation is the sum of all individual variations.

[117]: Barr et al. (2006), "Uncertainties in Atmospheric Neutrino Fluxes"

[118]: Riehn et al. (2020), "Hadronic interaction model sibyll 2.3d and extensive air showers"

[113]: Dembinski et al. (2017), "Data-driven model of the cosmic-ray flux and mass composition from 10 GeV to 10^{11} GeV"

1: The choice of flux and hadronic interaction model have negligible impact on the variations.

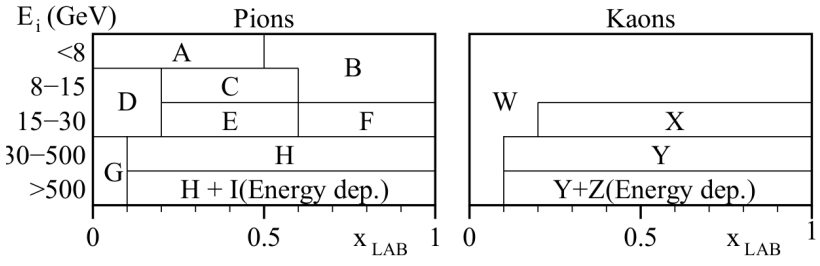

Figure 3.4: Flux uncertainty regions of the hadronic interaction model in the phase space of the primary energy E_i and the energy fraction of the secondary meson x_lab. Taken from [117].

Cross-Section Uncertainties

The uncertainties related to the cross-sections are split into low and high energy components, since there is no coherent model to explain both regimes. Below 20 GeV, *charged current resonance production (CCRES)* and *charged current quasi elastic scattering (CCQE)* interactions with the nucleons as a whole are important, while above 20 GeV DIS interactions are the dominant processes. Three parameters are included to account for all relevant cross-section uncertainties.

At low energies two parameters are included to account for uncertainties in form factors of CCQE and CCRES events. These uncertainties are due to uncertainties in the *axial mass* M_{A}, which enters the form factor as in

$$F(Q^2) \sim \frac{1}{(1 - (\frac{Q}{M_{\mathrm{A}}})^2)^2} \,, \tag{3.4}$$

where Q^2 is the momentum transfer squared. The axial mass can be determined experimentally and to include uncertainties on the values of $M_{\mathrm{A}}^{\mathrm{CCQE}}$ and $M_{\mathrm{A}}^{\mathrm{CCRES}}$, the cross-sections are computed for each event, where the form factors are calculated varying the axial mass by $\pm 20\%(1\sigma)/\pm 40\%(1\sigma)$ around the nominal value. This is an approximation of the recommended uncertainties by the GENIE collaboration, which are -15%, $+25\%$ for $M_{\mathrm{A}}^{\mathrm{CCQE}}$ and $\pm 20\%$ for $M_{\mathrm{A}}^{\mathrm{CCRES}}$ [92]. To apply a continuous uncertainty variation of the axial mass in a fit, the total cross-section is fit with a quadratic function to interpolate between the cross-sections computed with the different axial masses.

Even though the DIS interactions can be calculated very precisely, there are still uncertainties in the input PDF, describing the probability of finding a specific parton (quark) with a specific momentum fraction x inside a nucleon. To account for differences between the used method and more sophisticated methods using newer PDFs seen at high energies, an uncertainty parameter is introduced. The parameter is based on the discrepancy between the cross-sections computed with GENIE and the ones computed with CSMS [119] above 100 GeV. The included parameter scales the cross-section from the GENIE values to the CSMS values, which are considered more accurate above 100 GeV. The scaling is done as a function of energy and inelasticity and to guarantee continuity, the scaling is extrapolated linearly below 100 GeV[2]. The parameter is designed such that a value of 0.0 corresponds to the GENIE cross-sections and a value of 1.0 gives an approximation of the CSMS cross-sections. A comparison of the total cross-sections GENIE (scaled/unscaled) with the data is shown in Figure 3.5.

[119]: Cooper-Sarkar et al. (2011), "The high energy neutrino cross-section in the Standard Model and its uncertainty"

2: Multiple functional extrapolations were tested, but the choice was found to have negligible impact.

Muon Uncertainties

The muon fraction in the final level selection (see Section **??**) is below 1 %, therefore additional muon systematic uncertainties apart from the spectral index are not implemented, but rather a total muon scaling parameter is added. This total scale is somewhat degenerate with the DOM efficiency, since an increased DOM efficiency leads to better muon rejection. Both the total muon scaling and the muon spectral index have a very small impact on the analysis as will be shown in Section 3.

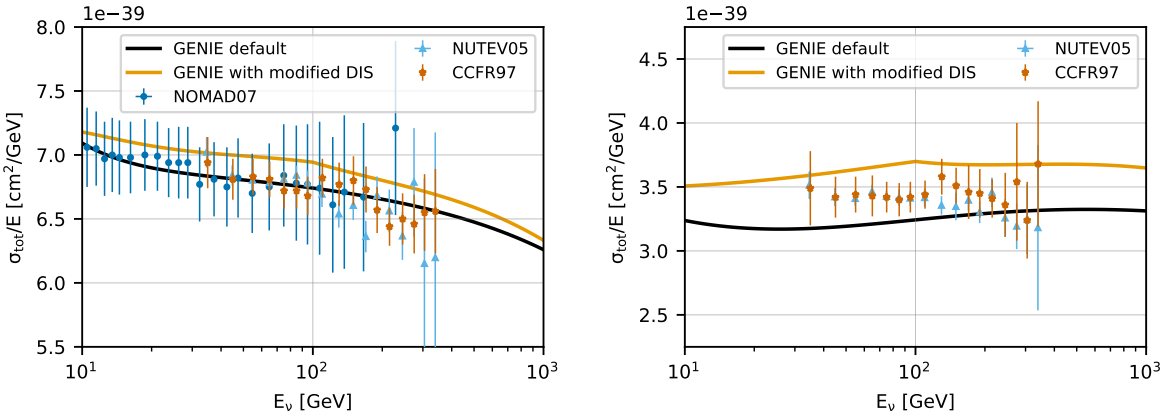

Figure 3.5: Inclusive total neutrino-nucleon cross-sections on an isoscalar target (black) for neutrinos (left) and antineutrinos (right) calculated with GENIE, comparing to measurements from NOMAD [120], NUTEV [121], and CCFR [122]. The scaled GENIE cross-section (orange) is also shown. Taken from [112].

Detector Calibration Uncertainties

The detection process of neutrinos in IceCube has several sources of uncertainties, where the effects of the properties of the ice itself and the optical efficiency of the DOMs are dominant for this analysis. None of these uncertainties can be described by an analytic expression, so instead their effects are estimated using MC simulation. This is done by producing additional simulation samples at discrete values of those parameters. The five relevant uncertainty parameters are the absolute efficiency of the DOMs, a global scaling of ice scattering and absorption lengths, and variations of the relative angular acceptance due to hole ice variations in two parameters. To perform the fit, continuous variations with respect to these parameters will be derived with a method explained in Section 3.

Relative DOM efficiency: As was already mentioned in Section **??**, the absolute efficiency of the DOMs, ϵ_{DOM} is calibrated using minimum ionizing muons from air showers, due to the lack of a calibrated light source in the detector. Using the muons as a steady, controlled source of light, the efficiency can be estimated by comparing simulated muon data sets with varied DOM response to the measured data. Since the uncertainties found in multiple iterations of this study [123, 124] are at the order of 10 %, this systematic is highly relevant and is included in the analysis.

[123]: Feintzeig (2014), "Searches for Point-like Sources of Astrophysical Neutrinos with the IceCube Neutrino Observatory"
[124]: Kulacz (2019), "In Situ Measurement of the IceCube DOM Efficiency Factor Using Atmospheric Minimum Ionizing Muons"

Ice scattering and absorption: Absorption and scattering length are the most important properties that govern the propagation of photons through the ice. The simulation principle and how the depth dependent absorption and scattering coefficients are used was already explained in Section 2.4.1. To account for uncertainties on this model of the ice coefficients, a global scaling for each of the two parameters (global absoprtion, global scatteriong) is applied.

Hole ice angular acceptance: Due to bubble formation in the re-freezing process of the boreholes, the hole ice seems to be less transparent in the center of the columns [125]. This effectively decreases the chance of pho-

[125]: Rongen, Martin (2016), "Measuring the optical properties of IceCube drill holes"

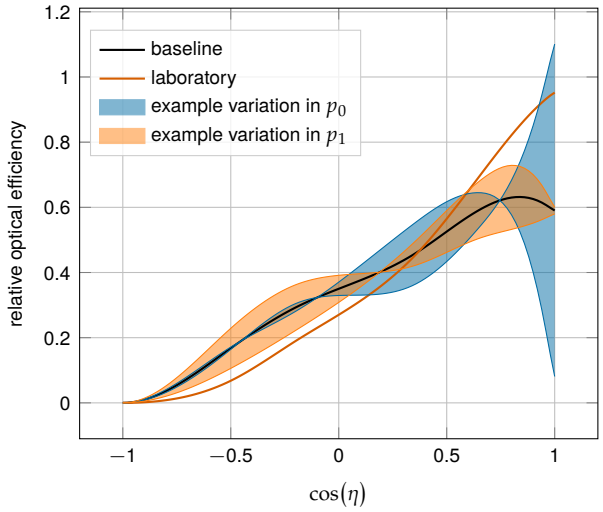

Figure 3.6: Relative angular acceptance modification due to hole ice. Shown is the current baseline model, the variations from changing p_0 and p_1, and a laboratory measurement. Modified from [13].

tons hitting the DOMs directly from below, which can be described as an additional angular modification of the DOM acceptance. The modification is parameterized by a two dimensional, normalized[3] function, where the two dominant of the parameters (p_0, p_1), dictating its form, are enough to describe all past and the current hole ice models from both *in-situ* and laboratory measurements. Figure 3.6 shows the acceptance modification as a function of the incident photon angle $\cos(\eta)$. The current baseline model, the variations achieved through modifying p_0 and p_1, and a laboratory measurement can be seen.

3: The hole ice angular acceptance modification is normalized so that it does not affect the total charge.

Ice Model: The ice model used in IceCube is continuously improved, and the recent models incorporate the birefringent polycriystalline microstructure [126] into the ice properties. To account for the uncertainty, due to this unmodeled effect in the ice model used for the simulation production, an additional simulation sample is produced using the newer version of the ice model, that incorporates the *birefringence (BFR)* effect.

[126]: Abbasi et al. (2024), "In situ estimation of ice crystal properties at the South Pole using LED calibration data from the IceCube Neutrino Observatory"

Treatment of Detector Systematic Uncertainties Since the variations related to the detector calibration uncertainties introduced in Section 2 are estimated by simulating MC at discrete values of the systematic parameters, a method to derive continuous variations is needed to perform the fit. The method applied here was initially introduced in [127] and first used in the low energy sterile neutrino search in [13] (section 7.4.3). Using a *likelihood-free inference* technique, re-weighting factors are found for every event in the nominal MC sample, given a specific choice of detector systematic parameters. These factors quantify how much more or less likely the event would be for the corresponding change in detector response from the nominal parameters. Without going into the details of the method, which were already exhaustively discussed in [127] and [13], the performance is assessed here for the HNL signal simulation. In order to do so, the weights are applied to the nominal MC samples, choosing the detector systematic values used to produce the discrete samples and the resulting event expectations are compared to the expectations from the individual, discrete MC samples. The

[127]: Fischer et al. (2023), "Treating detector systematics via a likelihood free inference method"
[13]: Trettin (2023), "Search for eV-scale sterile neutrinos with IceCube DeepCore"

bin counts are compared by calculating the pull defined as

$$p = \frac{N_{\text{reweighted}} - N_{sys}}{\sqrt{\sigma^2_{\text{reweighted}} + \sigma^2_{sys}}}\,, \tag{3.5}$$

where N are the bin-wise event expectations and σ are their MC uncertainty. For the SM BG simulation, the performance was already investigated in [128] (section 7.4.4, appendix B5) and the re-weighted nominal MC was shown to be in agreement with the discrete systematic sets at a sufficient level. Figure **??** shows the bin-wise pulls for the 1.0 GeV HNL mass sample at a mixing of 0.1 for a selection of the discrete systematic samples, where the DOM efficiency and the ice absorption was varied by ±10%. As expected, the pull distributions follow a standard normal distribution, without strong clustering or any systematic deviations. A similar performance is found for the additional systematic variations and the detailed figures can be found in Section **??**.

[128]: Lohfink (2023), "Testing non-standard neutrino interaction parameters with IceCube-DeepCore"

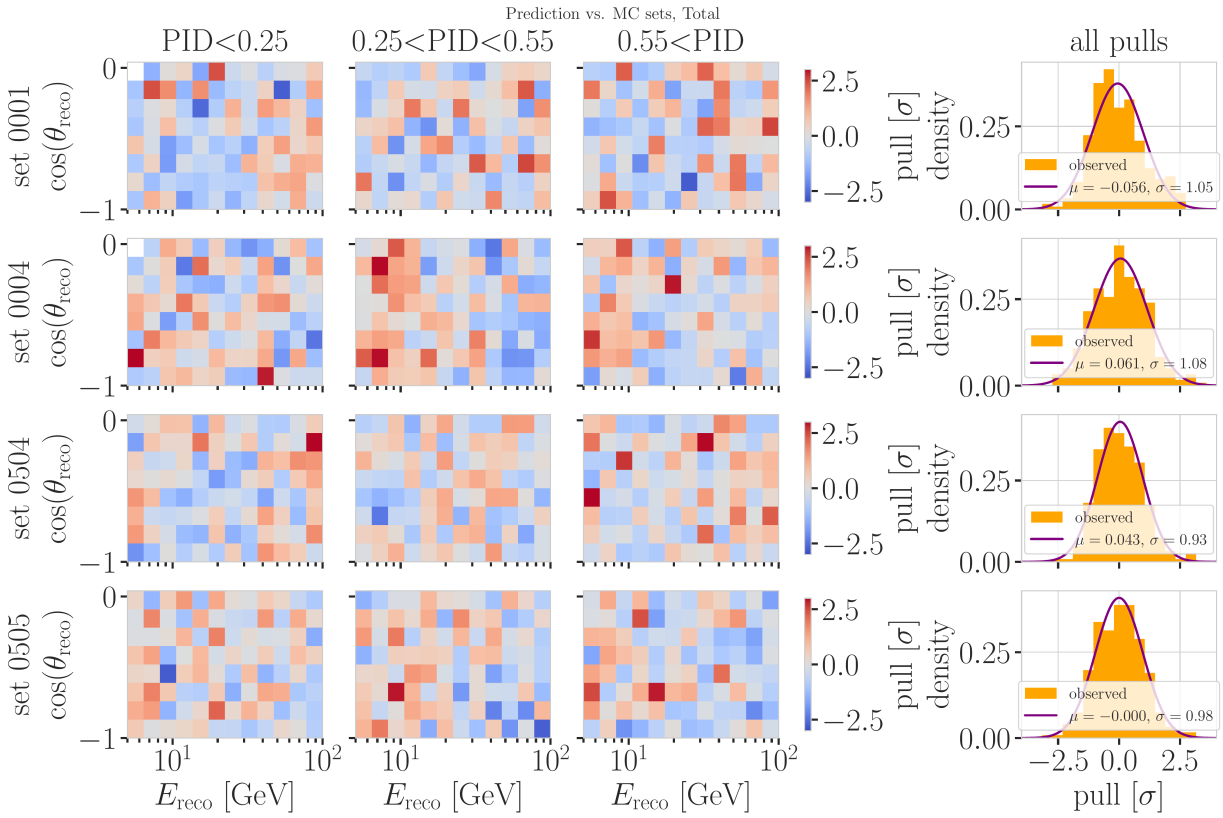

Figure 3.7: Three dimensional pulls and set-wise pull distributions between the nominal set and the specific systematic sets, after the nominal set was re-weighted to the correspoinding systematic parameter value. Set 0001 and 0004 have the DOM efficiency varied by ±10%, while set 0504 and 0505 have the ice absorption varied by ±10%.

Free Parameters

To decide which systematic uncertainties should be included in the fit, we test the potential impact they have on the TS if they are neglected. The test is performed by creating pseudo-data sets from the MC by choosing the nominal nuisance parameters and specific physics parameters, without adding any statistical or systematic fluctuations to it. These so-called *.Asimov* [4] are made with the BG simulation and the HNL simulation of the 1.0 GeV

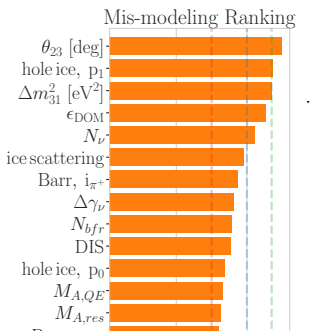

mass sample at a mixing value of 0.1, which is chosen as a benchmark physics parameter, but the explicit choice does not have a significant impact on the test. The systematic parameter of interest is set to a value above its nominal expectation, either pulled up by $+1\sigma$ or by an educated estimate for parameters without a well-defined uncertainty. A fit is performed fixing the systematic parameter of interest and leaving all additional parameters free. The resulting TS is the fit metric difference between between this fit and a fit with all parameters free, which would result in a fit metric of 0.0 for this Asimov test. This difference is called mis-modeling significance and parameters below a significance of 0.1 σ are fixed. The test is performed in an iterative manner until the final set of free parameters is found.

Figure 3.8 shows the resulting significances of one of these tests. The parameters tested are the systematic parameters introduced in Section 3.2.3 and the atmospheric oscillation parameters mentioned in Section 3.1. In the final selection of free parameters the Barr h_{π^+} parameter was also left free, to sufficiently cover the relevant energy production range of the Pions, as can be seen in Figure 3.4, where both for Kaons and Pions the uncertainties are included for primary energies above 30 GeV and $x_{\text{lab}} > 0.1$. Additionally, the ice absorption is still kept free, despite showing a small significance, which is done because the ice parameters are not well constrained and are known to have a large impact, which might be concealed in this idealized test, due to correlations with the other parameters. In this test, the effect of correlations is challenging to consider, because only the impact of one parameter is tested at a time, using the overall mis-modeling significance as a measure. The mis-modeling could be reduced by a correlated parameter capturing the effect of the parameter of interest. For this reason a very conservative threshold of 0.1 σ is chosen and some parameters below the threshold are still left free in the fit.

All nuisance parameters that are left free in the fit are summarized in Table 3.4, showing their nominal values, the allowed fit ranges, and their Gaussian prior, if applicable. The scaling parameter N_ν is included to account for the overall normalization of the neutrino rate, and it has the identical effect on the SM neutrino events and the BSM HNL events, because they both originate from the same neutrino flux. Despite being known to ~5 % in this energy range [74], there is no prior applied to this parameter, because the fit itself is able to constrain it well, which can be seen by the large impact it shows in Figure 3.8. Concerning the atmospheric neutrino flux, the CR power law flux correction factor $\Delta\gamma_\nu$ introduced in Section 3.2.3 is included with nominal value of 0.0 which corresponds to the baseline flux model. A slightly conservative prior of 0.1 is applied to the parameter, while latest measurements show an uncertainty of 0.05 [115]. The Barr parameters are contrained by a Gaussian prior, taken from [117]. All the detector systematic uncertainties discussed in Section 2 are included in the fit. The DOM efficiency ϵ_{DOM} is constrained by a Gaussian prior with a width of 0.1, which is a conservative estimate based on the studies of the optical efficiency using minimum ionizing muons from [123, 124]. The two atmospheric neutrino oscillation parameters θ_{23} and Δm^2_{31} are also included in the fit with nominal values of 47.5° and $2.48 \times 10^{-3}\,\text{eV}^2$ [111], respectively. Since they govern the shape and the strength of the tau neutrino flux, by defining the oscillation from ν_μ to ν_τ, they are also relevant for the HNL signal shape.

[74]: Honda et al. (2015), "Atmospheric neutrino flux calculation using the NRLMSISE-00 atmospheric model"

[115]: Evans et al. (2017), "Uncertainties in atmospheric muon-neutrino fluxes arising from cosmic-ray primaries"

[117]: Barr et al. (2006), "Uncertainties in Atmospheric Neutrino Fluxes"

[123]: Feintzeig (2014), "Searches for Point-like Sources of Astrophysical Neutrinos with the IceCube Neutrino Observatory"

[124]: Kulacz (2019), "In Situ Measurement of the IceCube DOM Efficiency Factor Using Atmospheric Minimum Ionizing Muons"

[111]: Yu et al. (2023), "Recent neutrino oscillation result with the IceCube experiment"

Table 3.4: Systematic uncertainty parameters that are left free to float in the fit. Their allowed fit ranges are shown with the nominal value and the Gaussian prior width if applicable.

Parameter	Nominal	Range	Prior
$\theta_{23}[^\circ]$	47.5047	[0.0, 90.0]	-
$\Delta m^2_{31}[\text{eV}^2]$	0.002475	[0.001, 0.004]	-
N_ν	1.0	[0.1, 2.0]	-
$\Delta\gamma_\nu$	0.0	[-0.5, 0.5]	0.1
Barr h_{π^+}	0.0	[-0.75, 0.75]	0.15
Barr i_{π^+}	0.0	[-3.05, 3.05]	0.61
Barr y_{K^+}	0.0	[-1.5, 1.5]	0.3
DIS	0.0	[-0.5, 1.5]	1.0
$M_{\text{A,QE}}$	0.0	[-2.0, 2.0]	1.0
$M_{\text{A,res}}$	0.0	[-2.0, 2.0]	1.0
ϵ_{DOM}	1.0	[0.8, 1.2]	0.1
hole ice p_0	0.101569	[-0.6, 0.5]	-
hole ice p_1	-0.049344	[-0.2, 0.2]	-
ice absorption	1.0	[0.85, 1.15]	-
ice scattering	1.05	[0.9, 1.2]	-
N_{bfr}	0.0	[-0.2, 1.2]	-

3.2.4 Low Energy Analysis Framework

[129]: Aartsen et al. (2020), "Computational techniques for the analysis of small signals in high-statistics neutrino oscillation experiments"

The analysis is performed using the PISA [129] [130] software framework, which was developed to perform analyses of small signals in high-statistics neutrino oscillation experiments. It is used to generate the expected event distributions from several MC samples, which can then be compared to the observed data. The expectation for each MC sample is calculated by applying physics and nuisance parameter effects in a stage-wise manner, before combining them to the final expectation.

3.3 Analysis Checks

[131]: Nickerson (1998), "Confirmation Bias: A Ubiquitous Phenomenon in Many Guises"

Fitting to data is performed in a *blind* manner, where the analyzer does not immediately see the fitted physics and nuisance parameter values, but first checks that a set of pre-defined *goodness of fit (GOF)* criteria are fulfilled. This is done to circumvent the so-called *confirmation bias* [131], where the analyzer might be tempted to construct the analysis in a way that confirms their expectation. After the GOF criteria are met to satisfaction, the fit results are unblinded and the full result can be revealed. Before these blind fits to data are performed, the robustness of the analysis method is tested using pseudo-data that is generated from the MC.

3.3.1 Minimization Robustness

5: There is a degeneracy between the lower octant ($\theta_{23} < 45°$) and the upper octant ($\theta_{23} > 45°$), which can lead to fit metric minima (local and global) at two positions that are mirrored around 45° in θ_{23}.

[132]: Dembinski et al. (2022), *scikit-hep/iminuit: v2.17.0*

[133]: James et al. (1975), "Minuit: A System for Function Minimization and Analysis of the Parameter Errors and Correlations"

Fit	Err.	Prec.	Tol.
Coarse	1e-1	1e-8	1e-1
Fine	1e-5	1e-14	1e-5

Table 3.5: Migrad settings for the two stages in the minimization routine. *Err.* are the step size for the numerical gradient estimation, *Prec.* is the precision with which the LLH is calculated, and *Tol.* is the tolerance for the minimization.

To find the set of parameters that best describes the data, a staged minimization routine is used. In the first stage, a fit with coarse minimizer settings is performed to find a rough estimate of the *best fit point (BFP)*. In the second stage, the fit is performed again in both octants[5] of θ_{23}, starting from the BFP of the coarse fit. For each individual fit the *MIGRAD* routine of IMINUIT [132] is used to minimize the χ^2_{mod} fit metric defined in Equation 3.1. Iminuit is a fast, python compatible minimizer based on the MINUIT2 C++ library [133]. The individual minimizer settings for both stages are shown in Table 3.5.

To test the minimization routine and to make sure it consistently recovers any physics parameters, Asimov data sets are produced and then fit back with the full analysis chain. This type of test is called *Asimov inject/recover test*. A set of mixing values between 10^{-3} and 10^{0} is injected and fit back. Without fluctuations the fit is expected to always recover the injected parameters (both physics and nuisance parameters). The fitted mixing values from the Asimov inject/recover tests are compared to the true injected values in Figure 3.9 for all three mass samples. As desired, the fit is always able to recover the injected physics parameter and the nuisance parameters within the statistical uncertainty or at an insignificant fit metric difference.

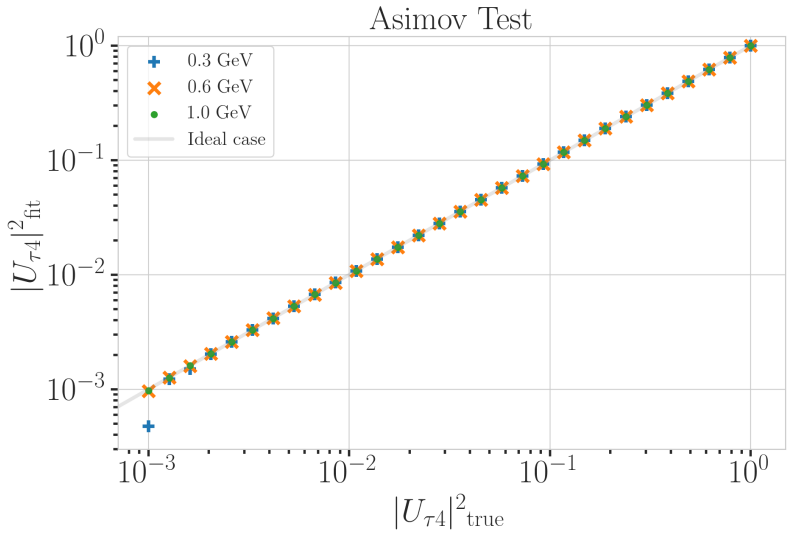

Figure 3.9: Asimov inject/recover test results for all three mass samples. Mixing values between 10^{-3} and 10^{0} are injected and fit back with the full analysis chain. The injected parameter is always recovered within the statistical uncertainty or at an insignificant fit metric difference.

3.3.2 Goodness of Fit

To estimate the GOF, pseudo-data is generated from the MC by injecting the BFP parameters as true parameters and then fluctuating the expected bin counts to account for MC uncertainty and Poisson fluctuations in data. First, the expectation value of each bin is drawn from a Gaussian distribution centered at the nominal expectation value with a standard deviation corresponding to the MC uncertainty of the bin. Based on this sampled expectation value, each bin count is drawn from a Poisson distribution, independently, to get the final pseudo-data set. These pseudo-data sets are analyzed with the same analysis chain as the real data, resulting in a final fit metric value for each pseudo-data set. By comparing the distribution of fit metric values from this *ensemble* of pseudo-data trials to the fit metric of the fit to real data, a p-value can be calculated. The p-value is the probability of finding a value of the fit metric at least as large as the one from the data fit. Figure 3.10 shows the distribution from the ensemble tests for the 0.6 GeV mass sample and the observed value from the fit, resulting in a p-value of 28.5 %. The p-values for the 0.3 GeV and 1.0 GeV are 28.3 % and 26.0 %, respectively, and the corresponding plots are shown in Section **??**. Based on this test, it is concluded that the fit result is compatible with the expectation from the ensemble of pseudo-data trials.

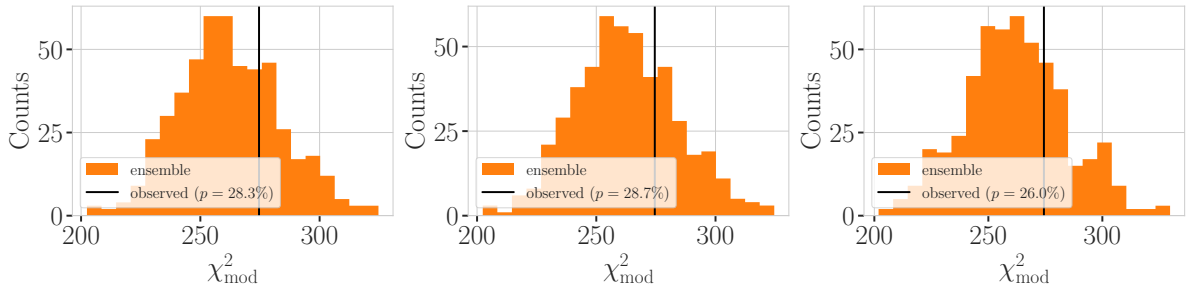

Figure 3.10: Observed fit metric (data fit) and fit metric distribution from pseudo-data ensemble generated around the best fit point. Shown are the results for all three mass samples, with the ensemble distribution on orange, the observed value in black, and the p-value in the legend.

3.3.3 Data/MC Agreement

At the BFP, the agreement between the data and simulation is probed by comparing both the one dimensional analysis distributions for PID, energy, and cosine of the zenith angle as well as the full three dimensional distributions. Figure 3.11 shows the three dimensional pull distribution between data and the total MC expectation for the 0.6 GeV mass sample at the BFP. The pulls are evenly spaced and show no strong clustering. In Figure **??**, two examples of the one dimensional distributions for the energy and cosine of the zenith angle are shown for the 0.6 GeV mass sample. The data is compared to the total MC expectation, which is also split up into the individual signal and background components for illustration. Good agreement can be observed in the pull distributions, and is quantified by a reduced χ^2, which is close to 1.0 for all distributions. The reduced χ^2 for all investigated distributions is listed in Table **??**, while the distributions themselves can be found in Section **??**.

add 1-d data/mc agreement for example mass sample (0.6?) and all 3 analysis variables (RED)

add table with reduced chi2 for all 1-d distributions (RED)

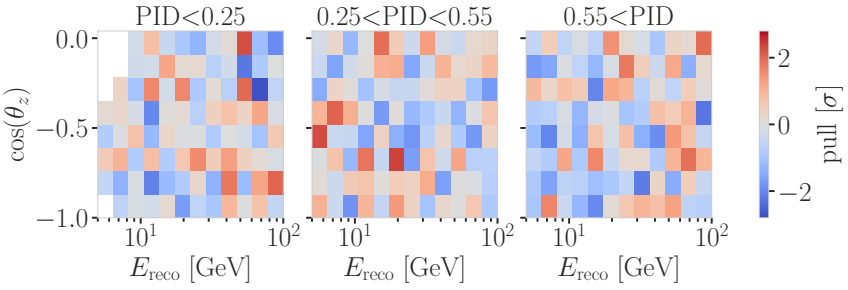

Figure 3.11: Three dimensional binwise pulls between data and simulation at the best fit point of the 0.6 GeV mass sample fit.

3.4 Results

3.4.1 Best Fit Nuisance Parameters

The resulting nuisance parameter values from the fits are illustrated in Figure 3.12, where the differences to the nominal values are shown, normalized by the distance to the closest boundary. The results from all three fits are shown in the same plot and the fits prefer values of the same size for all three mass samples. For parameters that have a Gaussian prior, the 1 σ range is also displayed. As was already confirmed during the blind fit procedure, all fitted parameters are within this range. The effective ice model parameter, N_{bfr}, prefers a value of ~0.74 , indicating that the data fits better to an ice model that includes real birefringence effects [126]. For completeness, the

[126]: Abbasi et al. (2024), "In situ estimation of ice crystal properties at the South Pole using LED calibration data from the IceCube Neutrino Observatory"

explicit results are listed in Table **??**. There, the nominal values and the absolute differences to the best fit value are also presented.

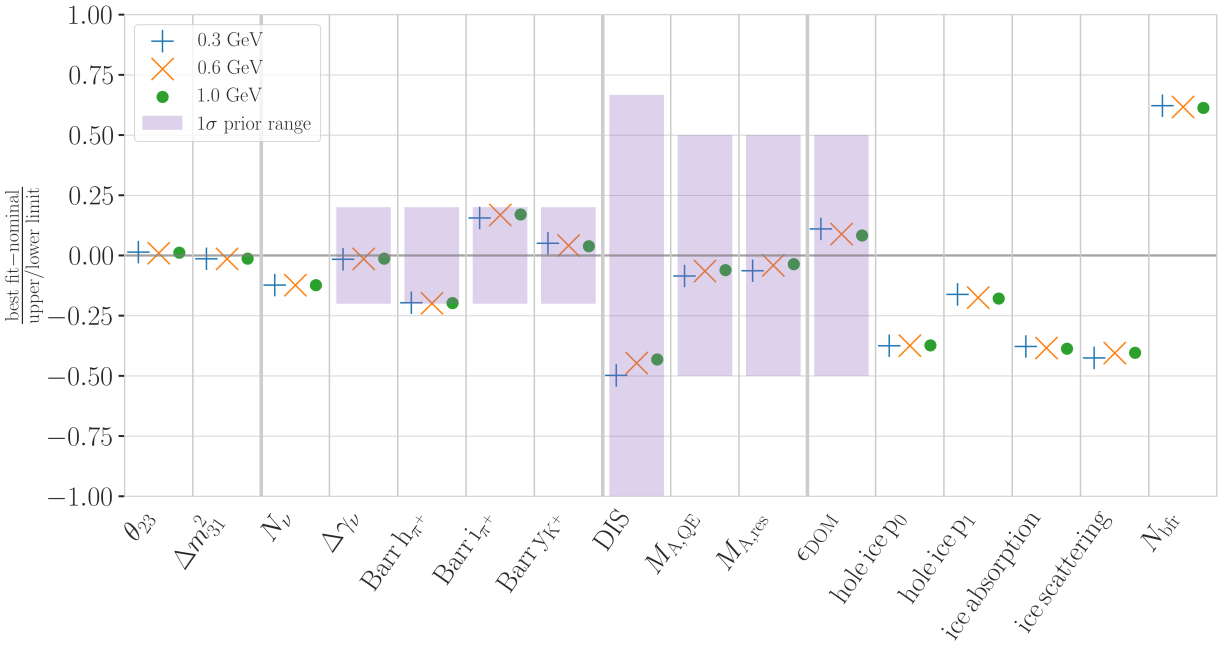

Figure 3.12: Best fit nuisance parameter distances to the nominal values, normalized by the distance to the closest boundary. For parameters with a Gaussian prior, the +1 σ range is also shown.

3.4.2 Agreement with Standard Model Three-Flavor Oscillation Measurement

The recently performed atmospheric neutrino oscillation measurement by the IceCube collaboration resulted in a best fit point of $\sin^2\theta_{23} = 0.544^{+0.030}_{-0.096}$ and $\Delta m^2_{32} = 2.40^{+0.03}_{-0.06} \times 10^{-3}\text{eV}^2$ [111]. The result used the identical 10 years of data at the same final level selection, assuming normal mass ordering. The differences to this analysis are the choice of fit metric and the use of the previous treatment of detector systematic uncertainties. Both the choice of the fit metric and the detector systematic uncertainty treatment should not influence the best fit values and a naive comparison of the results to the results from this work is done, to validate this is the case. The best fit values are listed in Table 3.6 and are all compatible with the IceCube result within the uncertainties. Since they are statistically fully dependent, a more rigorous quantitative comparison would be more involved and is not performed here. The agreement is still interpreted as a first validation of the new detector systematics treatment.

m_4	$\sin^2\theta_{23}$	Δm^2_{32} [eV^2]
0.3 GeV	0.554	0.0238
0.6 GeV	0.551	0.0238
1.0 GeV	0.553	0.0238

Table 3.6: Best fit oscillation parameters from the three mass sample fits. The values are compatible with the IceCube result within the uncertainties.

[111]: Yu et al. (2023), "Recent neutrino oscillation result with the IceCube experiment"

3.4.3 Best Fit Parameters and Limits

The fitted mixing values are

$$|U_{\tau 4}|^2(0.3\,\text{GeV}) = 0.003^{+0.084}\,,$$
$$|U_{\tau 4}|^2(0.6\,\text{GeV}) = 0.080^{+0.134}\,,\text{and}$$
$$|U_{\tau 4}|^2(1.0\,\text{GeV}) = 0.106^{+0.132}\,,$$

with their +1 σ uncertainty. All of them are compatible with the null hypothesis of 0.0 mixing, although the 0.6 GeV and 1.0 GeV fits indicate a mixing value of 0.08 and 0.106 , respectively. The best fit mixing values and the corresponding upper limits at 68 % and 90 % *confidence level (CL)* are listed in Table 3.7, also showing the p-value to reject the null hypothesis. The CLs and p-value are estimated by assuming that *Wilks' theorem* [134] holds, meaning that the TS follows a χ^2 distribution with one degree of freedom.

[134]: Wilks (1938), "The Large-Sample Distribution of the Likelihood Ratio for Testing Composite Hypotheses"

Table 3.7: Best fit mixing values and the corresponding upper limits at 68 % and 90 % confidence level, as well as the p-value to reject the null hypothesis, estimated by assuming that Wilks' theorem holds.

HNL mass	$\lvert U_{\tau 4}\rvert^2$	68 % CL	90 % CL	NH p-value
0.3 GeV	0.003	0.09	0.19	0.97
0.6 GeV	0.080	0.21	0.36	0.79
1.0 GeV	0.106	0.24	0.40	0.63

Figure 3.13 shows the observed TS profiles as a function of $|U_{\tau 4}|^2$ for all three fits. The TS profile is the difference in χ^2_{mod} between the free fit and a fit where the mixing is fixed to a specific value. Also shown is the expected TS profile, based on 100 pseudo-data trials, produced at the BFP and then fluctuated using both Poisson and Gaussian fluctuations, to include the data and the MC uncertainty as was explained in Section 3.3.2. The Asimov expectation and the 68 % and 90 % bands are shown and the observed TS profiles lie within the 68 % band for all three, confirming that they are compatible with statistical fluctuations of the observed data. For the 0.3 GeV fit, the observed contour is slightly tighter than the Asimov expectation, meaning that the observed upper limits in $|U_{\tau 4}|^2$ are slightly stronger than expected. For the 0.6 GeV the opposite is the case and the observed upper limit is therefore slightly weaker than expected. For the 1.0 GeV fit, the observed upper limit is very close to the Asimov expectation in the region where the 68 % and 90 % CLs thresholds are crossed. The observed upper limits are also shown in Table 3.7.

3.5 Summary and Outlook

tododiscuss how this compares to other experiments (it's far, far below the existing limits..) (RED)

3.5.1 Analysis Improvements

- estimate full contribution from cascade only events (underestimated due to limited sampling distributions)
- include double cascade classifier into Binning
- further optimize binning

Test Coupling to Electron/Muon Flavor

Test Additional Coupling Processes

IceCube Upgrade

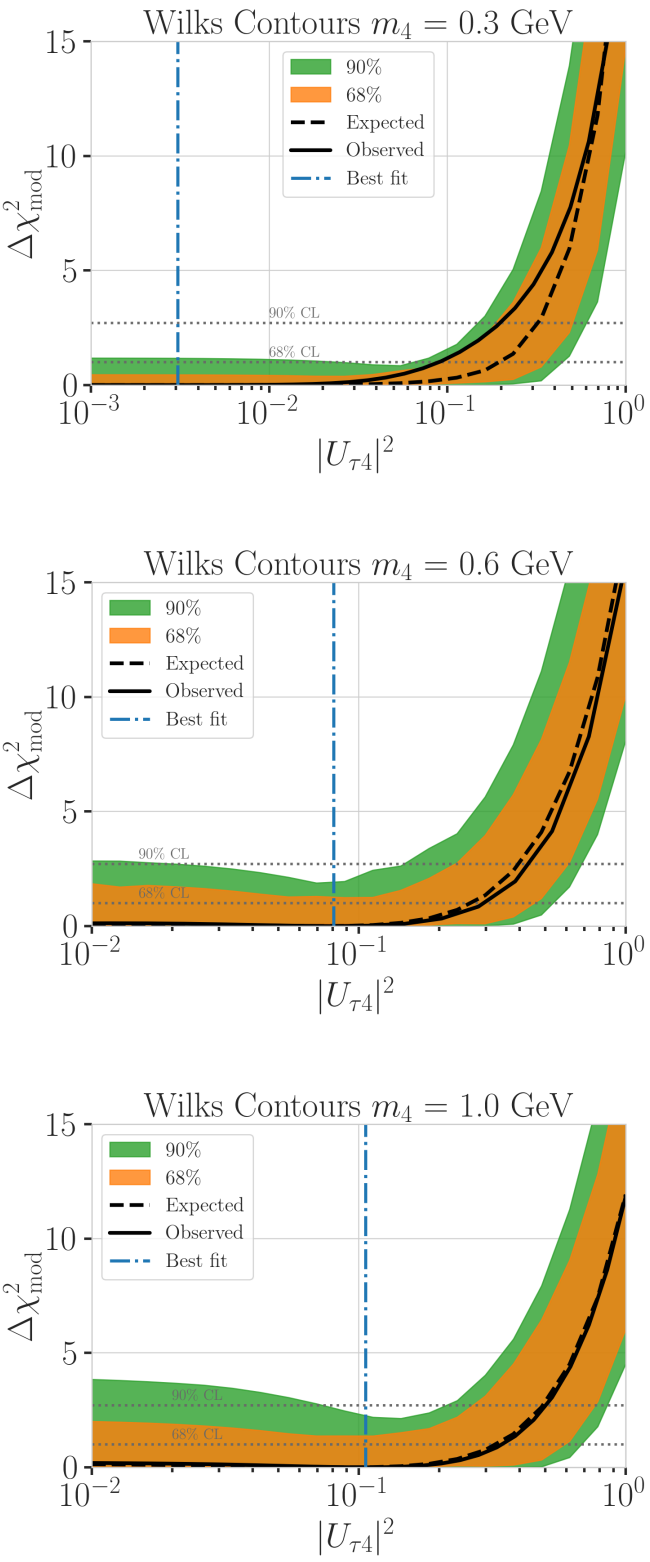

Figure 3.13: Best fit point TS profiles as a function of $|U_{\tau 4}|^2$ for the 0.3 GeV, 0.6 GeV, and 1.0 GeV mass samples. Shown are the observed profiles, the Asimov expectation at the best fit point, and the 68 % and 90 % bands, based on 100 pseudo-data trials. Also indicated are the 68 % and 90 % CL levels assuming Wilks' theorem.

Conclusion 4

Write conclusion (RED)

what was done?

1. set up model dependent and independent signal simulation for low energy double cascade events from HNL production and decay inside IceCube DeepCore

2. estimate performance of reconstructing and identifying these events

3. search for (cascade-like) events in 10 years of IceCube DeepCore data

possible improvements/future ideas for double cascade reconstruction and identification?

1. use more sophisticated machine learning algorithms for event selection and classification at lower levels 2. with icecube upgrade the performance of the existing reconstruction algorithms might improve (elaborate) 3. ml based reconstrucitons (GNN or so..)

Bibliography

Here are the references in citation order.

[1] C. N. Yang and R. L. Mills. "Conservation of Isotopic Spin and Isotopic Gauge Invariance". In: *Physical Review* 96.1 (Oct. 1954), pp. 191–195. DOI: 10.1103/PhysRev.96.191 (cited on page 1).

[2] S. Weinberg. "A Model of Leptons". In: *Phys. Rev. Lett.* 19 (21 Nov. 1967), pp. 1264–1266. DOI: 10.1103/PhysRevLett.19.1264 (cited on page 1).

[3] S. L. Glashow. "Partial-symmetries of weak interactions". In: *Nuclear Physics* 22.4 (Feb. 1961), pp. 579–588. DOI: 10.1016/0029-5582(61)90469-2 (cited on page 1).

[4] R. Jackiw. "Physical Formulations: Elementary Particle Theory. Relativistic Groups and Analyticity. Proceedings of the eighth Nobel Symposium, Aspenäsgården, Lerum, Sweden, May 1968. Nils Svartholm, Ed. Interscience (Wiley), New York, and Almqvist and Wiksell, Stockholm, 1969. 400 pp., illus. $31.75." In: *Science* 168.3936 (1970), pp. 1196–1197. DOI: 10.1126/science.168.3936.1196.b (cited on page 1).

[5] P. Higgs. "Broken symmetries, massless particles and gauge fields". In: *Physics Letters* 12.2 (1964), pp. 132–133. DOI: https://doi.org/10.1016/0031-9163(64)91136-9 (cited on page 1).

[6] S. Chatrchyan et al. "Observation of a New Boson at a Mass of 125 GeV with the CMS Experiment at the LHC". In: *Phys. Lett. B* 716 (2012), pp. 30–61. DOI: 10.1016/j.physletb.2012.08.021 (cited on page 1).

[7] G. Aad et al. "Observation of a new particle in the search for the Standard Model Higgs boson with the ATLAS detector at the LHC". In: *Phys. Lett. B* 716 (2012), pp. 1–29. DOI: 10.1016/j.physletb.2012.08.020 (cited on page 1).

[8] M. Gell-Mann. "A Schematic Model of Baryons and Mesons". In: *Resonance* 24 (1964), pp. 923–925 (cited on page 1).

[9] G. Zweig. "An SU(3) model for strong interaction symmetry and its breaking. Version 2". In: *DEVELOPMENTS IN THE QUARK THEORY OF HADRONS. VOL. 1. 1964 - 1978*. Ed. by D. B. Lichtenberg and S. P. Rosen. Feb. 1964, pp. 22–101 (cited on page 1).

[10] D. J. Gross and F. Wilczek. "Ultraviolet Behavior of Non-Abelian Gauge Theories". In: *PRL* 30.26 (June 1973), pp. 1343–1346. DOI: 10.1103/PhysRevLett.30.1343 (cited on page 1).

[11] C. Giunti and C. W. Kim. *Fundamentals of Neutrino Physics and Astrophysics*. Oxford University Press, Mar. 2007 (cited on page 1).

[12] M. D. Schwartz. *Quantum Field Theory and the Standard Model*. Cambridge University Press, 2013 (cited on page 1).

[13] A. Trettin. "Search for eV-scale sterile neutrinos with IceCube DeepCore". PhD thesis. Berlin, Germany: Humboldt-Universität zu Berlin, Mathematisch-Naturwissenschaftliche Fakultät, 2023. DOI: https://github.com/atrettin/PhD-Thesis (cited on pages 3, 7, 31, 41).

[14] N. Deruelle, J.-P. Uzan, and P. de Forcrand-Millard. *Relativity in Modern Physics*. Oxford University Press, Aug. 2018 (cited on page 4).

[15] R. L. Workman et al. "Review of Particle Physics". In: *Progress of Theoretical and Experimental Physics* 2022.8 (Aug. 2022), p. 083C01. DOI: 10.1093/ptep/ptac097 (cited on pages 4, 26).

[16] M. Fukugita and T. Yanagida. "Barygenesis without grand unification". In: *Physics Letters B* 174.1 (1986), pp. 45–47. DOI: https://doi.org/10.1016/0370-2693(86)91126-3 (cited on page 4).

[17] R. Davis, D. S. Harmer, and K. C. Hoffman. "Search for Neutrinos from the Sun". In: *Phys. Rev. Lett.* 20 (21 May 1968), pp. 1205–1209. DOI: 10.1103/PhysRevLett.20.1205 (cited on page 4).

[18] Y. Fukuda et al. “Evidence for Oscillation of Atmospheric Neutrinos”. In: *Phys. Rev. Lett.* 81 (8 Aug. 1998), pp. 1562–1567. DOI: 10.1103/PhysRevLett.81.1562 (cited on page 4).

[19] Q. R. Ahmad and other. “Direct Evidence for Neutrino Flavor Transformation from Neutral-Current Interactions in the Sudbury Neutrino Observatory”. In: *Phys. Rev. Lett.* 89 (1 June 2002), p. 011301. DOI: 10.1103/PhysRevLett.89.011301 (cited on page 4).

[20] S. Alam et al. “Completed SDSS-IV extended Baryon Oscillation Spectroscopic Survey: Cosmological implications from two decades of spectroscopic surveys at the Apache Point Observatory”. In: *Phys. Rev. D* 103 (8 Apr. 2021), p. 083533. DOI: 10.1103/PhysRevD.103.083533 (cited on page 4).

[21] N. Aghanim et al. “Planck2018 results: VI. Cosmological parameters”. In: *Astronomy & Astrophysics* 641 (Sept. 2020), A6. DOI: 10.1051/0004-6361/201833910 (cited on page 4).

[22] M. Aker et al. “Direct neutrino-mass measurement with sub-electronvolt sensitivity”. In: *Nature Phys.* 18.2 (2022), pp. 160–166. DOI: 10.1038/s41567-021-01463-1 (cited on page 4).

[23] T. Asaka, S. Blanchet, and M. Shaposhnikov. “The nuMSM, dark matter and neutrino masses”. In: *Phys. Lett. B* 631 (2005), pp. 151–156. DOI: 10.1016/j.physletb.2005.09.070 (cited on page 6).

[24] T. Asaka and M. Shaposhnikov. “The νMSM, dark matter and baryon asymmetry of the universe”. In: *Phys. Lett. B* 620 (2005), pp. 17–26. DOI: 10.1016/j.physletb.2005.06.020 (cited on page 6).

[25] P. Minkowski. “$\mu \to e\,\gamma$ at a rate of one out of 10^9 muon decays?” In: *Physics Letters B* 67.4 (Apr. 1977), pp. 421–428. DOI: 10.1016/0370-2693(77)90435-X (cited on page 6).

[26] T. Yanagida. “Horizontal Symmetry and Masses of Neutrinos”. In: *Progress of Theoretical Physics* 64.3 (Sept. 1980), pp. 1103–1105. DOI: 10.1143/PTP.64.1103 (cited on page 6).

[27] S. L. Glashow. “The Future of Elementary Particle Physics”. In: *NATO Sci. Ser. B* 61 (1980), p. 687. DOI: 10.1007/978-1-4684-7197-7_15 (cited on page 6).

[28] M. Gell-Mann, P. Ramond, and R. Slansky. “Complex Spinors and Unified Theories”. In: *Conf. Proc. C* 790927 (1979), pp. 315–321 (cited on page 6).

[29] R. N. Mohapatra and G. Senjanovi ć. “Neutrino Mass and Spontaneous Parity Nonconservation”. In: *Phys. Rev. Lett.* 44 (14 Apr. 1980), pp. 912–915. DOI: 10.1103/PhysRevLett.44.912 (cited on page 6).

[30] M. G. Aartsen et al. “eV-Scale Sterile Neutrino Search Using Eight Years of Atmospheric Muon Neutrino Data from the IceCube Neutrino Observatory”. In: *Phys. Rev. Lett.* 125.14 (2020), p. 141801. DOI: 10.1103/PhysRevLett.125.141801 (cited on page 7).

[31] J.-L. Tastet, O. Ruchayskiy, and I. Timiryasov. “Reinterpreting the ATLAS bounds on heavy neutral leptons in a realistic neutrino oscillation model”. In: *JHEP* 12 (2021), p. 182. DOI: 10.1007/JHEP12(2021)182 (cited on page 7).

[32] D. A. Bryman and R. Shrock. “Constraints on Sterile Neutrinos in the MeV to GeV Mass Range”. In: *Phys. Rev. D* 100 (2019), p. 073011. DOI: 10.1103/PhysRevD.100.073011 (cited on pages 8, 9).

[33] A. Aguilar-Arevalo et al. “Improved search for heavy neutrinos in the decay $\pi \to e\nu$”. In: *Phys. Rev. D* 97.7 (2018), p. 072012. DOI: 10.1103/PhysRevD.97.072012 (cited on page 8).

[34] G. Bellini et al. “New limits on heavy sterile neutrino mixing in B8 decay obtained with the Borexino detector”. In: *Phys. Rev. D* 88.7 (2013), p. 072010. DOI: 10.1103/PhysRevD.88.072010 (cited on pages 8, 11).

[35] D. Britton et al. “Improved search for massive neutrinos in $\pi + \to e + \nu$ decay”. In: *Physical Review D* 46 (1992) (cited on page 8).

[36] C. J. Parkinson et al. “Search for heavy neutral lepton production at the NA62 experiment”. In: *PoS* EPS-HEP2021 (2022), p. 686. DOI: 10.22323/1.398.0686 (cited on pages 8, 9).

[37] K. Abe et al. “Search for heavy neutrinos with the T2K near detector ND280”. In: *Phys. Rev. D* 100.5 (2019), p. 052006. DOI: 10.1103/PhysRevD.100.052006 (cited on pages 8, 9).

[38] P. Abreu et al. “Search for neutral heavy leptons produced in Z decays”. In: *Z. Phys. C* 74 (1997). [Erratum: Z.Phys.C 75, 580 (1997)], pp. 57–71. DOI: 10.1007/s002880050370 (cited on pages 8–10).

[39] R. Barouki, G. Marocco, and S. Sarkar. "Blast from the past II: Constraints on heavy neutral leptons from the BEBC WA66 beam dump experiment". In: *SciPost Phys.* 13 (2022), p. 118. DOI: 10.21468/SciPostPhys.13.5.118 (cited on pages 8, 10).

[40] D. Liventsev et al. "Search for heavy neutrinos at Belle". In: *Phys. Rev. D* 87.7 (2013). [Erratum: Phys.Rev.D 95, 099903 (2017)], p. 071102. DOI: 10.1103/PhysRevD.87.071102 (cited on page 8).

[41] P. Achard et al. "Search for heavy isosinglet neutrino in e^+e^- annihilation at LEP". In: *Phys. Lett. B* 517 (2001), pp. 67–74. DOI: 10.1016/S0370-2693(01)00993-5 (cited on page 8).

[42] F. Bergsma et al. "A Search for Decays of Heavy Neutrinos". In: *Phys. Lett. B* 128 (1983). Ed. by J. Tran Thanh Van, p. 361. DOI: 10.1016/0370-2693(83)90275-7 (cited on page 8).

[43] G. Aad et al. "Search for heavy neutral leptons in decays of W bosons produced in 13 TeV pp collisions using prompt and displaced signatures with the ATLAS detector". In: *JHEP* 10 (2019), p. 265. DOI: 10.1007/JHEP10(2019)265 (cited on pages 8, 9).

[44] G. Aad et al. "Search for Heavy Neutral Leptons in Decays of W Bosons Using a Dilepton Displaced Vertex in $\sqrt{s}$ = 13TeV pp Collisions with the ATLAS Detector". In: *Phys. Rev. Lett.* 131 (6 Aug. 2023), p. 061803. DOI: 10.1103/PhysRevLett.131.061803 (cited on pages 8, 9).

[45] A. M. Sirunyan et al. "Search for heavy neutral leptons in events with three charged leptons in proton-proton collisions at $\sqrt{s}$ = 13 TeV". In: *Phys. Rev. Lett.* 120.22 (2018), p. 221801. DOI: 10.1103/PhysRevLett.120.221801 (cited on pages 8, 9).

[46] A. Tumasyan et al. "Search for long-lived heavy neutral leptons with displaced vertices in proton-proton collisions at $\sqrt{s}$ =13 TeV". In: *JHEP* 07 (2022), p. 081. DOI: 10.1007/JHEP07(2022)081 (cited on pages 8, 9).

[47] A. Vaitaitis et al. "Search for neutral heavy leptons in a high-energy neutrino beam". In: *Phys. Rev. Lett.* 83 (1999), pp. 4943–4946. DOI: 10.1103/PhysRevLett.83.4943 (cited on pages 8, 9).

[48] E. Fernandez-Martinez et al. "Effective portals to heavy neutral leptons". In: *JHEP* 09 (2023), p. 001. DOI: 10.1007/JHEP09(2023)001 (cited on pages 8–10).

[49] G. Bernardi et al. "Search for Neutrino Decay". In: *Phys. Lett. B* 166 (1986), pp. 479–483. DOI: 10.1016/0370-2693(86)91602-3 (cited on page 8).

[50] M. Daum et al. "Search for Admixtures of Massive Neutrinos in the Decay $\pi^+ \to \mu^+$ Neutrino". In: *Phys. Rev. D* 36 (1987), p. 2624. DOI: 10.1103/PhysRevD.36.2624 (cited on pages 8, 9).

[51] A. V. Artamonov et al. "Search for heavy neutrinos in $K^+ \to \mu^+ \nu_H$ decays". In: *Phys. Rev. D* 91.5 (2015). [Erratum: Phys.Rev.D 91, 059903 (2015)], p. 052001. DOI: 10.1103/PhysRevD.91.052001 (cited on pages 8, 9).

[52] P. Astier et al. "Search for heavy neutrinos mixing with tau neutrinos". In: *Phys. Lett. B* 506 (2001), pp. 27–38. DOI: 10.1016/S0370-2693(01)00362-8 (cited on page 8).

[53] J. Orloff, A. N. Rozanov, and C. Santoni. "Limits on the mixing of tau neutrino to heavy neutrinos". In: *Phys. Lett. B* 550 (2002), pp. 8–15. DOI: 10.1016/S0370-2693(02)02769-7 (cited on pages 8, 10).

[54] I. Boiarska et al. "Constraints from the CHARM experiment on heavy neutral leptons with tau mixing". In: *Phys. Rev. D* 104.9 (2021), p. 095019. DOI: 10.1103/PhysRevD.104.095019 (cited on pages 8, 10).

[55] P. Abratenko et al. "Search for Heavy Neutral Leptons in Electron-Positron and Neutral-Pion Final States with the MicroBooNE Detector". In: *Phys. Rev. Lett.* 132.4 (2024), p. 041801. DOI: 10.1103/PhysRevLett.132.041801 (cited on page 9).

[56] Y. Ema et al. "Heavy Neutral Leptons from Stopped Muons and Pions". In: *JHEP* 08 (2023), p. 169. DOI: 10.1007/JHEP08(2023)169 (cited on page 9).

[57] A. Cooper-Sarkar et al. "Search for heavy neutrino decays in the BEBC beam dump experiment". In: *Physics Letters B* 160.1 (1985), pp. 207–211. DOI: https://doi.org/10.1016/0370-2693(85)91493-5 (cited on page 9).

[58] J. Badier et al. "Mass and Lifetime Limits on New Longlived Particles in 300-GeV/$c\pi^-$ Interactions". In: *Z. Phys. C* 31 (1986), p. 21. DOI: 10.1007/BF01559588 (cited on page 9).

[59] B. Shuve and M. E. Peskin. "Revision of the LHCb Limit on Majorana Neutrinos". In: *Phys. Rev. D* 94.11 (2016), p. 113007. DOI: 10.1103/PhysRevD.94.113007 (cited on page 9).

[60] R. Aaij et al. "Search for heavy neutral leptons in $W^+ \to \mu^+\mu^\pm$jet decays". In: *Eur. Phys. J. C* 81.3 (2021), p. 248. DOI: 10.1140/epjc/s10052-021-08973-5 (cited on page 9).

[61] R. Plestid. "Luminous solar neutrinos I: Dipole portals". In: *Phys. Rev. D* 104 (2021), p. 075027. DOI: 10.1103/PhysRevD.104.075027 (cited on pages 10, 11).

[62] A. Osipowicz et al. "KATRIN: A Next generation tritium beta decay experiment with sub-eV sensitivity for the electron neutrino mass. Letter of intent". In: (Sept. 2001) (cited on page 10).

[63] S. Mertens et al. "A novel detector system for KATRIN to search for keV-scale sterile neutrinos". In: *Journal of Physics G: Nuclear and Particle Physics* 46.6 (2019), p. 065203. DOI: 10.1088/1361-6471/ab12fe (cited on page 10).

[64] M. Aker et al. "Search for keV-scale sterile neutrinos with the first KATRIN data". In: *Eur. Phys. J. C* 83.8 (2023), p. 763. DOI: 10.1140/epjc/s10052-023-11818-y (cited on page 10).

[65] B. Abi et al. "Deep Underground Neutrino Experiment (DUNE), Far Detector Technical Design Report, Volume II: DUNE Physics". In: (Feb. 2020) (cited on page 10).

[66] S. Friedrich et al. "Limits on the Existence of sub-MeV Sterile Neutrinos from the Decay of ^{7}Be in Superconducting Quantum Sensors". In: *Phys. Rev. Lett.* 126.2 (2021), p. 021803. DOI: 10.1103/PhysRevLett.126.021803 (cited on page 10).

[67] C. Hagner et al. "Experimental search for the neutrino decay v3+vj+e++e- and limits on neutrino mixing". English. In: 52.3 (1995), pp. 1343–1352. DOI: 10.1103/PhysRevD.52.1343 (cited on page 11).

[68] R. Plestid. "Luminous solar neutrinos II: Mass-mixing portals". In: *Phys. Rev. D* 104 (2021). [Erratum: Phys.Rev.D 105, 099901 (2022)], p. 075028. DOI: 10.1103/PhysRevD.104.075028 (cited on page 11).

[69] P. Coloma et al. "Double-Cascade Events from New Physics in Icecube". In: *Phys. Rev. Lett.* 119.20 (2017), p. 201804. DOI: 10.1103/PhysRevLett.119.201804 (cited on page 11).

[70] P. Coloma. "Icecube/DeepCore tests for novel explanations of the MiniBooNE anomaly". In: *Eur. Phys. J. C* 79.9 (2019), p. 748. DOI: 10.1140/epjc/s10052-019-7256-8 (cited on page 11).

[71] M. Atkinson et al. "Heavy Neutrino Searches through Double-Bang Events at Super-Kamiokande, DUNE, and Hyper-Kamiokande". In: *JHEP* 04 (2022), p. 174. DOI: 10.1007/JHEP04(2022)174 (cited on page 11).

[72] P. Coloma et al. "GeV-scale neutrinos: interactions with mesons and DUNE sensitivity". In: *Eur. Phys. J. C* 81.1 (2021), p. 78. DOI: 10.1140/epjc/s10052-021-08861-y (cited on pages 11, 23, 25, 27).

[73] M. Tanabashi et al. "Review of Particle Physics". In: *Phys. Rev. D* 98 (3 Aug. 2018), p. 030001. DOI: 10.1103/PhysRevD.98.030001 (cited on pages 12, 14).

[74] M. Honda et al. "Atmospheric neutrino flux calculation using the NRLMSISE-00 atmospheric model". In: *Phys. Rev. D* 92 (2 July 2015), p. 023004. DOI: 10.1103/PhysRevD.92.023004 (cited on pages 12, 29, 37, 38, 43).

[75] A. Fedynitch et al. "Calculation of conventional and prompt lepton fluxes at very high energy". In: *European Physical Journal Web of Conferences*. Vol. 99. European Physical Journal Web of Conferences. Aug. 2015, p. 08001. DOI: 10.1051/epjconf/20159908001 (cited on page 13).

[76] P. A. M. Dirac. "The Quantum Theory of the Emission and Absorption of Radiation". In: *Proceedings of the Royal Society of London Series A* 114.767 (Mar. 1927), pp. 243–265. DOI: 10.1098/rspa.1927.0039 (cited on page 13).

[77] I. Esteban et al. "The fate of hints: updated global analysis of three-flavor neutrino oscillations". In: *JHEP* 09 (2020), p. 178. DOI: 10.1007/JHEP09(2020)178 (cited on page 14).

[78] A. Terliuk. "Measurement of atmospheric neutrino oscillations and search for sterile neutrino mixing with IceCube DeepCore". PhD thesis. Berlin, Germany: Humboldt-Universität zu Berlin, Mathematisch-Naturwissenschaftliche Fakultät, 2018. DOI: 10.18452/19304 (cited on page 15).

[79] J. A. Formaggio and G. P. Zeller. "From eV to EeV: Neutrino cross sections across energy scales". In: *Rev. Mod. Phys.* 84 (3 Sept. 2012), pp. 1307–1341. DOI: 10.1103/RevModPhys.84.1307 (cited on page 16).

[80] L. Fischer. https://github.com/LeanderFischer/icetray_double_cascade_generator_functions (cited on page 19).

[81] R. Abbasi et al. "LeptonInjector and LeptonWeighter: A neutrino event generator and weighter for neutrino observatories". In: *Comput. Phys. Commun.* 266 (2021), p. 108018. DOI: 10.1016/j.cpc.2021.108018 (cited on page 22).

[82] S. Agostinelli et al. "Geant4—a simulation toolkit". In: *Nucl. Instr. Meth. Phys. Res.* 506.3 (July 2003), pp. 250–303. DOI: 10.1016/s0168-9002(03)01368-8 (cited on page 23).

[83] L. Rädel and C. Wiebusch. "Calculation of the Cherenkov light yield from low energetic secondary particles accompanying high-energy muons in ice and water with Geant4 simulations". In: *Astroparticle Physics* 38 (Oct. 2012), pp. 53–67. DOI: 10.1016/j.astropartphys.2012.09.008 (cited on page 23).

[84] J. Alwall et al. "The automated computation of tree-level and next-to-leading order differential cross sections, and their matching to parton shower simulations". In: *JHEP* 07 (2014), p. 079. DOI: 10.1007/JHEP07(2014)079 (cited on page 23).

[85] J.-H. Koehne et al. "PROPOSAL: A tool for propagation of charged leptons". In: *Computer Physics Communications* 184.9 (2013), pp. 2070–2090. DOI: https://doi.org/10.1016/j.cpc.2013.04.001 (cited on page 23).

[86] C. Argüelles. https://github.com/arguelles/NuXSSplMkr (cited on page 24).

[87] N. Whitehorn, J. van Santen, and S. Lafebre. "Penalized splines for smooth representation of high-dimensional Monte Carlo datasets". In: *Computer Physics Communications* 184.9 (2013), pp. 2214–2220. DOI: https://doi.org/10.1016/j.cpc.2013.04.008 (cited on page 24).

[88] J.-M. Levy. "Cross-section and polarization of neutrino-produced tau's made simple". In: *J. Phys. G* 36 (2009), p. 055002. DOI: 10.1088/0954-3899/36/5/055002 (cited on page 24).

[89] E. Tiesinga et al. "CODATA recommended values of the fundamental physical constants: 2018". In: *Rev. Mod. Phys.* 93 (2 July 2021), p. 025010. DOI: 10.1103/RevModPhys.93.025010 (cited on page 26).

[90] https://launchpad.net/mg5amcnlo/3.0/3.3.x (cited on page 27).

[91] A. Alloul et al. "FeynRules 2.0 - A complete toolbox for tree-level phenomenology". In: *Comput. Phys. Commun.* 185 (2014), pp. 2250–2300. DOI: 10.1016/j.cpc.2014.04.012 (cited on page 27).

[92] C. Andreopoulos et al. "The GENIE Neutrino Monte Carlo Generator: Physics and User Manual". In: (2015) (cited on pages 29, 39).

[93] M. Glück, E. Reya, and A. Vogt. "Dynamical parton distributions revisited". In: *The European Physical Journal C* 5 (Sept. 1998), pp. 461–470. DOI: 10.1007/s100529800978 (cited on page 29).

[94] A. Bodek and U. K. Yang. "Higher twist, xi(omega) scaling, and effective LO PDFs for lepton scattering in the few GeV region". In: *Journal of Physics G: Nuclear and Particle Physics* 29.8 (2003), p. 1899. DOI: 10.1088/0954-3899/29/8/369 (cited on page 29).

[95] Y. Becherini et al. "A parameterisation of single and multiple muons in the deep water or ice". In: *Astroparticle Physics* 25.1 (2006), pp. 1–13. DOI: https://doi.org/10.1016/j.astropartphys.2005.10.005 (cited on page 30).

[96] D. Heck et al. "CORSIKA: A Monte Carlo code to simulate extensive air showers". In: (Feb. 1998) (cited on page 30).

[97] T. K. Gaisser. "Spectrum of cosmic-ray nucleons, kaon production, and the atmospheric muon charge ratio". In: *Astropart. Phys.* 35 (2012), pp. 801–806. DOI: 10.1016/j.astropartphys.2012.02.010 (cited on page 30).

[98] R. Engel et al. "The hadronic interaction model Sibyll – past, present and future". In: *EPJ Web Conf.* 145 (2017). Ed. by B. Pattison, p. 08001. DOI: 10.1051/epjconf/201614508001 (cited on page 30).

[99] C. Kopper et al. https://github.com/claudiok/clsim (cited on page 31).

[100] D. Chirkin et al. “Photon Propagation using GPUs by the IceCube Neutrino Observatory”. In: *2019 15th International Conference on eScience (eScience)*. 2019, pp. 388–393. DOI: 10.1109/eScience.2019.00050 (cited on page 31).

[101] M. G. Aartsen et al. “Measurement of South Pole ice transparency with the IceCube LED calibration system”. In: *Nucl. Instrum. Meth. A* 711 (2013), pp. 73–89. DOI: 10.1016/j.nima.2013.01.054 (cited on page 31).

[102] G. Mie. “Beiträge zur Optik trüber Medien, speziell kolloidaler Metallösungen”. In: *Annalen der Physik* 330.3 (1908), pp. 377–445. DOI: https://doi.org/10.1002/andp.19083300302 (cited on page 31).

[103] L. G. Henyey and J. L. Greenstein. “Diffuse radiation in the Galaxy.” In: *apj* 93 (Jan. 1941), pp. 70–83. DOI: 10.1086/144246 (cited on page 31).

[104] R. Abbasi et al. “In-situ estimation of ice crystal properties at the South Pole using LED calibration data from the IceCube Neutrino Observatory”. In: *The Cryosphere Discussions* 2022 (2022), pp. 1–48. DOI: 10.5194/tc-2022-174 (cited on page 31).

[105] S. Fiedlschuster. “The Effect of Hole Ice on the Propagation and Detection of Light in IceCube”. In: (Apr. 2019) (cited on page 32).

[106] M. G. Aartsen et al. “In-situ calibration of the single-photoelectron charge response of the IceCube photomultiplier tubes”. In: *Journal of Instrumentation* 15.6 (June 2020), P06032. DOI: 10.1088/1748-0221/15/06/P06032 (cited on page 32).

[107] M. Larson. “Simulation and Identification of Non-Poissonian Noise Triggers in the IceCube Neutrino Detector”. Available at https://ir.ua.edu/handle/123456789/1927. MA thesis. University of Alabama, Tuscaloosa, AL, USA, 2013 (cited on page 32).

[108] M. Larson. “A Search for Tau Neutrino Appearance with IceCube-DeepCore”. available at https://discoverycenter.nbi.ku.dk/teaching/thesis_page/mjlarson_thesis.pdf. PhD thesis. University of Copenhagen, Denmark, 2018 (cited on page 32).

[109] V. Barger et al. “Matter effects on three-neutrino oscillations”. In: *Phys. Rev. D* 22 (11 Dec. 1980), pp. 2718–2726. DOI: 10.1103/PhysRevD.22.2718 (cited on page 33).

[110] A. M. Dziewonski and D. L. Anderson. “Preliminary reference Earth model”. In: *Physics of the Earth and Planetary Interiors* 25.4 (1981), pp. 297–356. DOI: https://doi.org/10.1016/0031-9201(81)90046-7 (cited on page 33).

[111] S. Yu and J. Micallef. “Recent neutrino oscillation result with the IceCube experiment”. In: *38th International Cosmic Ray Conference*. July 2023 (cited on pages 34, 43, 47).

[112] R. Abbasi et al. “Measurement of atmospheric neutrino mixing with improved IceCube DeepCore calibration and data processing”. In: *Phys. Rev. D* 108 (1 July 2023), p. 012014. DOI: 10.1103/PhysRevD.108.012014 (cited on pages 38, 40).

[113] H. Dembinski et al. “Data-driven model of the cosmic-ray flux and mass composition from 10 GeV to 10^{11} GeV”. In: *PoS* ICRC2017 (2017), p. 533. DOI: 10.22323/1.301.0533 (cited on page 38).

[114] G. D. Barr et al. “Uncertainties in atmospheric neutrino fluxes”. In: *Phys. Rev. D* 74 (9 Nov. 2006), p. 094009. DOI: 10.1103/PhysRevD.74.094009 (cited on page 38).

[115] J. Evans et al. “Uncertainties in atmospheric muon-neutrino fluxes arising from cosmic-ray primaries”. In: *Phys. Rev. D* 95 (2 Jan. 2017), p. 023012. DOI: 10.1103/PhysRevD.95.023012 (cited on pages 38, 43).

[116] A. Fedynitch et al. https://github.com/afedynitch/MCEq (cited on page 38).

[117] G. D. Barr et al. “Uncertainties in Atmospheric Neutrino Fluxes”. In: *Phys. Rev. D* 74 (2006), p. 094009. DOI: 10.1103/PhysRevD.74.094009 (cited on pages 38, 43).

[118] F. Riehn et al. “Hadronic interaction model sibyll 2.3d and extensive air showers”. In: *Phys. Rev. D* 102 (6 Sept. 2020), p. 063002. DOI: 10.1103/PhysRevD.102.063002 (cited on page 38).

[119] A. Cooper-Sarkar, P. Mertsch, and S. Sarkar. “The high energy neutrino cross-section in the Standard Model and its uncertainty”. In: *JHEP* 08 (2011), p. 042. DOI: 10.1007/JHEP08(2011)042 (cited on page 39).

[120] Q. Wu et al. "A precise measurement of the muon neutrino–nucleon inclusive charged current cross section off an isoscalar target in the energy range 2.5<E<40 GeV by NOMAD". In: *Physics Letters B* 660.1 (2008), pp. 19–25. DOI: https://doi.org/10.1016/j.physletb.2007.12.027 (cited on page 40).

[121] M. M. Tzanov. "Precise measurement of neutrino and anti-neutrino differential cross sections on iron". PhD thesis. University of Pittsburgh, Pennsylvania, Jan. 2005 (cited on page 40).

[122] W. G. Seligman. "A next-to-leading-order QCD analysis of neutrino-iron structure functions at the Tevatron". PhD thesis. Columbia University, New York, Aug. 1997 (cited on page 40).

[123] J. Feintzeig. "Searches for Point-like Sources of Astrophysical Neutrinos with the IceCube Neutrino Observatory". PhD thesis. University of Wisconsin, Madison, Jan. 2014 (cited on pages 40, 43).

[124] N. Kulacz. "In Situ Measurement of the IceCube DOM Efficiency Factor Using Atmospheric Minimum Ionizing Muons". MA thesis. University of Alberta, 2019 (cited on pages 40, 43).

[125] Rongen, Martin. "Measuring the optical properties of IceCube drill holes". In: *EPJ Web of Conferences* 116 (2016), p. 06011. DOI: 10.1051/epjconf/201611606011 (cited on page 40).

[126] R. Abbasi et al. "In situ estimation of ice crystal properties at the South Pole using LED calibration data from the IceCube Neutrino Observatory". In: *The Cryosphere* 18.1 (2024), pp. 75–102. DOI: 10.5194/tc-18-75-2024 (cited on pages 41, 46).

[127] L. Fischer, R. Naab, and A. Trettin. "Treating detector systematics via a likelihood free inference method". In: *Journal of Instrumentation* 18.10 (2023), P10019. DOI: 10.1088/1748-0221/18/10/P10019 (cited on page 41).

[128] E. Lohfink. "Testing nonstandard neutrino interaction parameters with IceCube-DeepCore". PhD thesis. Mainz, Germany: Johannes Gutenberg-Universität Mainz, Fachbereich für Physik, Mathematik und Informatik, 2023. DOI: http://doi.org/10.25358/openscience-9288 (cited on page 42).

[129] M. G. Aartsen et al. "Computational techniques for the analysis of small signals in high-statistics neutrino oscillation experiments". In: *Nucl. Instrum. Meth. A* 977 (2020), p. 164332. DOI: 10.1016/j.nima.2020.164332 (cited on page 44).

[130] https://github.com/icecube/pisa (cited on page 44).

[131] R. S. Nickerson. "Confirmation Bias: A Ubiquitous Phenomenon in Many Guises". In: *Review of General Psychology* 2 (1998), pp. 175–220 (cited on page 44).

[132] H. Dembinski et al. *scikit-hep/iminuit: v2.17.0*. Version v2.17.0. Sept. 2022. DOI: 10.5281/zenodo.7115916 (cited on page 44).

[133] F. James and M. Roos. "Minuit: A System for Function Minimization and Analysis of the Parameter Errors and Correlations". In: *Comput. Phys. Commun.* 10 (1975), pp. 343–367. DOI: 10.1016/0010-4655(75)90039-9 (cited on page 44).

[134] S. S. Wilks. "The Large-Sample Distribution of the Likelihood Ratio for Testing Composite Hypotheses". In: *The Annals of Mathematical Statistics* 9.1 (1938), pp. 60–62. DOI: 10.1214/aoms/1177732360 (cited on page 48).

Acknowledgements

I would like to thank Marek for giving me the opportunity to conduct my research in the IceCube group at DESY. It was a pleasure to work in this group that combines the various research topics performed in IceCube but also offers the most friendly and welcoming atmosphere and wonderful colleagues.

I especially want to thank Summer for her continuous support and guidance throughout my five years at DESY. Thank you for all the invaluable and honest feedback on my work and beyond. I am grateful for all the opportunities you gave me and for everything I learned from you. I am very happy that I had the chance to work with you!

I would also like to thank Alex who shared 2L01 with me throughout most of my time at DESY and was a precious resource of insights, new ideas, and prompt support on anything I was struggling with.

Carlos Arguelles?

JVS?

I would also to like to thank everyone who proofread my thesis in order to make it a nice read: Cris, JVS, Alex

Reviewers: Thank you to xx and xx for reviewing my thesis.

Desy fam: Cris, Neha, Sofia, Richi

Actual fam: Christine/Wolfgang, Simon, Malin

Charlotte

Leander Fischer